Applications of Coupled-Wave Approach for 1D Gratings Illuminated from Planar Interface

Muhammad Kamran

Department of Electrical Engineering
Syed Babar Ali School of Science and Engineering
Lahore University of Management Science (LUMS)
Lahore, Pakistan

This dissertation is submitted in partial fulfillment
of the requirement for the degree of
Doctor of Philosophy

June 2020

I dedicate this thesis to my loving family.

Declaration

Lahore University of Management Sciences (LUMS)
Lahore, Pakistan.
Department of Electrical Engineering

I hereby declare that except where specific reference is made to the work of others, the contents of this dissertation are original and have not been submitted in whole or in part for consideration for any other degree or qualification in this or any other university. This dissertation is my own work and contains nothing which is the outcome of work done in collaboration with others, except as specified in the text and Acknowledgements.

Muhammad Kamran
June 2020

Acknowledgements

All praise and glories be to Allah, the Creator, Who created everything from spinning electrons to spiraling galaxies with astonishing beauty and symmetry. Also, peace be upon His last Prophet, Hazrat Muhammad, who taught us to unveil the truth behind the natural phenomena which gives us motivation for research.

I would like to take this opportunity to appreciate the role of my thesis advisor, Dr. Muhammad Faryad, in completion of this work. His constant guidance, support and encouragement enabled me to do this work.

I can never forget my teachers for what they have taught me, especially the thought-provoking lectures and inspiring personality of Dr. Muhammad Sabieh Anwar, Dr. Muhammad Imran Cheema, Dr. Ata Ulhaq, Dr. Nauman Zafar Butt, and Dr. Syed Azer Reza.

I want to thank the Lahore University of Management Sciences (LUMS) for providing me such a generous funding for my PhD. Without their constant financial support, it would have been very difficult for me to complete my degree. I also want to thank Higher Education Commission (HEC), Pakistan, for providing me funds for my PhD, as well as for supporting my six-month visit under the International Research Support Initiative Program (IRSIP). I am thankful to Michigan State University (MSU), and Prof. Shanker Balasubramaniam for their hosting under IRSIP. It really helped me to get the research exposure in the USA.

I think these acknowledgements remain incomplete without mentioning my family and friends. My special gratitude is for my father and mother, whose love has been with me throughout my education career. I want to acknowledge the constant support and patience of my wife Maria, because she was always waiting for me to come back home from LUMS, and spend time with her. She is a wonderful wife, I really want to thank her for her love. I also want to acknowledge the smiles of my daughter Aiza Kamran, who remained a source of joy during my PhD. I also thank my brothers Imran and Rizwan, sister Nadia, Bhabis Bushra and Saima for their moral and financial support in my odd times.

I would like to acknowledge constant support of my group mates and friends Aamir Hayat, Kiran Mujeeb, and Mehran Rasheed. I want to admire the the constant support from Muhammad Arshad Maral. He was very helpful during my time at LUMS. I want to mention the joyful company of my friends Muhammad Zareef, Muzamil Shah, Ali Akbar, Ali Raza

Mirza, Hasan Imran, Usama Bin Qasim, and Muhammad Umer Farooq. The time spent with these friends is unforgettable.

Muhammad Kamran

Abstract

Rigorous coupled-wave approach (RCWA) is formulated and applied to the computational modeling of problems involving 1D gratings and periodic structures. The RCWA is based on the expansion of the permittivity and permeability of the periodically varying material in terms of a Fourier series. A similar expansion of the electromagnetic field phasors is also used. This numerical method can be used to find the scattered and transmitted fields from surface-relief gratings and volume gratings.

In this thesis, the RCWA is used to study three important applications that require illumination from the planar side of periodic interface or periodic material. These applications involve surface plasmon-polariton (SPP) waves and anti-reflection coatings for solar cells. SPP waves are the electromagnetic surface waves that propagate at an interface of a metal and a dielectric material and find applications in sensitive (bio)chemical sensors, increasing the efficiency of light harvesting in the solar cells, imaging, microscopy, fiber optics, and waveguides. The SPP wave is excited only when the phase speed of the component of the incident light parallel to the interface is nearly equal to the phase speed of the possible SPP wave that can exist at that interface. Therefore, phase matching has to be achieved either by using a prism, or a surface-relief grating.

As a first application, SPP waves guided by an interface of a metal and a dielectric material using grating and prism couplings are numerically investigated for optical sensing. A new scheme is introduced by combining a prism on the planar side of the grating to excite the SPP waves. This new combination is only possible because of the excitation from the planar side. Both the prism-coupled configuration and the grating-coupled configurations have different advantages in an optical sensor. As a second application, the excitation of SPP waves at an interface of a metal and a one-dimensional photonic crystal (1DPC) along the direction of periodicity of the photonic crystal is theoretically studied. This interface was accessible only for illumination from the planar side. As a third application, we have proposed anti-reflection coatings of zero index metamaterials (ZIMs) for maximum absorption of light in solar cells. A thin layer of a ZIM is shown to help trap light inside a solar cell. The outer surface of the ZIM layer is planar, and the inner surface has periodic corrugations in order

for the incident light to pass through but block the re-transmission of the light back into free space.

Publications

- M. Kamran and M. Faryad, "Plasmonic sensor using a combination of grating and prism couplings", Plasmonics **14**, 791–798 (2019)
- M. Kamran and M. Faryad, "Excitation of surface plasmon polariton waves along the direction of periodicity of a one-dimensional photonic crystal", Physical Review A **99**, 053811 (2019)
- M. Kamran and M. Faryad, "Anti-reflection coatings of zero-index metamaterial for solar cells", AIP Advances **10**, 025010 (2020)
- H. Imran, I. Durrani, M. Kamran, T. M. Abdolkader, M. Faryad, and N. Z. Butt, "High-performance bifacial Perovskite/Silicon double-tandem solar cell", IEEE Journal of Photovoltaics **8**, 1222–1229 (2018)
- U. B. Qasim, H. Imran, M. Kamran, M. Faryad, and N. Z. Butt, "Computational study of stack/terminal topologies for perovskite based bifacial tandem solar cells", Solar Energy, **203**, 1–9 (2020)

Table of contents

List of figures

Chapter 1

Introduction

Periodic surfaces and periodic variations in the optical properties of materials are ubiquitous in optical devices. A periodic surface separating two dissimilar materials is called a surface-relief grating, and periodic variation in the permittivity and/or permeability is called volume grating. Usually, surface-relief gratings and volume gratings are illuminated from periodic surface to study scattering and other phenomena. The surface-relief gratings have many applications in the fields of acoustics, optics, holography and spectroscopy [1–4]. Gratings can also be used for the excitation of surface waves at an interface of two different materials [5]. Periodically corrugated metallic back reflectors are used for increasing the efficiency of energy harvesting in solar cells [6–8]. Because of periodic interfaces developed in contact lithography, it can also be used to understand near-field interaction [9, 10]. Gratings have application in the field of integrated optical devices. Integrated optical devices have the capability of doing the same tasks as the bulk optical devices are performing, but due to their compact size they are getting attention for on-chip applications. Some examples of integrated optical devices are beam expanders [11, 12], polarization-dependent devices [13–15], and holographic intensity profile reshaping [16, 17]. Other integrated optical device applications include the read/write heads of computer devices [18, 19], optical sensors [20, 21], and printer heads [22]. In all of the above examples, the grating is illuminated from the periodic side.

This thesis deals with the illumination from the planar side of the periodic materials to engender new applications. The illumination from the planar side opens up new avenues for applications, especially for surface plasmon-polariton (SPP) waves. SPP waves are the electromagnetic surface waves that are excited at an interface of a metal and a dielectric material. These waves find applications in the fields of chemical (bio) sensors, imaging, microscopy, fiber optics, and waveguide. The SPP wave cannot simply be excited by impinging light on a dielectric film that is lying on top of a metal film or a metal film lying on

top of a dielectric film because the phase speed of the SPP wave is usually smaller than that of a plane wave in the bulk partnering dielectric material. The SPP wave is excited only when the phase speed of the component of the incident light parallel to the interface is nearly equal to the phase speed of the possible SPP wave that can exist at that interface. Therefore, phase matching has to be achieved either by using a prism, or a surface-relief grating. There are two common configurations available to excite the surface waves, one is the prism-coupled configuration and the other is a grating-coupled configuration. By illuminating from planar side, we can couple the prism and grating configurations. Furthermore, the SPP wave is usually excited at an interface of a metal and a one-dimensional photonic crystal at an interface perpendicular to the direction of periodicity. This is excited in grating coupling by illuminating from periodic-interface side [5]. However, excitation of SPP waves parallel to the periodicity direction requires illumination from the planar side of the partnering metal. A problem where illumination from planar side is used already are periodic top surfaces in solar cells for light scattering into solar cells. Using the same setting, we propose a novel anti-reflection coating that is enabled only by illuminating from the planar side.

For all research presented in this thesis, we used rigorous coupled-wave approach (RCWA) for numerical computations. The RCWA is a numerical method that is used to compute the reflection and transmission coefficients from volume gratings and surface-relief gratings bounded by two dissimilar media. The RCWA was introduced by Moharam and Gaylord in 1981 [23]. The method is based on the Fourier series expansion of the material properties and the fields. They applied this method to a lossless sinusoidal grating to consider the diffraction of an obliquely incident plane wave. In 1982, they extended the RCWA for diffraction analysis of arbitrary surface-relief gratings [24], and later extended it to the three-dimensional diffraction for an arbitrarily oriented planar grating [25]. The extension of the RCWA for a metallic grating followed in 1986 by them [26], where they used a complex permittivity of the material. In 1987, the RCWA was formulated for three-dimensional anisotropic gratings [27]. An improved solution algorithm for the RCWA was developed for the diffraction gratings using a characteristic-matrix formulation later [28]. A stable and efficient algorithm for the binary gratings was soon developed for both the *s*- and *p*-polarization states as well as for the conical diffraction [29]. An application for multi-layer structures also quickly followed [30].

The rest of this chapter introduces SPP waves, anti-reflection coatings and zero-index metamaterial. A canonical boundary-value problem is presented for the SPP wave propagating at an interface of two dielectric-magnetic mediums in Section 1.1. Some commonly available configurations for the excitation of SPP waves and applications of SPP waves are presented in Section 1.2. Different types of anti-reflection coatings for solar cells are

presented in Section 1.3. A brief introduction to zero-index metamaterial is discussed in Section 1.4. At the end of this chapter, an overview of this thesis is presented in Section 1.5.

1.1 Surface Plasmon-Polariton (SPP) Waves

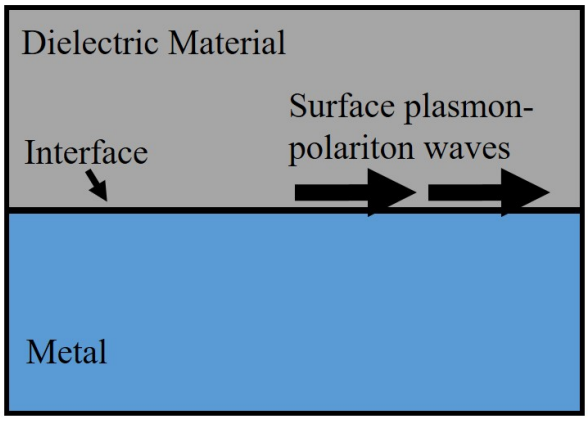

Fig. 1.1 Schematic figure showing the surface plasmon-polariton (SPP) waves guided by an interface of a metal and a dielectric material.

Surface waves are electromagnetic waves that are guided by an interface of two dissimilar materials. The surface waves guided by an interface of a metal and a dielectric material are called surface plasmon-polariton (SPP) waves [31], schematically shown in Fig. 1.1. The SPP waves are localized to the interface and decay away from that interface. This localization makes the SPP waves practically significant for sensitive (bio)chemical sensors because these waves are very sensitive to the small changes in the electromagnetic properties of the partnering metal and dielectric material near the interface [32]. The SPP-wave-based sensors can be used to sense very small molecules in analytes, pollutants in the environment, and small concentration of proteins or assays in a solution [33]. All these detections rely on sensing the small change in the refractive index of the dielectric material near the metal/dielectric interface.

The basic characteristics of an SPP wave can be understood from its dispersion equation that shows the relation of the wave number of the wave and the properties of the partnering materials. Dispersion equation can be best derived by eliminating all the interfaces but one

to exclude all the possibilities other than surface waves. This problem is called canonical boundary-value problem.

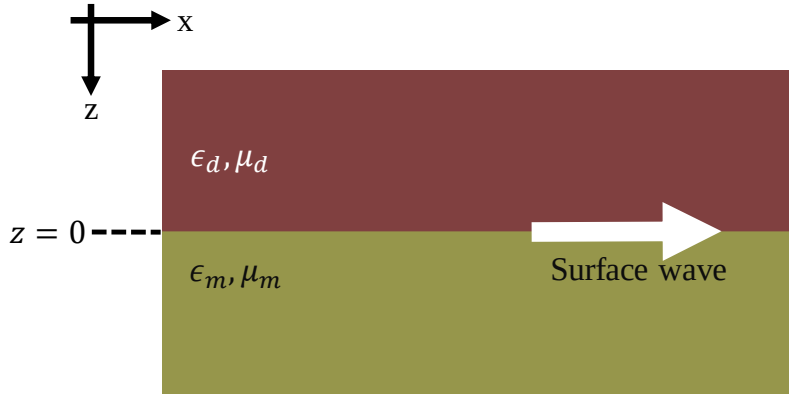

Fig. 1.2 Schematic of the geometry of the canonical boundary-value problem. The horizontal arrow at the interface of two dissimilar mediums at $z = 0$ shows the propagation of surface wave.

Let us consider SPP wave propagation by planar interface of two general isotropic materials. For this purpose, let us consider the geometry of the canonical boundary-value problem shown in Fig. 1.2. The half-space $z < 0$ is occupied by a dielectric-magnetic medium of relative permittivity ε_d and relative permeability μ_d. The half-space $z > 0$ is occupied by another dielectric-magnetic medium with relative permittivity ε_m and relative permeability μ_m. Without loss of generality, let us assume that the surface wave is propagating in the planar interface of two dielectric-magnetic mediums along the x-axis. The electric and magnetic field phasors in the two contiguous half-spaces can be written as [34]

$$\mathbf{E}^d(\mathbf{r}) = \left[a_s\hat{\mathbf{u}}_y + a_p\left(\frac{\alpha_d\hat{\mathbf{u}}_x + q\hat{\mathbf{u}}_z}{k_0 n_d}\right)\right]\exp\left[i(qx - \alpha_d z)\right], \quad z < 0, \tag{1.1}$$

$$\mathbf{H}^d(\mathbf{r}) = \frac{1}{\eta_d\eta_0}\left[a_s\left(\frac{\alpha_d\hat{\mathbf{u}}_x + q\hat{\mathbf{u}}_z}{k_0 n_d}\right) - a_p\hat{\mathbf{u}}_y\right]\exp\left[i(qx - \alpha_d z)\right], \quad z < 0, \tag{1.2}$$

$$\mathbf{E}^m(\mathbf{r}) = \left[b_s\hat{\mathbf{u}}_y + b_p\left(\frac{-\alpha_m\hat{\mathbf{u}}_x + q\hat{\mathbf{u}}_z}{k_0 n_m}\right)\right]\exp\left[i(qx + \alpha_m z)\right], \quad z > 0, \tag{1.3}$$

$$\mathbf{H}^m(\mathbf{r}) = \frac{1}{\eta_m\eta_0}\left[b_s\left(\frac{-\alpha_m\hat{\mathbf{u}}_x + q\hat{\mathbf{u}}_z}{k_0 n_m}\right) - b_p\hat{\mathbf{u}}_y\right]\exp\left[i(qx + \alpha_m z)\right], \quad z > 0, \tag{1.4}$$

where $n_d = \sqrt{\varepsilon_d \mu_d}$, $n_m = \sqrt{\varepsilon_m \mu_m}$, $\eta_d = \sqrt{\mu_d/\varepsilon_d}$, $\eta_m = \sqrt{\mu_m/\varepsilon_m}$, and

$$\alpha_d = \sqrt{k_0^2 n_d^2 - q^2}\,, \tag{1.5}$$

$$\alpha_m = \sqrt{k_0^2 n_m^2 - q^2}\,. \tag{1.6}$$

Furthermore, a_p, a_s, b_p, and b_s are the unknown amplitudes, and $\hat{\mathbf{u}}_\mathrm{x}$, $\hat{\mathbf{u}}_\mathrm{y}$ and $\hat{\mathbf{u}}_\mathrm{z}$ are the Cartesian unit vectors.

For surface-wave propagation, α_d and α_m are complex-valued such that their imaginary parts are positive to keep the fields localized to the interface $z = 0$. The continuity of the x and the y components of the electric and magnetic fields at the interface $z = 0$ give the following four equations:

$$a_p \frac{\alpha_d}{n_d} = -b_p \frac{\alpha_m}{n_m}\,, \tag{1.7}$$

$$a_s = b_s\,, \tag{1.8}$$

$$a_s \frac{\alpha_d}{\eta_d n_d} = -b_s \frac{\alpha_m}{\eta_m n_m}\,, \tag{1.9}$$

$$\frac{a_p}{\eta_d} = \frac{b_p}{\eta_m}\,. \tag{1.10}$$

Since both the partnering mediums are isotropic, the s- and p-polarization states decouple from each other as can be seen from Eq. (1.7)–(1.10)

1.1.1 S-polarized Surface Waves

Using Eqs. (1.8) and (1.9), we get

$$\frac{\alpha_d}{\mu_d} = -\frac{\alpha_m}{\mu_m}\,, \tag{1.11}$$

and using Eqs. (1.5) and (1.6), we get

$$\left(\frac{\alpha_m}{\alpha_d}\right)^2 = \frac{(k_0 n_m)^2 - q^2}{(k_0 n_d)^2 - q^2}\,. \tag{1.12}$$

Simultaneously solving Eqs. (1.11) and (1.12), we get expressions for α_d, α_m and q as

$$\alpha_d = k_0 \mu_d \sqrt{\frac{\varepsilon_d \mu_d - \mu_m \varepsilon_m}{\mu_d^2 - \mu_m^2}}\,, \quad \mathrm{Im}[\alpha_d] > 0, \tag{1.13}$$

$$\alpha_m = k_0 \mu_m \sqrt{\frac{\varepsilon_d \mu_d - \mu_m \varepsilon_m}{\mu_d^2 - \mu_m^2}}\,, \quad \mathrm{Im}[\alpha_m] > 0, \tag{1.14}$$

$$q = k_0 \sqrt{\frac{\mu_d \mu_m (\varepsilon_m \mu_d - \varepsilon_d \mu_m)}{\mu_d^2 - \mu_m^2}}. \tag{1.15}$$

The last equation gives wave number q of s-polarized SPP waves. When $\mu_m = \mu_d = 1$, we get from Eq. (1.11) $\alpha_d = -\alpha_m$, which means $\mathrm{Im}[\alpha_m]$ and $\mathrm{Im}[\alpha_m]$ can not be both positive at the same time. So s-polarized SPP can not exist.

1.1.2 P-polarized Surface Waves

Using Eqs. (1.7) and (1.10), we get

$$\frac{\alpha_d}{\varepsilon_d} = -\frac{\alpha_m}{\varepsilon_m}. \tag{1.16}$$

Next, solving Eqs. (1.12) and (1.16), we get α_d, α_m and q as

$$\alpha_d = k_0 \varepsilon_d \sqrt{\frac{\varepsilon_d \mu_d - \mu_m \varepsilon_m}{\varepsilon_d^2 - \varepsilon_m^2}}, \tag{1.17}$$

$$\alpha_m = k_0 \varepsilon_m \sqrt{\frac{\varepsilon_d \mu_d - \mu_m \varepsilon_m}{\varepsilon_d^2 - \varepsilon_m^2}}, \tag{1.18}$$

$$q = k_0 \sqrt{\frac{\varepsilon_d^2 \mu_m \varepsilon_m - \varepsilon_m^2 \mu_d \varepsilon_d}{\varepsilon_d^2 - \varepsilon_m^2}}. \tag{1.19}$$

The dispersion Eq. (1.19) gives the wavenumber of possible p-polarized SPP wave. When $\mu_m = \mu_d = 1$, we get the usual case of $q = k_0 \sqrt{\frac{\varepsilon_d \varepsilon_m}{\varepsilon_d + \varepsilon_m}}$.

1.2 Excitation of SPP Waves

Excitation of SPP waves is not simple and straightforward. SPP waves cannot be excited by simply illuminating the light on the dielectric material that is lying on a metal film or a metal film lying on top of a dielectric material. This is because the phase speed of the SPP wave is smaller than the plane wave in the dielectric material. The SPP wave is excited only when the phase speed of the component of the incident light parallel to the interface is nearly equal to the phase speed of the possible SPP wave that can exist at that interface. The phase speed of possible SPP waves is determined by canonical boundary-value problem. Therefore, wavenumber matching has to be attained because phase speed is related to wavenumber by the relation $v_p = \omega/k$. The wavenumber matching can be achieved either by using a

prism, or a surface-relief grating. For exciting SPP waves in practical configurations, only the materials with finite thicknesses are used. Many practical configurations are available for SPP wave excitation. The most common are described below.

1.2.1 Prism-Coupled Configurations

The prism-coupled configuration can be either Turbadar–Kretschmann–Raether (TKR) [35, 36] (commonly called Kretschmann configuration) or Turbadar–Otto [35, 37] (commonly called Otto configuration). They both employ evanescent waves to excite SPP waves. The

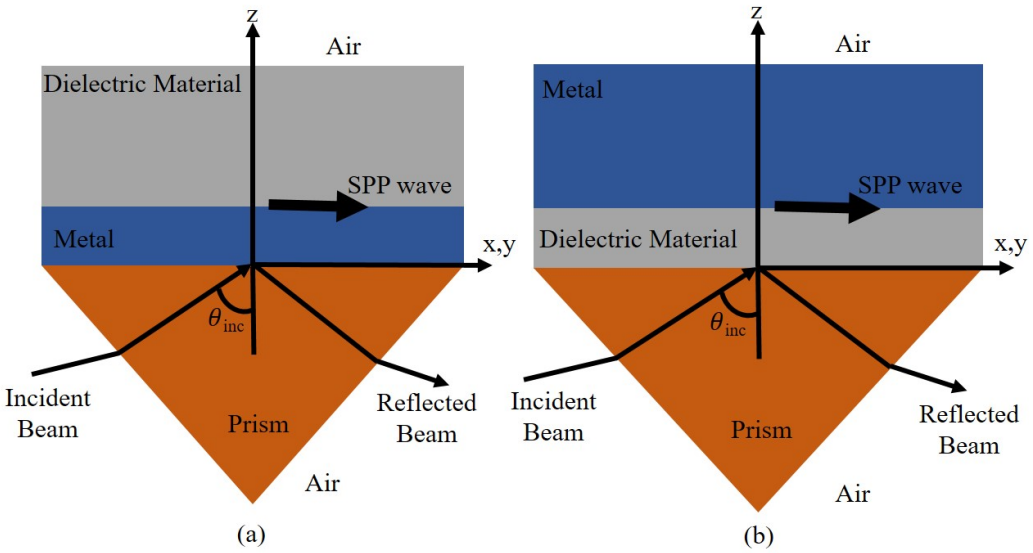

Fig. 1.3 Schematic figure of (a) Turbadar–Kretschmann–Raether configuration (TKR) and (b) Turbadar–Otto configuration.

TKR configuration is more famous and practical of the two prism-coupled configurations. It consists of a prism whose refractive index exceeds the refractive index of the dielectric material. An interface is formed by depositing dielectric material over metallic film. Other side of the metal is attached with the base of prism as shown in Fig. 1.3(a). When the ray of light impinges on the prism/metal interface at an angle θ, the component of wave vector parallel to metal/dielectric interface is given by

$$k_x = n_p k_0 \sin\theta\,, \tag{1.20}$$

where n_p is the refractive index of the prism. The SPP wave is only excited when the real part of the wavenumber q of possible SPP wave is nearly equal to k_x, i.e.,

$$n_p k_0 \sin\theta \approx \mathrm{Re}(q)\,. \tag{1.21}$$

The Turbadar–Otto configuration is similar to the TKR, but the position of metal and dielectric is interchanged, as shown in Fig. 1.3(b). Turbadar–Otto configuration is less popular as compared to the TKR configuration. It is because Turbadar–Otto configuration requires thin layer of dielectric material. In sensing applications, where dielectric material is involved, thick layer of dielectric material is desirable. On the other hand, in TKR configuration we require thin layer of metal, which is not a problem in sensing applications.

1.2.2 Grating-Coupled Configuration

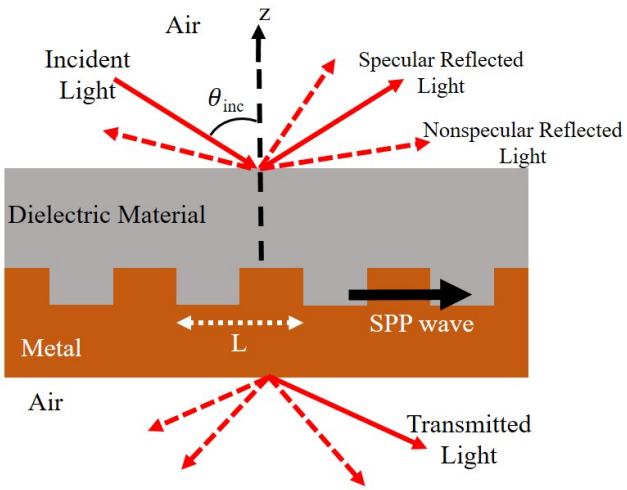

Fig. 1.4 Schematic of grating-coupled configuration for excitation of SPP wave.

In the grating-coupled configuration [31], a periodically corrugated interface of a dielectric material and a metal is used to create non-specular electromagnetic modes with various wavenumbers, schematically shown in Fig. 1.4. An SPP wave is excited if the wavenumber of one of the non-specular mode is the same as that of the possible SPP wave and a dip in reflectance spectrum (or a peak in absorptance spectrum) appears because of the energy transfer from the incident light to the SPP wave. In this configuration metal and dielectric material are of finite thickness with a surface-relief grating $z = g(x) = g(x \pm L)$ at their

interface, where L is the period along x-axis. A surface wave is excited when

$$\mathrm{Re}(q) \approx k_0 \sin\theta + \ell\frac{2\pi}{L}, \quad \ell \in \{0, \pm 1, \pm 2, ...\}. \tag{1.22}$$

To investigate grating-coupled configuration theoretically, we require the help of numerical techniques like the extinction boundary condition method [38, 39], the method of covariant spatial transformation [40], and the rigorous coupled-wave approach (RCWA) [27, 28]. All these numerical method work very well for grating-coupled configuration when the partnering materials are homogeneous and isotropic. But for periodically nonhomogeneous and anisotropic materials, the RCWA is well suited [27].

1.2.3 Waveguide-Coupled Configurations

Excitation of SPP wave can be possible in the waveguide-coupled configuration. This configuration is also called the end-fire configuration. For applications in the integrated optics, waveguide-coupled configuration is suitable. In waveguide-coupled configuration,

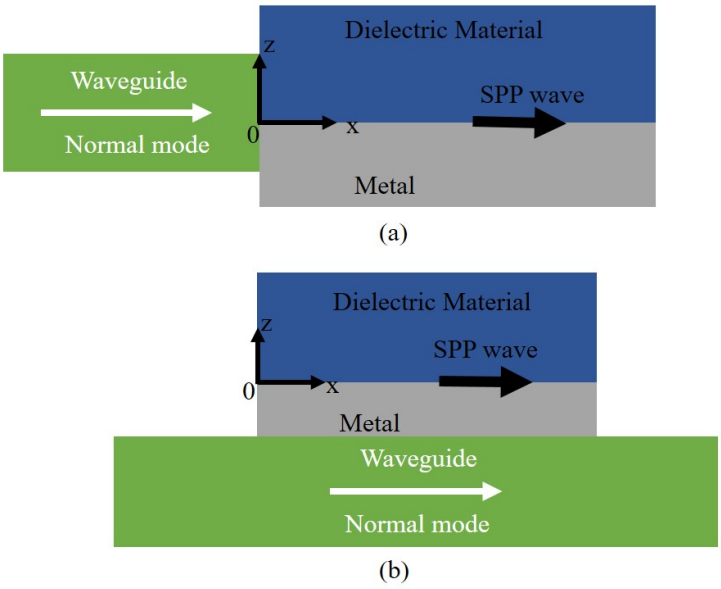

Fig. 1.5 Schematic of waveguide-coupled configuration for excitation of SPP wave.

plane $x = 0$ separates waveguide ($x < 0$) from metal/dielectric structure ($x > 0$), as shown in Fig. 1.5(a). The axis of the waveguide is x-axis. The cross sectional area of both the waveguide and metal/dielectric structure must be significantly large so that fields must decay before reaching out the limits of metal/dielectric structure and waveguide. This configuration

was introduced by Stegeman et al. [41] in 1983. For sensing applications, a different waveguide-coupled configuration is used. In this configuration a thin layer of metal is placed on a dielectric waveguide, and partnering dielectric layer is placed on the top of metal layer as shown in Fig. 1.5(b). This type of configuration is useful in building sensors due to their small size and ruggedness [33].

1.2.4 Applications of SPP Waves

The SPP waves are sensitive to the change in permittivity/permeability of the partnering materials. Therefore most common applications of SPP waves are in optical sensing. Sensing applications started back in 1980s. Practical configurations employ evanescent waves to excite SPP waves. The SPP wave absorbs energy from the evanescent wave that results in a reduction in the reflected light and increase in absorptance showing as a reflectance dip or an absorptance peak in the spectrum. This is often referred to as surface plasmon resonance (SPR). These SPR based sensors can detect the change in refractive index as low as 3×10^{-7} [32]. SPP waves are present in a very narrow region of interface and these waves are very sensitive to the change in refractive index. Using SPR we can sense a wide range of chemical and biochemical species. SPR based sensors are deployed to sense very small molecules, which found its application in observing pollutants in the environment, pathological analyses in medical laboratories, purity and compositional analyses in different industries [42–44].

Prism-coupled configuration is very good for sensing analytes. The TKR configuration is more convenient than the Turbadar–Otto, because latter configuration requires thin layer of dielectric, which is not good for sensing application. Wide range of samples can be sensed using prism-coupled configuration.

Grating-coupled configuration is also applied in sensing application [45]. Grating-coupled configuration is more useful in sensors where electronic circuitry is involved. It is because modern technology is based planar chips and integration with electronic circuitry is easy without the need of bulky prisms.

Advances in the research had opened new doors in the energy sector. Efficiency of light harvesting by solar cells is improved many times using periodic texturing. Use of plasmonic structures to increase the absorption capability is being investigated [46, 47].

1.3 Anti-Reflection Coatings for Solar Cells

Solar cells are at the leading position for the alternative energy sources. In a solar cell, the optical properties are responsible for how much light is absorbed by it, and thus the quantity

of light that generates the electron-hole pairs [48]. Two conventional methods to enhance the absorption of light of solar cells are light trapping and anti-reflection coatings.

For light trapping, surface-relief gratings and rough surfaces are used for light scattering and excitation of surface waves inside the solar cell. Anti-reflection coatings are designed using the principle of interference of light between incident and reflected waves. The idea in anti-reflection coatings is to cancel the reflecting light by destructive interference of light reflected from multiple interfaces. Basic anti-reflection coatings are discussed here.

1.3.1 Index-Matching Layer

The simplest anti-reflection coatings were discovered by Lord Rayleigh in 1886. At that time, the optical glass tended to develop a tarnish on its surface due to the environmental effects. Rayleigh took a tarnished glass and tested the light reflection and transmission from that tarnished glass. He found that the glass with the tarnish transmitted more light than the clean glass. It was because the tarnish created an extra interface at the glass surface. Now the glass surface has two interfaces, one is the glass-tarnish and the other is tarnish-air interface. The refractive index of tarnish is between the refractive indices of air and glass, so it offers less reflection than the air-glass interface did [49]. Hence by matching the indices we can also make anti-reflection coatings.

1.3.2 Quarter-Wave Layer

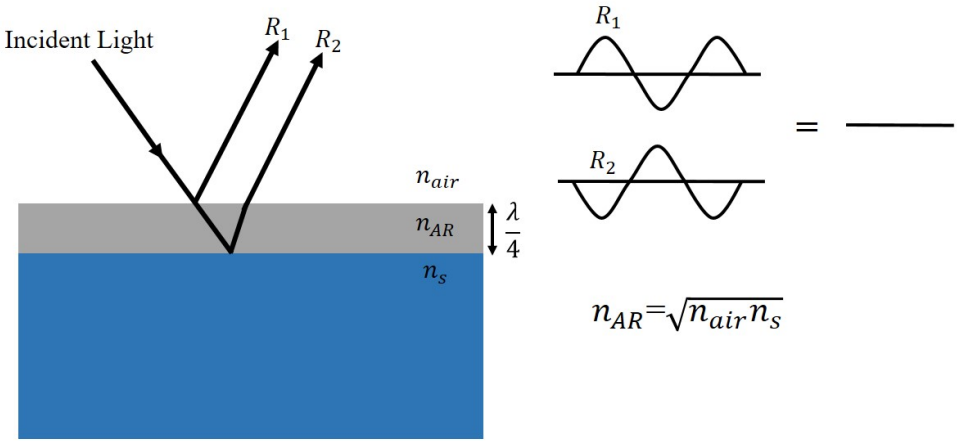

Fig. 1.6 Schematic of single-layer anti-reflection coatings of quarter-wave layer.

The most commonly known anti-reflection coating is a quarter-wave layer. A quarter-wave layer of anti-reflection coating can reduce the reflections at the desired wavelength. The idea of quarter-wave layer is based on the creation of a thin layer which provides two interfaces, to give two reflected waves as shown in Fig. 1.6. When the thickness of the anti-reflection coating is $\lambda/4$, the reflected waves R_1 and R_2 will be 180 deg out of phase as shown in Fig. 1.6, resulting in a destructive interference. Hence they give rise to zero reflection. For the suppression of reflected wave, the refractive index of the anti-reflection coating has to be the geometric mean of the refractive indices of the air and the substrate. The drawback of this type of anti-reflection coatings is that it reduces the reflection only at a single wavelength and for a single incidence angle.

1.3.3 Double Layer Coatings

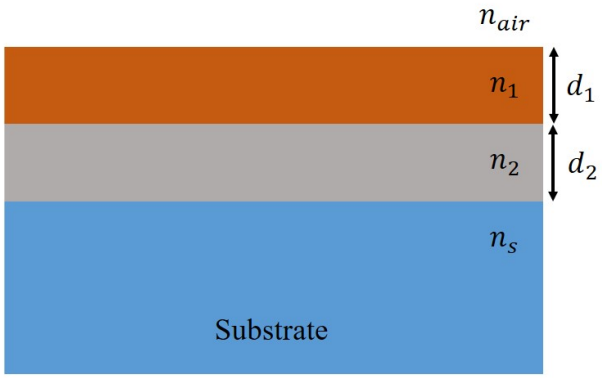

Fig. 1.7 Schematic of double-layer anti-reflection coatings.

Double layer [50–52] anti-reflection coatings are very useful for reducing the reflection for a specific wavelength. In double-layer anti-reflection coatings, the upper layer facing the air has low refractive index than the other layer, schematically shown in Fig. 1.7. In this scheme, the interference condition should be fulfilled for the destructive interference in these two layers. Therefore the thicknesses of each layer is set to be the multiple of quarter or half wavelength ($\lambda/4$ and $\lambda/2$). The optical thicknesses of each layer and the refractive index can be set using the relation

$$n_1 \times d_1 = n_2 \times d_2\,, \tag{1.23}$$

and condition for the reduction of reflection down to zero is given by [49]

$$n_1 \times n_2 = n_{air} \times n_s \,, \tag{1.24}$$

where n_1 and n_2 are the refractive indices of first (upper) layer and the second layer, respectively, and d_1 and d_2 are the thickness of these layers. This coating is somewhat broad band than single layer, but it requires more complicated structure and material.

1.3.4 Multi-Layer Coatings

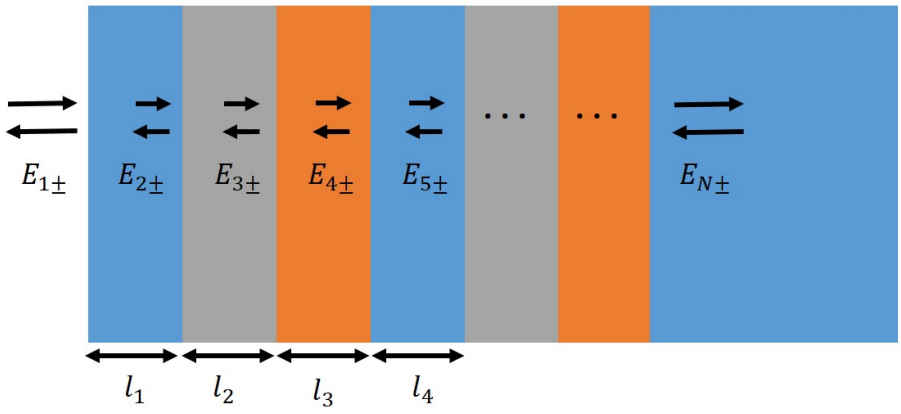

Fig. 1.8 Schematic of multi-layer anti-reflection coatings.

A single-layer anti-reflection coatings can minimize the reflection only at a single wavelength. For a broad spectrum, multi-layer anti-reflection coatings can be used to get zero refelction at multiple wavelengths [53, 54]. These multi-layer coatings can be combined with different thicknesses to minimize the reflections for a broad range of spectrum, as schematically shown in Fig. 1.8. The interference condition is achieved in these layers by light circulation inside the optical cavities formed by thin films [55]. Forward and backward moving fields add in each other to fulfill the condition of destructive interference. However, increasing the number of layers keeps on adding complexity to design.

1.4 Zero-Index Metamaterials (ZIM)

Metamaterials are the artificially designed materials that get their bulk properties from not only their constituent materials but also from their structural arrangements. Common metamaterials include double positive materials with both the permittivity and permeability having positive values [56], double negative [57, 58], zero-index metamaterial (ZIM) with near-zero refractive index [59, 60], bi-isotropic and bianisotropic materials [61, 62]. The ZIM is a metamaterial in which the permittivity and/or the permeability of the medium are nearly zero, thus its refractive index is close to zero. The ZIM finds applications in electromagnetic cloaking [63], directional emission [64], tunneling effects [65], transition from total reflection to total transmission [66], and the reshaping of the phase front [67, 68]. The ZIM can be designed as a mixture of metallic and dielectric materials or as a photonic crystal of all-dielectric materials working at a frequency close to the Dirac-like point in the photonic band structure [69, 70]. The ZIM using metallic inclusion suffer from the ohmic losses and the fact that the impedance is infinite. However, the photonic-crystal-based design do not suffer from both of these issues. However, all designs of the ZIM currently are not broadband.

When the refractive index n of a material is near zero, the phase velocity $v_D = \omega/nk_0$ is very large inside it, and wavelength $\lambda = \lambda_0/n$ is also large. As a result, phase is uniform throughout the material regardless of the size and shape of the material. The fields inside the material whose refractive index is zero oscillate in unison as field dependence is only on $\exp(i\omega t)$. Now there will bo no spatial dependence, and a quasi-electrostatic behavior can be achieved. This uniform phase inside ZIM gives rise to numerous applications like phase-front shaping [71] and unidirectional transmission [72, 73].

1.5 Thesis Overview

The goal of the thesis is twofold: First is to generalize the RCWA to formulate the boundary-value problem of scattering from the dielectric-magnetic gratings. A stable algorithm of the RCWA is implemented on the computer. The second goal is to apply the RCWA for the computational modeling of the problems involving periodic structure with inverted geometry. Therefore, a detailed mathematical formulation of the RCWA is given in Chapter 2. The RCWA is formulated for the surface-relief grating at an interface of two different dielectric-magnetic materials. Complete algorithm and the method of computation of fields is given in detail.

In Chapter 3, a plasmonic sensor using a combination of grating and prism couplings is presented. A new scheme is described that uses the prism and grating couplings for the optical sensing after exploiting illumination from the planar side. The plasmonic sensor is analyzed using both angular and wavelength interrogations.

In Chapter 4, the excitation of surface plasmon-polariton waves along the direction of periodicity of one-dimensional photonic crystal is described. Previously, the SPP waves guided by one-dimensional photonic crystals are usually excited at the interface perpendicular to the direction of periodicity. In this work, we will present the numerical results describing the excitation of the SPP waves on the interface along the direction of periodicity. This new interface is accessed by illuminating from planar metallic side.

In Chapter 5, anti-reflection coatings of zero-index metamaterial for solar cells are proposed and analyzed. A new scheme of designing anti-reflection coatings using zero index materials is presented. This approach can be used to design light-trapping layers for other devices as well.

In Chapter 6, the concluding remarks are presented. Some future directions of this work are also given in Chapter 6. All the computer codes are compiled in Matlab. Important codes are given in the Appendix. The given codes are for some figures as specified and the codes for remaining figures are similar with small changes.

An $\exp(-i\omega t)$ time-dependency is implicit throughout the thesis, where ω is the angular frequency and t being the time. The free-space wavenumber and the free-space wavelength are indicated by $k_0 = \omega\sqrt{\varepsilon_0\mu_0}$ and $\lambda_0 = 2\pi/k_0$, respectively, where ε_0 and μ_0 are the permittivity and permeability of free space. Vectors are in bold face, and unit vectors are in bold face and have a hat on them. The Cartesian unit vectors are denoted by $\hat{\mathbf{u}}_{\mathrm{x}}$, $\hat{\mathbf{u}}_{\mathrm{y}}$ and $\hat{\mathbf{u}}_{\mathrm{z}}$. Matrices are enclosed in square brackets.

Chapter 2

Rigorous Coupled-Wave Approach for Dielectric-Magnetic Materials

Rigorous coupled-wave approach (RCWA) is a numerical technique in the computational electromagnetics that is used to solve the scattering problems involving periodic structures and gratings [23]. This method demands that all the field quantities and the material properties be expressed as Fourier series. The RCWA is used to find the reflection and transmission coefficients from the surface-relief gratings or volume gratings. These gratings have many applications in the field of optics, acoustics, and spectroscopy [1–4]. These gratings are also helpful in designing optical sensors and improving diffractive structures for high efficiency photovoltaics solar cells [6–8]. The RCWA is used for numerical results in all of this thesis.

In this chapter, the RCWA is generalized to formulate the boundary-value problem of scattering from the dielectric-magnetic gratings. The formulation is developed for a surface-relief grating with both sides of the grating occupied by the dielectric-magnetic mediums. The general formulation of the RCWA for bianisotropic materials is provided in [34]. Here, we present its specialization to isotropic dielctric and magnetic materials.

The plan of this chapter is as follows: boundary-value problem is given in Section 2.1. Fourier expansions of field and material properties are presented in Section 2.2. Coupled equations derived from Maxwell equations are given in Section 2.3. Fields at the boundaries are computed in Section 2.4, and solution algorithm is discussed in Section 2.5. A detailed formulation is discussed for stable algorithm for the implementation of the RCWA in Section 2.6. The relations for the absorptances are given in Section 2.7, and time-averaged Poynting vectors are given in Section 2.8. The numerical results showing the convergence of the RCWA are presented and discussed in Section 2.9.

2.1 Boundary-Value Problem

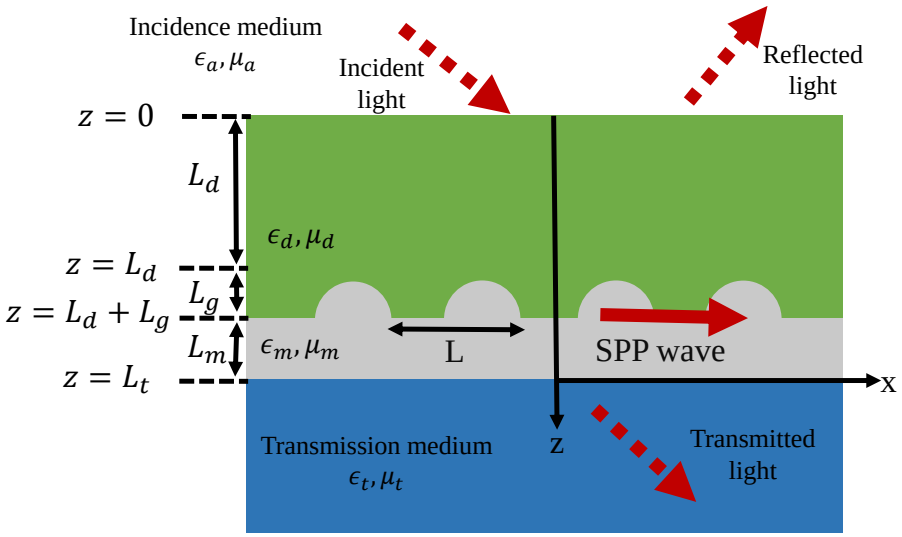

Fig. 2.1 Schematic of the geometry of the boundary-value problem. It consists of a surface-relief grating in the region $L_d < z < L_d + L_g$. Here $L_t = L_d + L_g + L_m$.

Let us consider the geometry of the problem as shown in Fig. 2.1. We have a surface-relief grating at the interface of two dissimilar dielectric-magnetic mediums. The half-space $z < 0$ is the incidence medium with the relative permittivity ε_a and the relative permeability μ_a. The region $0 \leqslant z \leqslant L_d$ is a homogeneous dielectric-magnetic medium with the relative permittivity ε_d and the relative permeability μ_d. For extension to multi-layer as well, a homogeneous layer of another dielectric-magnetic medium occupying the region $L_d + L_g \leqslant z \leqslant L_t$, $L_t = L_d + L_g + L_m$, is taken with the relative permittivity and relative permeability ε_m and μ_m, respectively. The region between $z = L_d$ and $z = L_d + L_g$ is a surface-relief grating with period L along the x axis and depth L_g, with the relative permittivity $\varepsilon_g(x,z) = \varepsilon_g(x \pm L, z)$ and the relative permeability $\mu_g(x,z) = \mu_g(x \pm L, z)$. The region $z > L_t$ is a semi-infinite transmission medium with the relative permittivity ε_t and the relative permeability μ_t.

Let a plane wave propagating in the region $z < 0$, making an angle θ with the z axis be incident on $z = 0$ interface. The incident, reflected, and transmitted electric and magnetic

field phasors in terms of Floquet harmonics can be written as [34].

$$\mathbf{E}_{\text{inc}}(\mathbf{r}) = \sum_{\ell\in\mathbb{Z}} \left[\hat{\mathbf{s}}_\ell a_s^{(\ell)} + \hat{\mathbf{p}}_\ell^+ a_p^{(\ell)}\right] \exp\left\{i[k_x^{(\ell)}x + k_{za}^{(\ell)}z]\right\}, \quad z \leqslant 0\,, \tag{2.1}$$

$$\eta_0\mathbf{H}_{\text{inc}}(\mathbf{r}) = n_a \sum_{\ell\in\mathbb{Z}} \left[\hat{\mathbf{p}}_\ell^+ a_s^{(\ell)} - \hat{\mathbf{s}}_\ell a_p^{(\ell)}\right] \exp\left\{i[k_x^{(\ell)}x + k_{za}^{(\ell)}z]\right\}, \quad z \leqslant 0\,, \tag{2.2}$$

$$\mathbf{E}_{\text{ref}}(\mathbf{r}) = \sum_{\ell\in\mathbb{Z}} \left[\hat{\mathbf{s}}_\ell r_s^{(\ell)} + \hat{\mathbf{p}}_\ell^- r_p^{(\ell)}\right] \exp\left\{i[k_x^{(\ell)}x - k_{za}^{(\ell)}z]\right\}, \quad z \leqslant 0\,, \tag{2.3}$$

$$\eta_0\mathbf{H}_{\text{ref}}(\mathbf{r}) = n_a \sum_{\ell\in\mathbb{Z}} \left[\hat{\mathbf{p}}_\ell^- r_s^{(\ell)} - \hat{\mathbf{s}}_\ell r_p^{(\ell)}\right] \exp\left\{i[k_x^{(\ell)}x - k_{za}^{(\ell)}z]\right\}, \quad z \leqslant 0\,, \tag{2.4}$$

$$\mathbf{E}_{\text{tr}}(\mathbf{r}) = \sum_{\ell\in\mathbb{Z}} \left[\hat{\mathbf{s}}_\ell t_s^{(\ell)} + \hat{\mathbf{p}}_\ell^t t_p^{(\ell)}\right] \exp\left\{i[k_x^{(\ell)}x + k_{zt}^{(\ell)}(z - L_t)]\right\}, \quad z \geqslant L_t\,, \tag{2.5}$$

$$\eta_0\mathbf{H}_{\text{tr}}(\mathbf{r}) = n_t \sum_{\ell\in\mathbb{Z}} \left[\hat{\mathbf{p}}_\ell^t t_s^{(\ell)} - \hat{\mathbf{s}}_\ell t_p^{(\ell)}\right] \exp\left\{i[k_x^{(\ell)}x + k_{zt}^{(\ell)}(z - L_t)]\right\}, \quad z \geqslant L_t\,, \tag{2.6}$$

where

$$k_x^{(\ell)} = k_0 n_a \sin\theta + \ell\kappa_x\,,\ \kappa_x = 2\pi/L, \tag{2.7}$$

$$k_{za}^{(\ell)} = \sqrt{\left[k_0 n_a\right]^2 - \left[k_x^{(\ell)}\right]^2}\,, \tag{2.8}$$

$$k_{zt}^{(\ell)} = \sqrt{\left[k_0 n_t\right]^2 - \left[k_x^{(\ell)}\right]^2}\,. \tag{2.9}$$

In Eqs. (2.1)–(2.6), $a_s^{(0)}$ and $a_p^{(0)}$ are the amplitudes of the *s*- and *p*-polarized incident plane waves, respectively, and $a_s^{(\ell)} = a_p^{(\ell)} = 0 \forall\, \ell \neq 0$. Furthermore, $r_s^{(\ell)}$ and $t_s^{(\ell)}$ are unknown amplitudes of the Floquet harmonics of order ℓ in the *s*-polarized reflected and transmitted fields, respectively. Similarly, $r_p^{(\ell)}$ and $t_p^{(\ell)}$ are the amplitudes of the Floquet harmonics of order ℓ in the *p*-polarized reflected and transmitted fields, respectively, where ℓ is the order of Floquet harmonics with $\ell \in \{0, \pm1, \pm2, \pm3...\}$. Let us note that $\ell = 0$ represents the specular component of the reflected and transmitted field, and $\ell \neq 0$ are the non-specular components. Specular reflection from a surface is known as a regular reflection in which incident ray is reflected at the same angle with the surface normal as the incident ray. On the other hand, whenever we have some irregular surface we get non-specular reflection. In non-specular reflection, the reflected rays reflect at different angles than the incidence angle.

The *s*-polarization state is represented by the unit vector

$$\hat{\mathbf{s}}_\ell = \hat{\mathbf{u}}_y\,, \tag{2.10}$$

the p-polarization state of the incident and reflected waves is represented by

$$\hat{\mathbf{p}}_\ell^{\pm} = \frac{\mp k_{za}^{(\ell)} \hat{\mathbf{u}}_x + k_x^{(\ell)} \hat{\mathbf{u}}_z}{k_0 n_a}, \tag{2.11}$$

and the p-polarization state of the transmitted wave is represented by

$$\hat{\mathbf{p}}_\ell^{t} = \frac{k_{zt}^{(\ell)} \hat{\mathbf{u}}_x + k_x^{(\ell)} \hat{\mathbf{u}}_z}{k_0 n_t}. \tag{2.12}$$

2.2 Expansions of Fields and Material Properties

The constitutive relations can be written as

$$\left.\begin{aligned} \mathbf{D}(\mathbf{r}) &= \varepsilon_0 \varepsilon(x,z)\mathbf{E}(\mathbf{r}) \\ \mathbf{B}(\mathbf{r}) &= \mu_0 \mu(x,z)\mathbf{H}(\mathbf{r}) \end{aligned}\right\}, \quad z \in [0, L_t]. \tag{2.13}$$

The RCWA demands that all the field phasors, permittivity and permeability are expressed as Fourier series with respect to x [29, 30, 34]. Fourier series for the permittivity and the permeability can be written as

$$\varepsilon(x,z) = \sum_{\ell=-\infty}^{\infty} \varepsilon^{(\ell)}(z) \exp(i\ell\kappa_x x), \quad z \in [0, L_t], \tag{2.14}$$

and

$$\mu(x,z) = \sum_{\ell=-\infty}^{\infty} \mu^{(\ell)}(z) \exp(i\ell\kappa_x x), \quad z \in [0, L_t], \tag{2.15}$$

respectively, where

$$\varepsilon^{(0)}(z) = \begin{cases} \varepsilon_d, & z \in [0, L_d], \\ \frac{1}{L}\int_0^L \varepsilon_g(x,z)dx, & z \in (L_d, L_d + L_g), \\ \varepsilon_m, & z \in [L_d + L_g, L_t], \end{cases} \tag{2.16}$$

$$\mu^{(0)}(z) = \begin{cases} \mu_d, & z \in [0, L_d], \\ \frac{1}{L}\int_0^L \mu_g(x,z)dx, & z \in (L_d, L_d + L_g), \\ \mu_m, & z \in [L_d + L_g, L_t], \end{cases} \tag{2.17}$$

and

$$\varepsilon^{(\ell)}(z) = \begin{cases} \frac{1}{L}\int_0^L \varepsilon_g(x,z)\exp(-i\ell\kappa_x x)dx, & \ell \neq 0, \quad z \in (L_d, L_d+L_g), \\ 0, & \text{otherwise}, \end{cases} \tag{2.18}$$

$$\mu^{(\ell)}(z) = \begin{cases} \frac{1}{L}\int_0^L \mu_g(x,z)\exp(-i\ell\kappa_x x)dx, & \ell \neq 0, \quad z \in (L_d, L_d+L_g), \\ 0, & \text{otherwise}. \end{cases} \tag{2.19}$$

Similarly, the field phasors in terms of Floquet harmonics in region $0 \leqslant z \leqslant L_t$ can be written as

$$\left.\begin{aligned} \mathbf{E}(\mathbf{r}) &= \sum_{\ell=-\infty}^{\infty}\left[E_x^{(\ell)}(z)\hat{\mathbf{u}}_x + E_y^{(\ell)}(z)\hat{\mathbf{u}}_y + E_z^{(\ell)}(z)\hat{\mathbf{u}}_z\right]\exp\left\{i[k_x^{(\ell)}x]\right\} \\ \mathbf{H}(\mathbf{r}) &= \sum_{\ell=-\infty}^{\infty}\left[H_x^{(\ell)}(z)\hat{\mathbf{u}}_x + H_y^{(\ell)}(z)\hat{\mathbf{u}}_y + H_z^{(\ell)}(z)\hat{\mathbf{u}}_z\right]\exp\left\{i[k_x^{(\ell)}x]\right\} \end{aligned}\right\}, \quad z \in [0, L_t]. \tag{2.20}$$

2.3 Coupled Equations

The source-free Maxwell equations in the frequency-domain are given by

$$\bigtriangledown \times \mathbf{E}(\mathbf{r},\omega) = i\omega\mu(z)\mathbf{H}(\mathbf{r},\omega), \tag{2.21}$$

$$\bigtriangledown \times \mathbf{H}(\mathbf{r},\omega) = -i\omega\varepsilon(z)\mathbf{E}(\mathbf{r},\omega), \tag{2.22}$$

$$\bigtriangledown \cdot \mathbf{E}(\mathbf{r},\omega) = 0, \tag{2.23}$$

$$\bigtriangledown \cdot \mathbf{H}(\mathbf{r},\omega) = 0. \tag{2.24}$$

Substituting Eqs. (2.14), (2.15), and (2.20) in Maxwell curl postulates given in Eqs. (2.21) and (2.22), along with the constitute relations given in Eq. (2.13), we get four ordinary differential equations and two algebraic equations, given by

$$\frac{d}{dz}E_x^{(\ell)}(z) - ik_x^{(\ell)}E_z^{(\ell)}(z) = ik_0\eta_0\sum_{m=-\infty}^{\infty}\mu^{(\ell-m)}(z)H_y^{(m)}(z), \tag{2.25}$$

$$\frac{d}{dz}E_y^{(\ell)}(z) = -ik_0\eta_0 \sum_{m=-\infty}^{\infty} \mu^{(\ell-m)}(z)H_x^{(m)}(z)\,, \tag{2.26}$$

$$k_x^{(\ell)}E_y^{(\ell)}(z) = k_0\eta_0 \sum_{m=-\infty}^{\infty} \mu^{(\ell-m)}(z)H_z^{(m)}(z)\,, \tag{2.27}$$

$$\frac{d}{dz}H_x^{(\ell)}(z) - ik_x^{(\ell)}H_z^{(\ell)}(z) = -\frac{ik_0}{\eta_0} \sum_{m=-\infty}^{\infty} \varepsilon^{(\ell-m)}(z)E_y^{(m)}(z)\,, \tag{2.28}$$

$$\frac{d}{dz}H_y^{(\ell)}(z) = \frac{ik_0}{\eta_0} \sum_{m=-\infty}^{\infty} \varepsilon^{(\ell-m)}(z)E_x^{(m)}(z)\,, \tag{2.29}$$

$$k_x^{(\ell)}H_y^{(\ell)}(z) = -\frac{k_0}{\eta_0} \sum_{m=-\infty}^{\infty} \varepsilon^{(\ell-m)}(z)E_z^{(m)}(z)\,. \tag{2.30}$$

The sums in Eqs. (2.25)–(2.30) contain infinite terms. Implementation of these sums on a computer requires the truncation of the series to a finite number of terms. An approximation is obtained by restricting the series between $\ell \in [-N_t, N_t]$. Defining column $(2N_t+1)$-vectors

$$[\mathbf{X}_\sigma^{(n)}(z)] = [X_\sigma^{(-N_t)}(z), X_\sigma^{(-N_t+1)}(z), ..., X_\sigma^{(0)}(z), ..., X_\sigma^{(N_t-1)}(z), X_\sigma^{(N_t)}(z)]^T\,, \tag{2.31}$$

where $\mathbf{X} \in \{E, H\}$ and $\sigma \in \{x, y, z\}$, $(2N_t+1)\times(2N_t+1)$-diagonal matrix

$$\left[\underline{\underline{K}}_x\right] = \text{diag}\left[k_x^{(\ell)}\right]\,, \tag{2.32}$$

and $(2N_t+1)\times(2N_t+1)$-square matrices

$$\left[\underline{\underline{\varepsilon}}(z)\right] = \left[\varepsilon^{(\ell-m)}(z)\right]\,, \quad \left[\underline{\underline{\mu}}(z)\right] = \left[\mu^{(\ell-m)}(z)\right]\,, \tag{2.33}$$

Eqs. (2.27) and (2.30) give

$$\left[\mathbf{H}_z(z)\right] = \frac{1}{\eta_0 k_0}\left[\underline{\underline{\mu}}(z)\right]^{-1} \cdot \left(\left[\underline{\underline{K}}_x\right] \cdot \left[\mathbf{E}_y(z)\right]\right) \tag{2.34}$$

and

$$\left[\mathbf{E}_z(z)\right] = -\frac{\eta_0}{k_0}\left[\underline{\underline{\varepsilon}}(z)\right]^{-1} \cdot \left(\left[\underline{\underline{K}}_x\right] \cdot \left[\mathbf{H}_y(z)\right]\right). \tag{2.35}$$

Substituting Eqs. (2.34) and (2.35) back in Eqs. (2.25), (2.26), (2.28), and (2.29) and eliminating $E_z^{(\ell)}(z)$ and $H_z^{(\ell)}(z)$, we obtained matrix ordinary differential equation

$$\frac{d}{dz}[\mathbf{f}(z)] = i\left[\underline{\underline{P}}(z)\right] \cdot [\mathbf{f}(z)]\,, \qquad z \in (0, L_t)\,, \tag{2.36}$$

where $[\mathbf{f}(z)]$ is a column vector with $4(2N_t+1)$ components given as

$$[\mathbf{f}(z)] = \left[[\mathbf{E}_x(z)]^T, [\mathbf{E}_y(z)]^T, \eta_0[\mathbf{H}_x(z)]^T, \eta_0[\mathbf{H}_y(z)]^T\right]^T, \tag{2.37}$$

and $4(2N_t+1)\times 4(2N_t+1)$-matrix $[\underline{\underline{P}}(z)]$ is

$$\left[\underline{\underline{P}}(z)\right] = \begin{bmatrix} [\underline{\underline{0}}] & [\underline{\underline{0}}] & [\underline{\underline{0}}] & \left[\underline{\underline{P}}_{14}(z)\right] \\ [\underline{\underline{0}}] & [\underline{\underline{0}}] & \left[\underline{\underline{P}}_{23}(z)\right] & [\underline{\underline{0}}] \\ [\underline{\underline{0}}] & \left[\underline{\underline{P}}_{32}(z)\right] & [\underline{\underline{0}}] & [\underline{\underline{0}}] \\ \left[\underline{\underline{P}}_{41}(z)\right] & [\underline{\underline{0}}] & [\underline{\underline{0}}] & [\underline{\underline{0}}] \end{bmatrix}, \tag{2.38}$$

with

$$[\underline{\underline{P}}_{14}(z)] = k_0[\underline{\underline{\mu}}(z)] - \frac{1}{k_0}[\underline{\underline{K}}_x]\cdot[\underline{\underline{\varepsilon}}(z)]^{-1}\cdot[\underline{\underline{K}}_x], \tag{2.39}$$

$$[\underline{\underline{P}}_{23}(z)] = -k_0[\underline{\underline{\mu}}(z)], \tag{2.40}$$

$$[\underline{\underline{P}}_{32}(z)] = \frac{1}{k_0}[\underline{\underline{K}}_x]\cdot[\underline{\underline{\mu}}(z)]^{-1}\cdot[\underline{\underline{K}}_x] - k_0[\underline{\underline{\varepsilon}}(z)], \tag{2.41}$$

$$[\underline{\underline{P}}_{41}(z)] = k_0[\underline{\underline{\varepsilon}}(z)], \tag{2.42}$$

where $[\underline{\underline{0}}]$ is a $(2N_t+1)\times(2N_t+1)$-null matrix.

2.4 Fields at Boundaries

To implement the boundary conditions at the $z=0$ and $z=L_t$ interfaces, the column field vectors are required at these boundaries. The column vectors $[\mathbf{f}(0)]$ and $[\mathbf{f}(L_t)]$ can be obtained using Eqs. (2.1)–(2.6) as

$$\left[\mathbf{f}(0)\right] = \begin{bmatrix} [\underline{\underline{Y}}_e^{\text{inc}}] & [\underline{\underline{Y}}_e^{\text{ref}}] \\ [\underline{\underline{Y}}_h^{\text{inc}}] & [\underline{\underline{Y}}_h^{\text{ref}}] \end{bmatrix} \cdot \begin{bmatrix} [\mathbf{A}] \\ [\mathbf{R}] \end{bmatrix}, \tag{2.43}$$

and

$$\left[\mathbf{f}(L_t)\right] = \begin{bmatrix} [\underline{\underline{Y}}_e^{\text{tr}}] \\ [\underline{\underline{Y}}_h^{\text{tr}}] \end{bmatrix} \cdot \left[\mathbf{T}\right], \tag{2.44}$$

where the column vectors for the incident, reflected and transmitted amplitudes for *s*- and *p*-polarized components are defined as

$$[\mathbf{A}] = \left[a_s^{(-N_t)}, a_s^{(-N_t+1)}, ..., a_s^{(0)}, ..., a_s^{(N_t-1)}, a_s^{(N_t)}, a_p^{(-N_t)}, a_p^{(-N_t+1)}, ..., a_p^{(0)}, ..., a_p^{(N_t-1)}, a_p^{(N_t)}\right]^T, \tag{2.45}$$

$$[\mathbf{R}] = \left[r_s^{(-N_t)}, r_s^{(-N_t+1)}, ..., r_s^{(0)}, ..., r_s^{(N_t-1)}, r_s^{(N_t)}, r_p^{(-N_t)}, r_p^{(-N_t+1)}, ..., r_p^{(0)}, ..., r_p^{(N_t-1)}, r_p^{(N_t)}\right]^T, \tag{2.46}$$

$$[\mathbf{T}] = \left[t_s^{(-N_t)}, t_s^{(-N_t+1)}, ..., t_s^{(0)}, ..., t_s^{(N_t-1)}, t_s^{(N_t)}, t_p^{(-N_t)}, t_p^{(-N_t+1)}, ..., t_p^{(0)}, ..., t_p^{(N_t-1)}, t_p^{(N_t)}\right]^T. \tag{2.47}$$

The other $(2N_t+1)\times(2N_t+1)$-matrices are obtained as

$$\left[\underline{\underline{Y}}_e^{\text{inc}}\right] = \frac{1}{k_0 n_a}\begin{bmatrix}[\underline{0}] & -\left[\underline{\underline{K}}_{za}\right] \\ [\underline{I}] & [\underline{0}]\end{bmatrix}, \tag{2.48}$$

$$\left[\underline{\underline{Y}}_h^{\text{inc}}\right] = \frac{1}{k_0}\begin{bmatrix}-\left[\underline{\underline{K}}_{za}\right] & [\underline{0}] \\ [\underline{0}] & -n_a k_0\,[\underline{I}]\end{bmatrix}, \tag{2.49}$$

$$\left[\underline{\underline{Y}}_e^{\text{ref}}\right] = \frac{1}{k_0 n_a}\begin{bmatrix}[\underline{0}] & \left[\underline{\underline{K}}_{za}\right] \\ [\underline{I}] & [\underline{0}]\end{bmatrix}, \tag{2.50}$$

$$\left[\underline{\underline{Y}}_h^{\text{ref}}\right] = \frac{1}{k_0}\begin{bmatrix}\left[\underline{\underline{K}}_{za}\right] & [\underline{0}] \\ [\underline{0}] & -n_a k_0\,[\underline{I}]\end{bmatrix}, \tag{2.51}$$

$$\left[\underline{\underline{Y}}_e^{\text{tr}}\right] = \frac{1}{k_0 n_t}\begin{bmatrix}[\underline{0}] & -\left[\underline{\underline{K}}_{zt}\right] \\ [\underline{I}] & [\underline{0}]\end{bmatrix}, \tag{2.52}$$

$$\left[\underline{\underline{Y}}_h^{\text{tr}}\right] = \frac{1}{k_0}\begin{bmatrix}-\left[\underline{\underline{K}}_{zt}\right] & [\underline{0}] \\ [\underline{0}] & -n_t k_0\,[\underline{I}]\end{bmatrix}, \tag{2.53}$$

where

$$\left[\underline{\underline{K}}_{za}\right] = \text{diag}\left[k_{za}^{(\ell)}\right], \tag{2.54}$$

$$\left[\underline{\underline{K}}_{zt}\right] = \text{diag}\left[k_{zt}^{(\ell)}\right], \tag{2.55}$$

and $[\underline{I}]$ is the $(2N_t+1)\times(2N_t+1)$ identity matrix.

2.5 Solution Algorithm

The matrix $[\underline{\underline{P}}(z)]$ in Eq. (2.38) is z dependent. In order to solve this differential equation, the region between $0 \leqslant z \leqslant L_t$ is divided into small slices parallel to xy plane, so that in each slice the matrix $[\underline{\underline{P}}(z)]$ remains constant. The region $0 \leq z \leq L_d$ is divided into N_d slices, the region $L_d \leq z \leq L_d + L_g$ is divided into N_g slices, and the region $L_d + L_g \leq z \leq L_t$ is divided into N_m slices. Thus the total number of slices is $N_s = N_d + N_g + N_m$. Let us consider the jth slice, where $j \in [1, N_s]$, bounded by the planes $z = z_{j-1}$ and $z = z_j$, and approximate

$$\left[\underline{\underline{P}}(z)\right] = \left[\underline{\underline{P}}\right]_j = \left[\underline{\underline{P}}\left(\frac{z_j + z_{j-1}}{2}\right)\right]. \tag{2.56}$$

Now, the solution of differential Eq. (2.36) is given by

$$\left[\mathbf{f}(z_j)\right] = \left[\underline{\underline{X}}\right]_j \cdot \left[\mathbf{f}(z_{j-1})\right], \qquad j \in [1, Ns], \tag{2.57}$$

where

$$\left[\underline{\underline{X}}\right]_j = \exp\left\{i \triangle_j \left[\underline{\underline{P}}\right]_j\right\}, \qquad j \in [1, Ns], \tag{2.58}$$

and $\triangle_j = z_j - z_{j-1}$. Repeated use of Eq. (2.57) at the boundaries give

$$\left[\mathbf{f}(L_t)\right] = \left[\underline{\underline{X}}\right]^{(N_s)} \cdot \left[\underline{\underline{X}}\right]^{(N_s-1)} \ldots \left[\underline{\underline{X}}\right]^{(2)} \cdot \left[\underline{\underline{X}}\right]^{(1)} \cdot \left[\mathbf{f}(0)\right]. \tag{2.59}$$

Using Eqs. (2.43), (2.44), and (2.59), we get

$$\begin{bmatrix} [\underline{\underline{Y}}_e^{\mathrm{tr}}] \\ [\underline{\underline{Y}}_h^{\mathrm{tr}}] \end{bmatrix} \cdot \left[\mathbf{T}\right] = \left[\underline{\underline{X}}\right]^{(N_s)} \cdot \left[\underline{\underline{X}}\right]^{(N_s-1)} \ldots \left[\underline{\underline{X}}\right]^{(2)} \cdot \left[\underline{\underline{X}}\right]^{(1)} \cdot \begin{bmatrix} [\underline{\underline{Y}}_e^{\mathrm{inc}}] & [\underline{\underline{Y}}_e^{\mathrm{ref}}] \\ [\underline{\underline{Y}}_h^{\mathrm{inc}}] & [\underline{\underline{Y}}_h^{\mathrm{ref}}] \end{bmatrix} \cdot \begin{bmatrix} [\mathbf{A}] \\ [\mathbf{R}] \end{bmatrix}. \tag{2.60}$$

Solving Eq. (2.60) for $[\mathbf{R}]$ and $[\mathbf{T}]$, we can write

$$\begin{bmatrix} [\underline{\underline{Y}}_e^{\mathrm{tr}}] \\ [\underline{\underline{Y}}_h^{\mathrm{tr}}] \end{bmatrix} \cdot \left[\mathbf{T}\right] = \left[\underline{\underline{Q}}\right] \cdot \begin{bmatrix} [\underline{\underline{Y}}_e^{\mathrm{inc}}] & [\underline{\underline{Y}}_e^{\mathrm{ref}}] \\ [\underline{\underline{Y}}_h^{\mathrm{inc}}] & [\underline{\underline{Y}}_h^{\mathrm{ref}}] \end{bmatrix} \cdot \begin{bmatrix} [\mathbf{A}] \\ [\mathbf{R}] \end{bmatrix}, \tag{2.61}$$

where $\left[\underline{\underline{Q}}\right] = \left[\underline{\underline{X}}\right]^{(N_s)} \cdot \left[\underline{\underline{X}}\right]^{(N_s-1)} \ldots \left[\underline{\underline{X}}\right]^{(2)} \cdot \left[\underline{\underline{X}}\right]^{(1)}$. Hence

$$\begin{bmatrix} [\mathbf{T}] \\ [\mathbf{R}] \end{bmatrix} = \begin{bmatrix} [\underline{\underline{Y}}_e^{\mathrm{tr}}] & -[\underline{\underline{Q}}] \begin{bmatrix} [\underline{\underline{Y}}_e^{\mathrm{ref}}] \\ [\underline{\underline{Y}}_h^{\mathrm{ref}}] \end{bmatrix} \\ [\underline{\underline{Y}}_h^{\mathrm{tr}}] \end{bmatrix}^{-1} \left[\underline{\underline{Q}}\right] \cdot \begin{bmatrix} [\underline{\underline{Y}}_e^{\mathrm{inc}}] \\ [\underline{\underline{Y}}_h^{\mathrm{inc}}] \end{bmatrix} \cdot \left[\mathbf{A}\right]. \tag{2.62}$$

In Eq. (2.62), finding the inverse of matrix is difficult. It is because the matrix is ill-conditioned. A stable algorithm is adopted to overcome the problem of ill-conditioning in the matrix.

2.6 Stable RCWA Algorithm

To solve the problem of ill-conditioning in matrix in Eq. (2.62), we will implement a stable algorithm [5, 29, 30, 34]. We need to diagonalize the matrix $\left[\underline{\underline{P}}\right]_j$. Now the solution of Eq. (2.36) takes the form in one slice

$$\left[\mathbf{f}(z_{j-1})\right] = \left[\underline{\underline{G}}\right]_j \cdot \exp\left\{-i\triangle_j \left[\underline{\underline{D}}\right]_j\right\} \cdot \left[\underline{\underline{G}}\right]_j^{-1} \cdot \left[\mathbf{f}(z_j)\right], \tag{2.63}$$

with

$$\left[\underline{\underline{P}}\right]_j = \left[\underline{\underline{G}}\right]_j \cdot \left[\underline{\underline{D}}\right]_j \cdot \left[\underline{\underline{G}}\right]_j^{-1}, \tag{2.64}$$

where $\left[\underline{\underline{G}}\right]_j$ has eigenvectors of $\left[\underline{\underline{P}}\right]_j$ on its columns, and diagonal matrix $\left[\underline{\underline{D}}\right]_j$ comprises of the eigenvalues of $\left[\underline{\underline{P}}\right]_j$. The eigenvalues in $\left[\underline{\underline{D}}\right]_j$ are arranged in the decreasing order of imaginary part, and each eigenvector in $\left[\underline{\underline{G}}\right]_j$ is also at the same position as corresponding eigenvalue in $\left[\underline{\underline{D}}\right]_j$. Defining auxiliary matrices $\left[\underline{\underline{Z}}\right]_j$ and $\left[\mathbf{T}\right]_j$, we can write

$$\left[\mathbf{f}(z_j)\right] = \left[\underline{\underline{Z}}\right]_j \cdot \left[\mathbf{T}\right]_j, \qquad j \in [0, N_s], \tag{2.65}$$

and

$$\left[\mathbf{T}\right]_{N_s} = \left[\mathbf{T}\right], \tag{2.66}$$

and

$$\left[\underline{\underline{Z}}\right]_{N_s} = \begin{bmatrix} [\underline{\underline{Y}}_e^{\mathrm{tr}}] \\ [\underline{\underline{Y}}_h^{\mathrm{tr}}] \end{bmatrix}. \tag{2.67}$$

Substituting Eq. (2.65) in Eq. (2.63), we get

$$\left[\underline{\underline{Z}}\right]_{j-1} \cdot \left[\mathbf{T}\right]_{j-1} = \left[\underline{\underline{G}}\right]_j \cdot \begin{bmatrix} e^{-i\triangle_j [\underline{\underline{D}}]_j^u} & 0 \\ 0 & e^{-i\triangle_j [\underline{\underline{D}}]_j^l} \end{bmatrix} \cdot \left[\underline{\underline{G}}\right]_j^{-1} \cdot \left[\underline{\underline{Z}}\right]_j \cdot \left[\mathbf{T}\right]_j, \tag{2.68}$$

where $\left[\underline{\underline{D}}\right]_j^u$ and $\left[\underline{\underline{D}}\right]_j^l$ are upper and lower diagonal submatrices of matrix $\left[\underline{\underline{D}}\right]_j$, when eigenvalues are arranged in the decreasing order of the imaginary part. From Eq. (2.68), we

can define that

$$\left[\mathbf{T}\right]_{j-1} = \exp\left\{-i\triangle_j \left[\underline{\underline{D}}\right]_j^u\right\} \cdot \left[\underline{\underline{W}}\right]_j^u \cdot \left[\mathbf{T}\right]_j, \tag{2.69}$$

where matrices $\left[\underline{\underline{W}}\right]_j^u$ and $\left[\underline{\underline{W}}\right]_j^l$ are defined as

$$\begin{bmatrix} [\underline{\underline{W}}]_j^u \\ [\underline{\underline{W}}]_j^l \end{bmatrix} = \left[\underline{\underline{G}}\right]_j^{-1} \cdot \left[\underline{\underline{Z}}\right]_j. \tag{2.70}$$

Substituting Eq. (2.69) in Eq. (2.68) gives

$$\left[\underline{\underline{Z}}\right]_{j-1} = \left[\underline{\underline{G}}\right]_j \cdot \begin{bmatrix} [\underline{\underline{I}}] \\ \exp\{-i\triangle_j [\underline{\underline{D}}]_j^l\} \cdot [\underline{\underline{W}}]_j^l \cdot \{[\underline{\underline{W}}]_j^u\}^{-1} \cdot \exp\{i\triangle_j [\underline{\underline{D}}]_j^u\} \end{bmatrix}. \tag{2.71}$$

Finally, we can write $\left[\mathbf{R}\right]$ and $\left[\mathbf{T}\right]_0$ by using Eqs. (2.43), (2.44) and (2.65) as

$$\begin{bmatrix} [\mathbf{T}]_0 \\ [\mathbf{R}] \end{bmatrix} = \begin{bmatrix} [\underline{\underline{Z}}]_0^u & -[\underline{\underline{Y}}_e^{\text{ref}}] \\ [\underline{\underline{Z}}]_0^l & -[\underline{\underline{Y}}_h^{\text{ref}}] \end{bmatrix}^{-1} \cdot \begin{bmatrix} [\underline{\underline{Y}}_e^{\text{inc}}] \\ [\underline{\underline{Y}}_h^{\text{inc}}] \end{bmatrix} \cdot \left[\mathbf{A}\right], \tag{2.72}$$

where

$$\left[\underline{\underline{Z}}\right]_0 = \begin{bmatrix} [\underline{\underline{Z}}]_0^u \\ [\underline{\underline{Z}}]_0^l \end{bmatrix}. \tag{2.73}$$

From Eq. (2.72), we can find $\left[\mathbf{T}\right]_0$, and $\left[\mathbf{T}\right] = \left[\mathbf{T}\right]_{N_s}$ can be found by reversing the iteration in Eq. (2.69).

2.7 Absorptances

After the amplitudes are computed, the total absorptances for the *s*- and *p*-polarized incident plane waves can be computed as [74] as

$$A_s = 1 - \sum_{\ell=-N_t}^{N_t} \frac{|r_s^{(\ell)}|^2 + |r_p^{(\ell)}|^2}{|a_s^{(0)}|^2} \text{Re}\left(\frac{k_{za}^{(\ell)}}{k_{za}^{(0)}}\right) - \sum_{\ell=-N_t}^{N_t} \frac{|t_s^{(\ell)}|^2 + |t_p^{(\ell)}|^2}{|a_s^{(0)}|^2} \text{Re}\left(\frac{k_{zt}^{(\ell)}}{k_{za}^{(0)}}\right)\Bigg|_{a_p^{(\ell)}=0} \tag{2.74}$$

and

$$A_p = 1 - \sum_{\ell=-N_t}^{N_t} \frac{|r_s^{(\ell)}|^2 + |r_p^{(\ell)}|^2}{|a_p^{(0)}|^2} \text{Re}\left(\frac{k_{za}^{(\ell)}}{k_{za}^{(0)}}\right) - \sum_{\ell=-N_t}^{N_t} \frac{|t_s^{(\ell)}|^2 + |t_p^{(\ell)}|^2}{|a_p^{(0)}|^2} \text{Re}\left(\frac{k_{zt}^{(\ell)}}{k_{za}^{(0)}}\right)\Bigg|_{a_s^{(\ell)}=0}, \tag{2.75}$$

respectively.

2.8 Time-Averaged Poynting Vector

When $\left[\mathbf{T}\right]_j$, $j \in [1, N_s]$, is known in each layer, we can find fields $\left[\mathbf{f}(z_j)\right]$ in each layer using Eq. (2.65). As a result, $\left[\mathbf{f}(z_j)\right]_j$ will give $[\mathbf{E}_x(z)]^T, [\mathbf{E}_y(z)]^T, [\mathbf{H}_x(z)]^T$, and $[\mathbf{H}_y(z)]^T$ in each layer using the Eq. (2.37). We can then use Eqs. (2.34) and (2.35) to find $[\mathbf{H}_z(z)]^T$ and $[\mathbf{E}_z(z)]^T$, respectively.

The instantaneous Poynting vector is defined as $\mathbf{E}(\mathbf{r},t) \times \mathbf{H}(\mathbf{r},t)$. The time-averaged Poynting vector is defined as

$$\mathbf{P}(\mathbf{r}) = \frac{1}{2}\mathrm{Re}\left[\mathbf{E}(\mathbf{r}) \times \mathbf{H}^*(\mathbf{r})\right], \tag{2.76}$$

where $(*)$ asterisk denotes complex conjugate. For s-polarization, three components of Poynting vector $\mathrm{P}_{x,s}$ are $\mathrm{P}_{y,s}$, and $\mathrm{P}_{z,s}$ are given by

$$\mathrm{P}_{x,s} = \frac{1}{2}\mathrm{Re}\left(\mathrm{E}_y \mathrm{H}_z^*\right), \tag{2.77}$$

$$\mathrm{P}_{y,s} = 0, \tag{2.78}$$

$$\mathrm{P}_{z,s} = -\frac{1}{2}\mathrm{Re}\left(\mathrm{E}_y \mathrm{H}_x^*\right), \tag{2.79}$$

and for the p-polarization state, three component of Poynting vector $\mathrm{P}_{x,p}$ are $\mathrm{P}_{y,p}$, and $\mathrm{P}_{z,p}$ are given by

$$\mathrm{P}_{x,p} = -\frac{1}{2}\mathrm{Re}\left(\mathrm{E}_z \mathrm{H}_y^*\right), \tag{2.80}$$

$$\mathrm{P}_{y,p} = 0, \tag{2.81}$$

$$\mathrm{P}_{z,p} = \frac{1}{2}\mathrm{Re}\left(\mathrm{E}_x \mathrm{H}_y^*\right). \tag{2.82}$$

2.9 Numerical Results And Discussion

We have implemented the RCWA to find the convergence of absorptances for both the s- and p-polarized incident plane waves. For this purpose, a surface-relief grating was chosen in the

region $L_d \leq z \leq L_d + L_g$ with the relative permittivity and the relative permeability as

$$\varepsilon_g(x,z) = \begin{cases} \varepsilon_m - [\varepsilon_m - \varepsilon_d]U\Big[L_d + L_g - z - g(x)\Big], x \in (0, 0.5L), \\ \varepsilon_d, \qquad\qquad\qquad\qquad\qquad\quad x \in (0.5L, L), \end{cases} \tag{2.83}$$

and

$$\mu_g(x,z) = \begin{cases} \mu_m - [\mu_m - \mu_d]U\Big[L_d + L_g - z - g(x)\Big], x \in (0, 0.5L), \\ \mu_d, \qquad\qquad\qquad\qquad\qquad\quad x \in (0.5L, L), \end{cases} \tag{2.84}$$

respectively, with sinusoidal bumps defined by

$$g(x) = L_g \sin(\frac{2\pi x}{L}), \quad x \in (0, 0.5L), \tag{2.85}$$

where

$$U(\alpha) = \begin{cases} 1, & \alpha \geqslant 0, \\ 0, & \alpha \leqslant 0, \end{cases} \tag{2.86}$$

is the unit step function.

For all the numerical results in this section, the free-space wavelength was set at $\lambda_0 = 800$ nm. The depth of the grating is fixed at $L_g = 50$ nm with a grating period of $L = 550$ nm, and thickness of the layer on top of the grating is fixed at $L_m = 30$ nm. The incidence and transmission mediums are considered to be air so that $\varepsilon_a = \mu_a = \varepsilon_t = \mu_t = 1$.

To check the convergence of the RCWA for the dielectric-magnetic grating, the absorptances (that require the computations of both the reflectances and transmittances) are computed for different values of the parameter N_t. Figure 2.2 shows the absorptances A_s for the s-polarized incidence as a function of the incidence angle θ for $N_t = 19$, 20, and 21. The other parameters are $N_d = 1$, $N_g = 50$, $N_m = 1$, $L_d = 900$ nm, $\varepsilon_d = 2$, $\mu_d = 1.5$, $\varepsilon_m = -20 + 1.5i$, and $\mu_m = 1.5 + 0.2i$. The figure clearly shows that the results are converged. Figure 2.3 shows the absrptances for a p-polarized incident plane wave as a function of the incidence angle for $N_t = 19$, 20, and 21, all other parameters are same as in Fig 2.2 . The figure shows pretty good convergence though the convergence is slightly worse for this case as compared to A_s and at the larger incidence angles at the absorptance peaks. However, the convergence is still acceptable as the change from $N_t = 19$ to 20 is less than $\pm 0.5\%$.

In the following chapters, the RCWA is applied to three problems that involve the periodic structures and 1D gratings. In these problems 1D gratings are illuminated from planar interface.

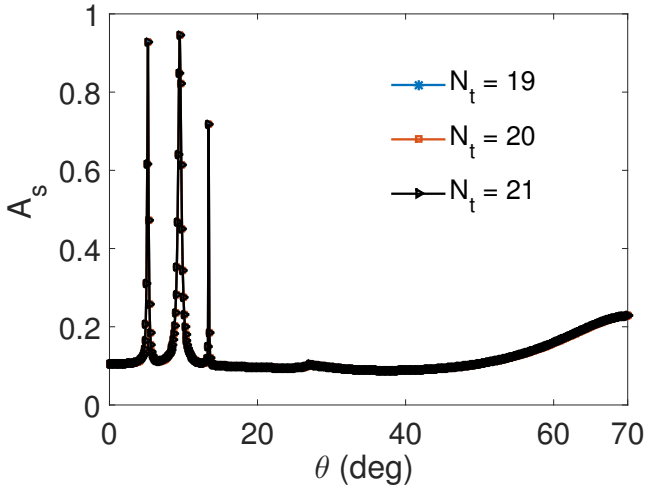

Fig. 2.2 Apsorptance for an *s*-polarized incident wave as a function of the incidence angle θ for $N_t = 19$, 20, and 21, when $L_d = 900$ nm, $L_g = 50$ nm, $L = 550$ nm, $N_d = 1$, $N_g = 50$, $N_m = 1$, $\varepsilon_d = 2$, $\mu_d = 1.5$, $\varepsilon_m = -20 + 1.5i$, and $\mu_m = 1.5 + 0.2i$.

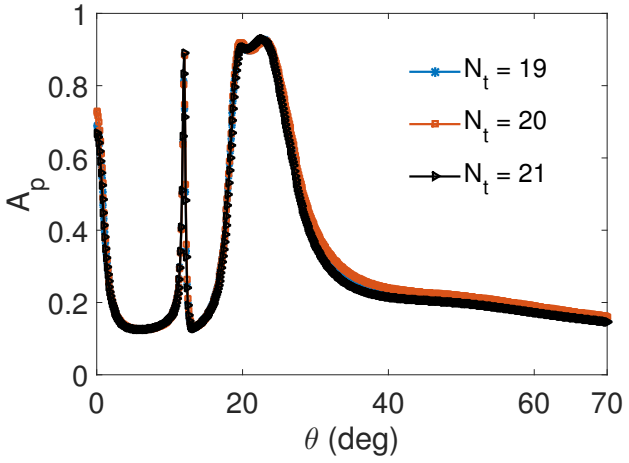

Fig. 2.3 Absorptance A_p as a function of the incidence angle θ for $N_t = 19$, 20, and 21, all other parameters are same as in Fig 2.2.

Chapter 3

Combination of Grating and Prism for Optical Sensing

In this chapter, surface plasmon-polariton (SPP) waves guided by an interface of a metal and a dielectric material with a combination of grating- and prism-coupled configurations are theoretically investigated for the optical sensing. Change in the refractive index of the partnering dielectric material is sensed by determining the change in the incidence angle and wavelength of excitation of the SPP waves. Two absorptance peaks are observed to determine the sensitivity for a single refractive index in the angular interrogation scheme. One peak corresponds to the prism-coupled configuration and the other peak to the grating-coupled configuration. The double sensing can increase the confidence in the optical measurements. The sensitivity of the proposed sensor is also investigated in the wavelength interrogation scheme. The plan of this chapter is as follows: The introduction and literature review is given in Section 3.1. For the analytical formulation, we used the rigorous coupled-wave approach which is briefly described in Section 3.2. The numerical results comparing the sensing with two types of SPP-wave-excitation are presented and discussed in Section 3.3, and the concluding remarks are presented in Section 3.4.

3.1 Introduction

The SPP waves are the electromagnetic surface waves that are excited at the metal/dielectric interface. The SPP waves are localized to the interface and decays away from that interface. This localization makes the SPP waves practically significant for sensitive (bio)chemical

This chapter is based on "Kamran and Faryad, Plasmonic sensor using a combination of grating and prism couplings, Plasmonics, **14**, 791–798 (2019)".

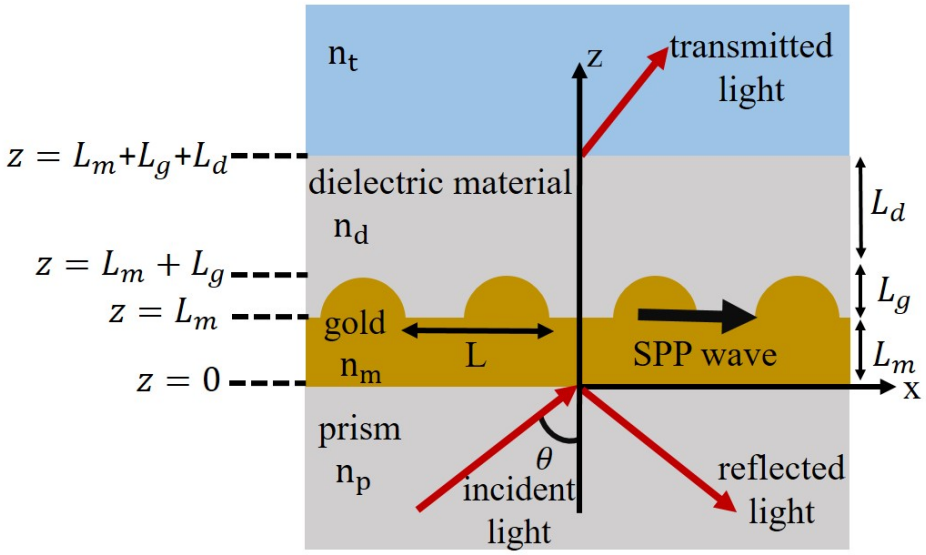

Fig. 3.1 Schematic of the geometry of the boundary-value problem. It is a combination of the prism-coupled configuration and the grating-coupled configuration.

sensors because these waves are very sensitive to the small changes in the electromagnetic properties of the partnering metal and dielectric material near the interface.

The SPP wave absorbs energy from the evanescent wave that results in a reduction in reflected light and increase in absorptance showing as a reflectance dip or an absorptance peak in the spectrum. This is often referred to as surface plasmon resonance (SPR). Most SPR sensing applications are developed using the prism-coupled configuration, for example, high performance SPR-based sensor [75], columnar thin film based SPR sensor [76], and biosensors that are capable of wavelength division multiplexing [77]. Another example of SPR based sensor is of DNA imaging in the prism-coupled configuration [78]. Several techniques have been developed to enhance the sensitivity of the prism coupling, including the use of magneto-optics [79], Michelson interferometer [80], and hyperbolic metamaterials [81, 82]. SPR sensors can be implemented in either the angular interrogation scheme for a fixed wavelength or in wavelength interrogation scheme for a fixed angle or a combination of both. The angular scheme affords wavelength division multiplexing whereas the wavelength scheme affords the angular division multiplexing; however, the angular scheme is more popular because it is simpler and offers wavelength division multiplexing [77, 83, 84]. In this work, we have reported both the angular and the wavelength scheme for the new geometry. The optical sensing based on the grating-coupled configuration has been studied extensively using the grating alone [85–90]. However, in all of these studies, the grating is illuminated

from the side of the dielectric material to be sensed and uses the effect of the grating alone to excite the SPP waves. In our problem, we propose an inverted scheme, as shown in Fig. 3.1, where the illumination is from the planar side of the grating so that a prism can also be used to combine the prim and the grating couplings.

Both the prism-coupled and the grating-coupled configurations are useful in designing optical sensors but offer different advantages. In the prism-coupled configuration, the chosen prism affects the angle of the incidence where an SPP wave is excited. Whereas in the grating-coupled configuration, it is the period of the grating that decides the angle of the incidence of incident light where an SPP wave is excited if everything else is kept the same. In the present work, we propose a new geometry for the excitation of the SPP waves that combines the grating and the prism-coupled configurations, as shown schematically in Fig. 3.1. A prism is attached to the planar metallic film that is corrugated from the other side. Since the metallic film is thin, the incident light couples with the periodic corrugations (grating) on the other side. The SPP waves are excited on the side of the grating, and the angle of incidence where they are excited is selected by both the prism refractive index and the grating period. By changing the prism, we can shift the incidence angle for the excitation of SPP wave. We can shift the absorptance peaks at the desired incidence angles. Thus, by combining the prism and the grating, we will be able to get more control over the incidence angle in addition to excite the SPP wave at two incidence angles, one using specular mode due to the prism and the other using the non-specular modes present due the grating. This is because the wavenumber of the incident light depends on the refractive index of the prism so that the wavenumber of the specularly and non-specularly scattered waves depend upon both the period of the grating and the wavenumber of the incidence angle. Therefore, in the work presented here, we set out to numerically analyze an optical sensor employing the combination of the prism- and the grating-coupled configurations. Let us note that this new scheme is possible because of excitation from the planar side of the grating.

3.2 Problem Description

Let us consider the geometry of the problem shown schematically in Fig. 3.1. We have a combination of the prism-coupled configuration and the grating-coupled configuration to excite the SPP waves. Since the prism is generally optically very thick, the prism is assumed to occupy the half-space $z < 0$ with a refractive index n_p. The region between $z > 0$ and $z < L_m$ is occupied by a metal of refractive index n_m and thickness L_m. The region between $z > L_m$ and $z < L_m + L_g$ is a surface-relief grating, with depth L_g and period L. Each period of the grating contains a sinusoidal bump of width $0.5L$. The shape of this type of grating is

chosen for the ease of fabrication. The region between $z > L_m + L_g$ and $z < L_m + L_g + L_d$ is occupied by a dielectric material of refractive index n_d and thickness L_d representing the fluid whose refractive index is to be sensed. The half-space $z > L_m + L_g + L_d$ is a semi-infinite medium with a refractive index n_t representing the transmission medium, which will be taken to be the same as the fluid for numerical results later since fluid is optically very thick in practical implementation. Taking the transmission medium to be the same as the fluid will also eliminate the excitation of the waveguide modes.

To study the excitation of the SPP waves, we need to calculate the absorptance for a p-polarized incident plane wave. The peaks in the absorptance spectra will then be analyzed to ascertain the excitation of the SPP waves. Therefore, let us consider a p-polarized incident plane wave propagating in the xz plane making an angle θ with the z axis. The incident, reflected and transmitted electric field phasors are given by,

$$\mathbf{E}_{\text{inc}}(\mathbf{r}) = \hat{\mathbf{p}}_0^+ a_p^{(0)} \exp\left[i(k_x^{(0)} x + k_{zp}^{(0)} z)\right], \quad z < 0\,, \tag{3.1}$$

$$\mathbf{E}_{\text{ref}}(\mathbf{r}) = \sum_{\ell=-N_t}^{N_t} \hat{\mathbf{p}}_\ell^- r_p^{(\ell)} \exp\left[i(k_x^{(\ell)} x - k_{zp}^{(\ell)} z)\right], \quad z < 0\,, \tag{3.2}$$

and

$$\begin{aligned}\mathbf{E}_{\text{tr}}(\mathbf{r}) = \sum_{\ell=-N_t}^{N_t} \hat{\mathbf{p}}_\ell^t t_p^{(\ell)} \exp\Big(i\{k_x^{(\ell)} x \\ + k_{zt}^{(\ell)}[z - (L_m + L_g + L_d)]\}\Big), \quad z > L_m + L_g + L_d\,,\end{aligned} \tag{3.3}$$

respectively, where $a_p^{(0)}$ is the amplitude of the incident plane wave, and $r_p^{(\ell)}$ and $t_p^{(\ell)}$ are the unknown amplitudes of Floquet harmonics of order ℓ in the reflected and transmitted fields, respectively, where ℓ is the order of Floquet harmonic with $\ell \in \{0, \pm 1, \pm 2 ...\}$. Here $\ell = 0$ corresponds to the specular component of reflected and transmitted fields, and $\ell \neq 0$ are the non-specular components. The parameter N_t in the summation is taken to be 21 (total terms in the sum is $2N_t + 1 = 43$), after ascertaining the convergence of the results within 0.5% of the results when $N_t = 20$. The other parameters are given by,

$$k_{zp}^{(\ell)} = \sqrt{k_0^2 n_p^2 - (k_x^{(\ell)})^2}\,, \tag{3.4}$$

$$k_{zt}^{(\ell)} = \sqrt{k_0^2 n_t^2 - (k_x^{(\ell)})^2}\,, \tag{3.5}$$

$$\hat{\mathbf{p}}_\ell^{\pm} = \frac{\mp k_{zp}^{(\ell)}\hat{\mathbf{u}}_x + k_x^{(\ell)}\hat{\mathbf{u}}_z}{k_0 n_p}, \tag{3.6}$$

and

$$\hat{\mathbf{p}}_\ell^{t} = \frac{k_{zt}^{(\ell)}\hat{\mathbf{u}}_x + k_x^{(\ell)}\hat{\mathbf{u}}_z}{k_0 n_t}. \tag{3.7}$$

Linear reflectance and transmittance of order ℓ are defined as [91]

$$R_{pp}^{(\ell)} = \left|\frac{r_p^{(\ell)}}{a_P^{(0)}}\right|^2 \frac{\mathrm{Re}[k_{zp}^{(\ell)}]}{k_{zp}^{(0)}} \tag{3.8}$$

and

$$T_{pp}^{(\ell)} = \left|\frac{t_p^{(\ell)}}{a_p^{(0)}}\right|^2 \frac{\mathrm{Re}[k_{zt}^{(\ell)}]}{k_{zp}^{(0)}}, \tag{3.9}$$

respectively. Therefore, the absorptance is defined as

$$A_p = 1 - \sum_{\ell=-\infty}^{\infty} \left(R_{pp}^{(\ell)} + T_{pp}^{(\ell)}\right). \tag{3.10}$$

Let us note that $0 \leq A_p \leq 1$ for energy conservation because the definitions (3.8) and (3.9) are the ratios of the reflected and transmitted power densities (z components of the Poynting vector) of the ℓth Floquet mode, respectively, and the incident power. The component of the wavenumber along x-axis is given as

$$k_x^{(\ell)} = k_0 n_p \sin\theta + \ell(2\pi/L). \tag{3.11}$$

This equation shows that the wavenumber of the Floquet harmonics depends upon both the refractive index n_p of the prism refractive index and the order of the harmonic ℓ. An SPP wave is excited when this wavenumber is the same as the real part of the wavenumber of the possible SPP wave at the chosen interface. Therefore, both the prism and grating period determine the angle θ and ℓ that will excite the SPP waves. We used the RCWA to find reflectance, transmittance and absorptance [29, 30, 5, 34].

3.3 Numerical Results and Discussion

We implemented the RCWA in Matlab to find the absorptances as a function of the incidence angle θ and wavelength λ_0. First we present the results of angular interrogation and then the results of wavelength interrogation are presented. The metallic film thickness $L_m = 20$ nm,

the grating depth $L_g = 40$ nm, the dielectric medium thickness $L_d = 1000$ nm, and the prism $n_p = 1.7$ were all kept fixed. Furthermore, $n_t = n_d \in [1, 1.5]$ was used since most fluids have the refractive index in this range.

3.3.1 Angular Interrogation

For angular interrogation, change in the refractive index of the dielectric medium is sensed by determining the change in the incidence angle of excitation of the SPP wave. All the results for the angular interrogation were computed at a wavelength of $\lambda_0 = 635$ nm. The metal was taken to be gold ($n_m = 0.14089 + 3.6318i$). Figures 3.2(a) and (b) show the absorptance spectrums for $n_t = n_d \in [1, 1.5]$ when the grating period $L = 700$ nm and 800 nm, respectively, and the prism has a refractive index $n_p = 1.7$. Figure 3.2(c) shows the absorptance when the refractive index of the prism is changed to 2.6 and the grating period is $L = 700$ nm, showing the effect of the refractive index. In these spectra, two sets of peaks are identified: $\ell = 0$ peaks when $k_x^{(0)} \sim \mathrm{Re}(q)$ and $\ell = 1$ peaks when $k_x^{(1)} \sim \mathrm{Re}(q)$, where $q = k_0\sqrt{n_m^2 n_d^2/(n_m^2 + n_d^2)}$ is the wavenumber of the possible SPP wave at the dielectric/metal interface. Therefore, $\ell = 0$ peaks are essentially the peaks representing the excitation of SPP waves that are only due to the prism as they are independent of the grating period L and only depend upon n_p. The $\ell = 1$ peaks are due to the combination of the prism and the grating since they depend upon n_p and L. The change in the angular position of both the peaks indicates that both the peaks can be used for optical sensing.

To verify that the absorptance peaks indeed represent the SPP waves, the x-component of the time-averaged Poynting vector $\mathbf{P}(x,z)$ is plotted as a function of x and z in Fig. 3.3 for both the peaks when $n_d = 1.2$ and $L = 700$ nm. In Fig. 3.2(a), the absorptance peaks for $n_d = 1.2$ are present at $\theta = 52.2$ deg ($\ell = 0$ peak) and 11.4 deg ($\ell = 1$ peak). That is why we have used these two angles in the Fig. 3.3 to plot the Poynting vector $\mathbf{P}(x,z)$. The localization of the power density near the metal/dielectric interface indicates that an SPP wave indeed exists for both the peaks. Furthermore, the power is localized to the planar part of the grating in Fig. 3.3(a) for the $\ell = 0$ peak and the power is localized to the metal/dielectric interface more uniformly in Fig. 3.3(b) for the $\ell = 1$ peak. Also, we can see the that the power density is periodic along x axis, which should be the case because the geometry is periodic along this axis.

To analyze the usefulness of both the peaks for optical sensing, we computed the

$$Sensitivity = \frac{\Delta\theta}{\Delta n_d}, \tag{3.12}$$

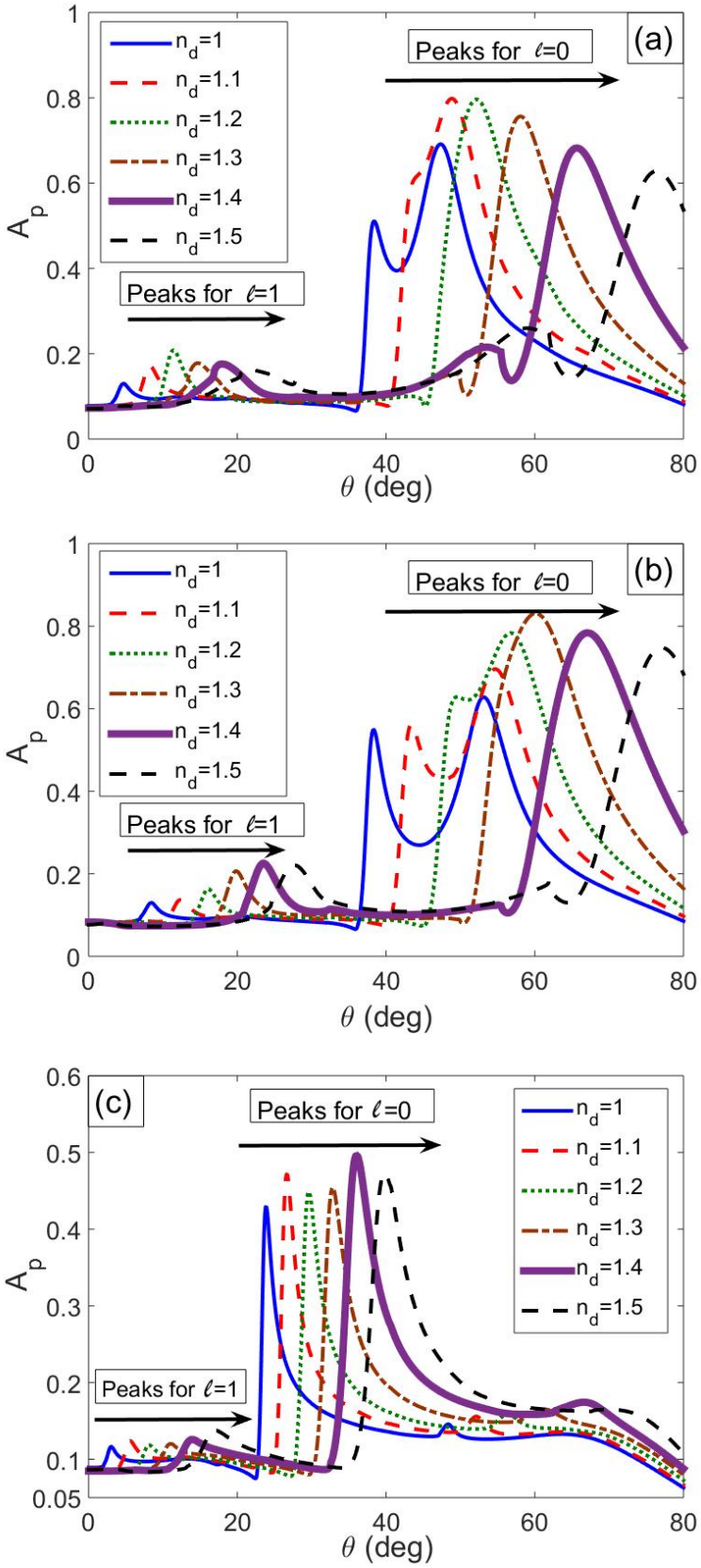

Fig. 3.2 Absorptance A_p as a function of incidence angle θ, $L_m = 20$ nm, $L_g = 40$ nm, $L_d = 1000$ nm, $n_t = n_d$, (a) $L = 700$ nm, $n_p = 1.7$, (b) $L = 800$ nm, $n_p = 1.7$, and (c) $L = 700$ nm, $n_p = 2.6$. The horizontal arrows show the shift of peaks representing the excitation of SPP wave.

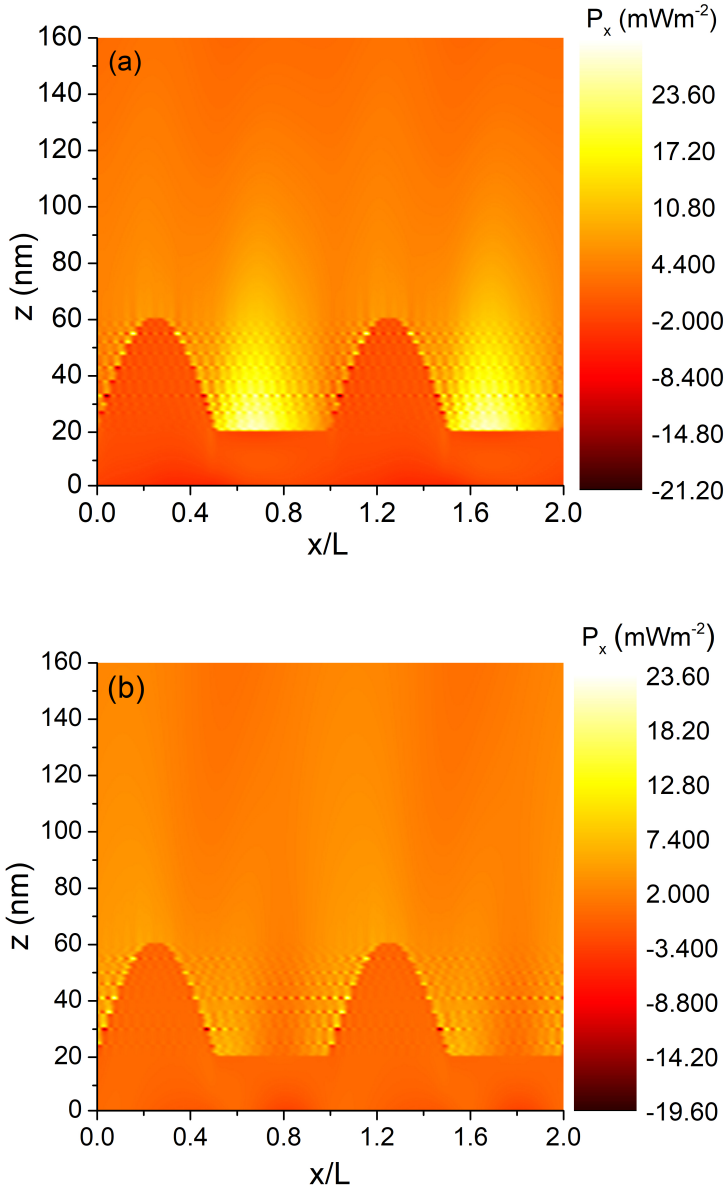

Fig. 3.3 Variation of the x-component of the time averaged Poynting vector $\mathbf{P}(x,z)$ as a function of x and z, when $n_d = n_t = 1.2$, $L = 700$ nm, $L_d = 1000$ nm, $L_g = 40$ nm, $n_p = 1.7$, (a) ($\ell = 0$ peak) $\theta = 52.2$ deg and (b) ($\ell = 1$ peak) $\theta = 11.4$ deg.

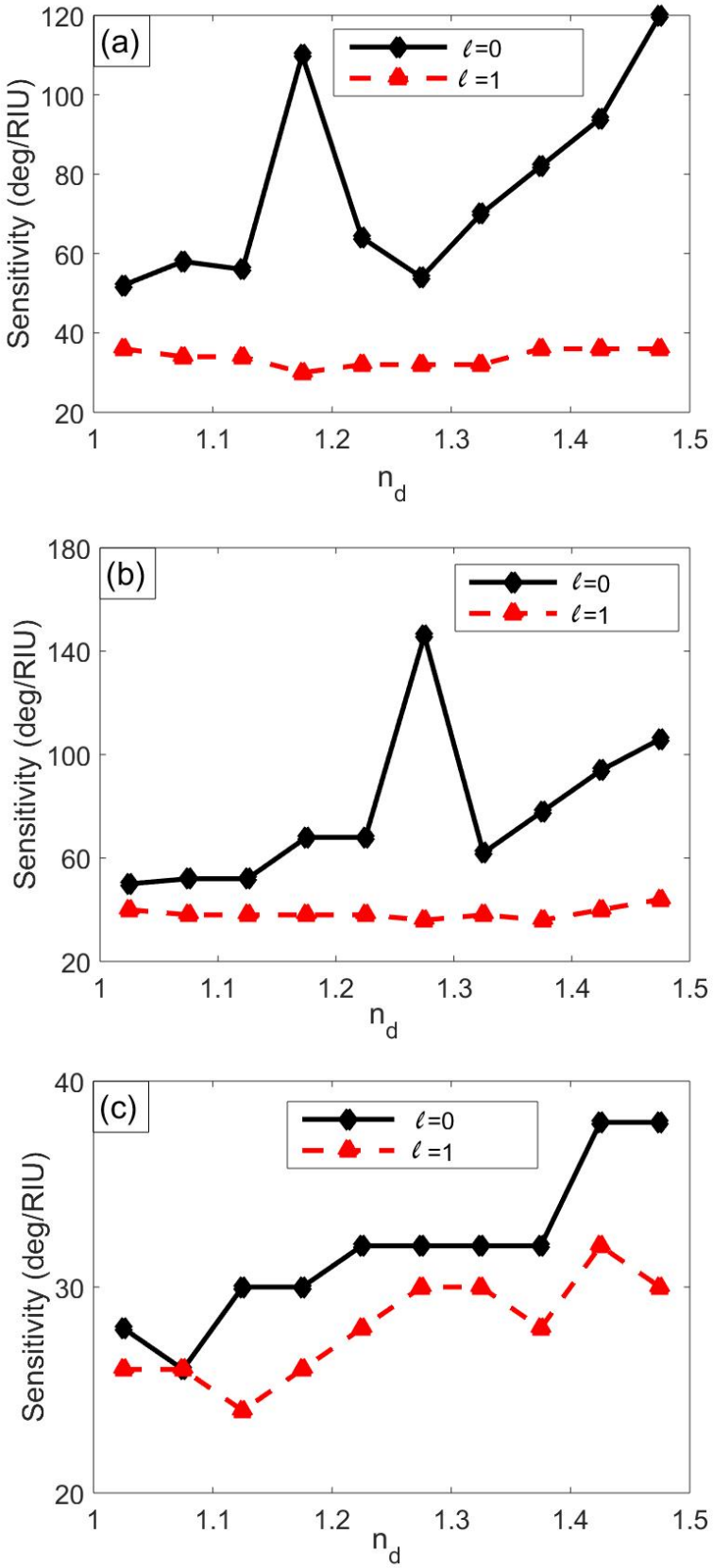

Fig. 3.4 Sensitivity (Eq. 3.12) in degrees per refractive index units (RIU) as a function of the refractive index (n_d) of the dielectric material corresponding to the cases presented in Fig. 3.2 for the angular interrogation scheme.

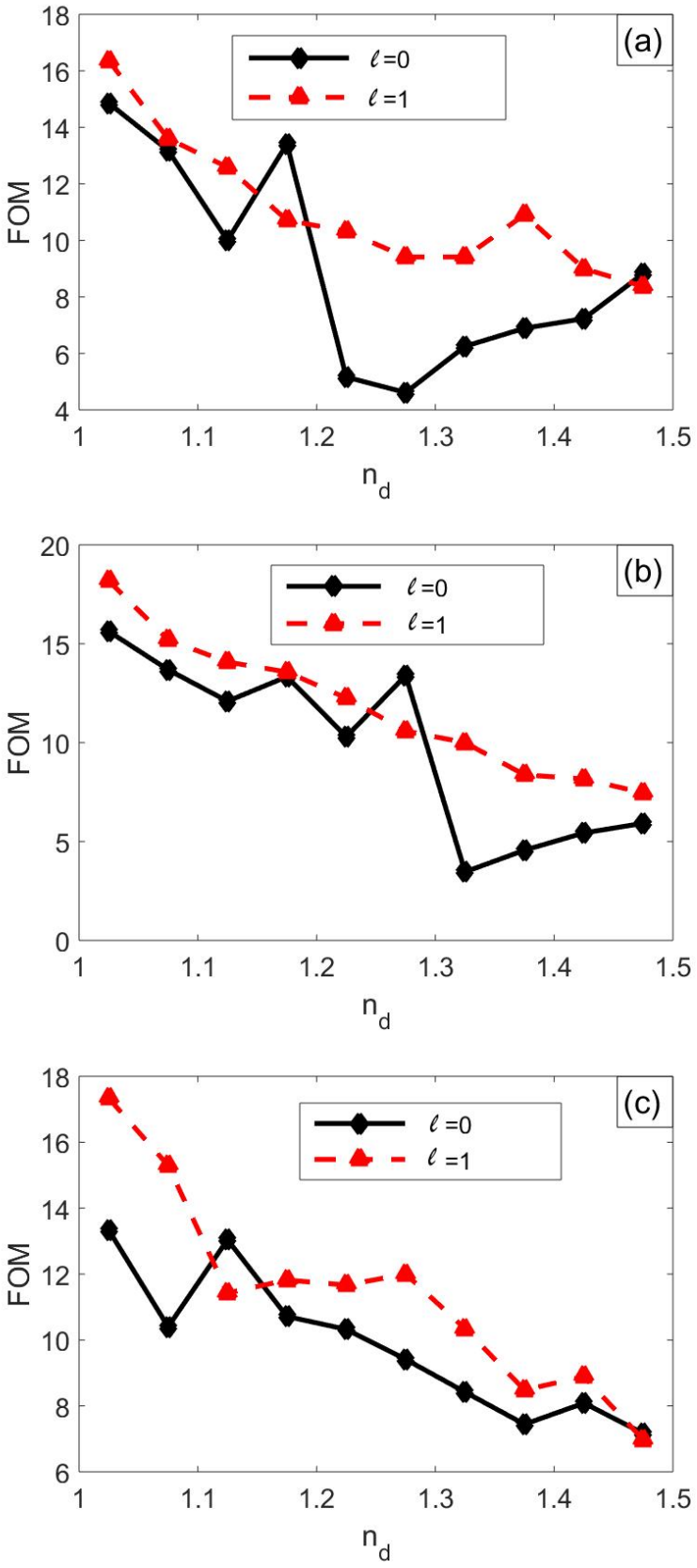

Fig. 3.5 Figure of merit (FOM) as a function of refractive index of the dielectric material (n_d) corresponding to the cases presented in Fig. 3.2.

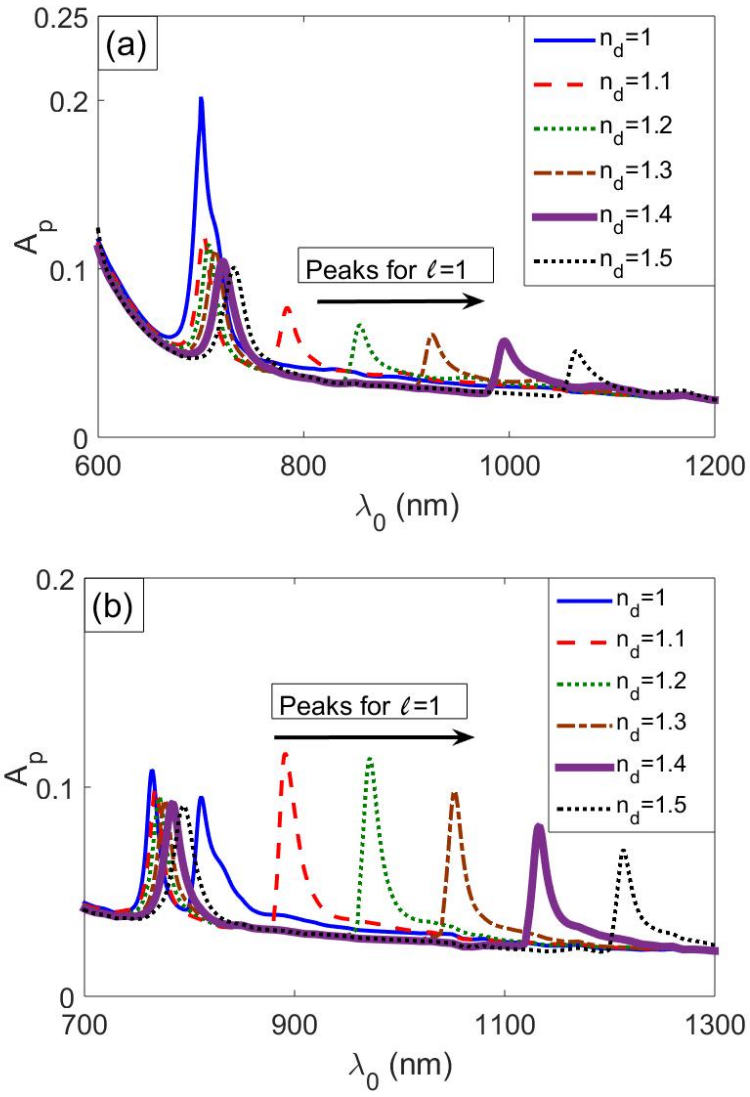

Fig. 3.6 Absorptance A_p as a function of wavelength λ_0, when $\theta = 0$ deg, $n_p = 1.7$, and (a) $L = 700$ nm, and (b) $L = 800$ nm.

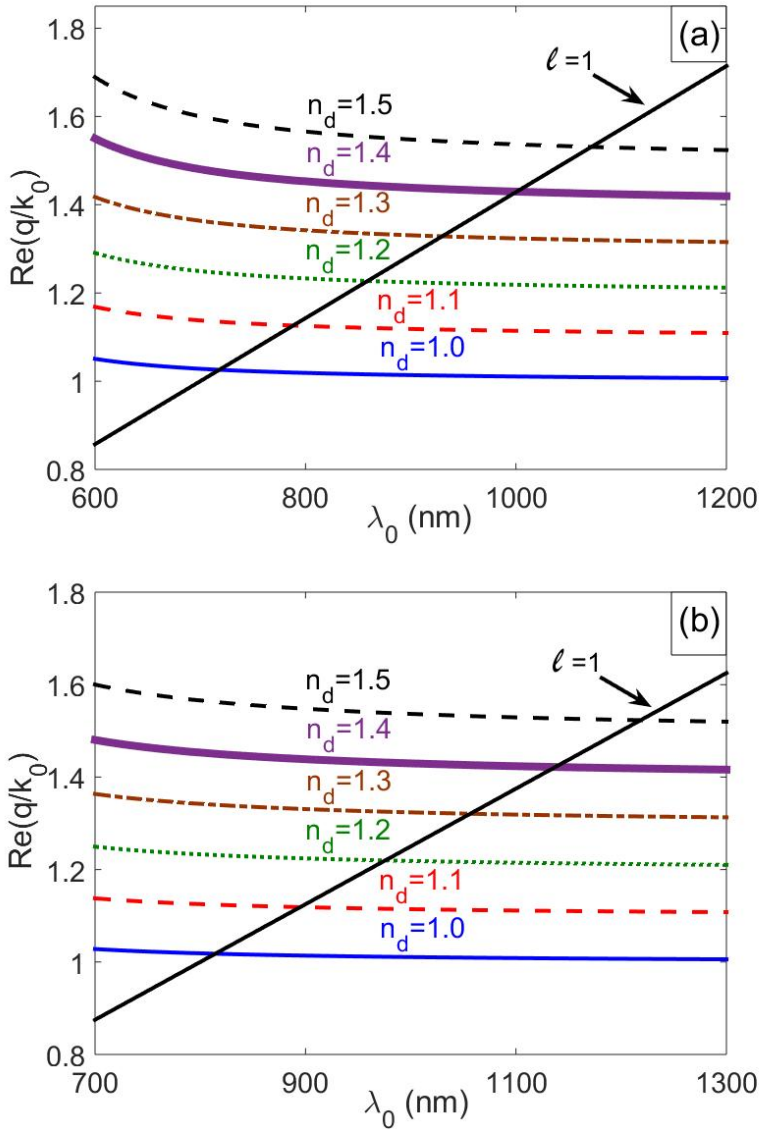

Fig. 3.7 Graphical solution of Eq. (3.14): The right-hand side of the equation as a function of λ_0 is shown by a solid black straight line when $\ell = 1$. The real parts of the solutions of the canonical problem q/k_0 as a function of wavelength for different values of n_d are also plotted. The spectral values of the intersections represent the solutions of the equation. The values of the grating periods are (a) $L = 700$ nm and (b) $L = 800$ nm.

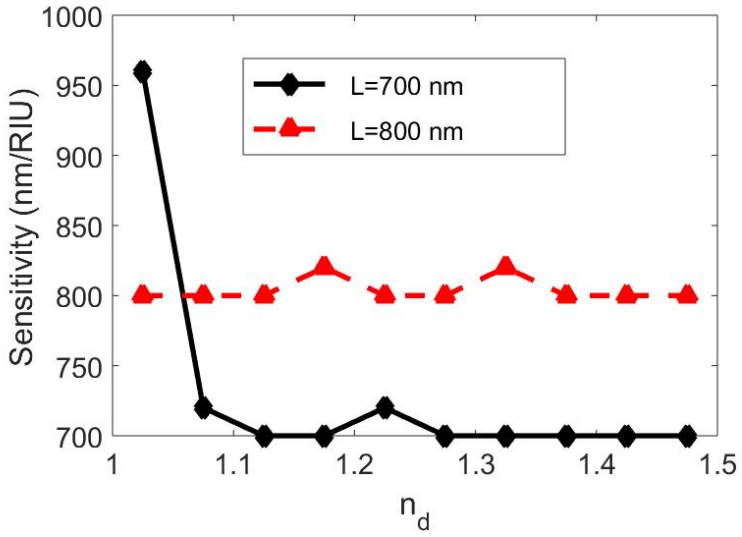

Fig. 3.8 Sensitivity (Eq. 3.15) in nm per refractive index units (RIU) as a function of the refractive index (n_d) of the dielectric material for the wavelength interrogation scheme.

where $\Delta\theta$ is the difference between the two incidence angles for the SPP wave excitation and Δn_d is the difference between the refractive indices of the dielectric material. The sensitivity of the angular positions of both the peaks was computed and is presented in Fig. 3.4 when (a) $L = 700$ nm, $n_p = 1.7$, (b) $L = 800$ nm, $n_p = 1.7$, and (c) $L = 700$ nm, $n_p = 2.6$. A quick scan of the figures shows that the sensitivity of the $\ell = 0$ peak is generally higher than the $\ell = 1$ peaks. Also, the sensitivity of $\ell = 0$ peaks is almost independent of the grating period L (as should be expected since the peak only depends on the refractive index of the prism) but inversely proportional to the refractive index of the prism, though the sensitivity of the $\ell = 1$ peak slightly increases with increase in the period L but is inversely proportional to the refractive index n_p of the prism. Furthermore, the sensitivity plots show that the sensitivity, in general, is dependent upon the refractive index of the fluid.

In actual experiments, however, it is not just the angular shift that is important in measurement of the change in the angular position of the peak for a change in the refractive index of the dielectric material n_d to be sensed. What is important is the change in the angular location with respect to the peak width. Therefore, we computed a Figure of merit (FOM) defined as

$$FOM = \frac{Sensitivity}{\Delta\theta_{FWHM}}, \tag{3.13}$$

where $\Delta\theta_{FWHM}$ is the full width at half maximum of the absorption peak, and is presented in Fig. 3.5. The figure indicates that the FOM is generally higher for the $\ell = 1$ peak which is due to the combination of the prism and the grating and is smaller for the $\ell = 0$ peak which

is solely due to the prism. This is because the $\ell = 1$ peaks are considerably sharper than the $\ell = 0$ peaks.

3.3.2 Wavelength Interrogation

For the wavelength interrogation, all the results were computed for normal incidence ($\theta = 0$ deg) but the absorptances were computed as a function of wavelength λ_0. The refractive index of the fluid-to-be-sensed and the prism were taken to be independent of the wavelength but the refractive index of the metal (gold) was taken to be wavelength dependent. Figures 3.6(a) and (b) shows the absorptance spectra as a function of wavelength λ_0 for $n_t = n_d \in [1, 1.5]$ when the grating period $L = 700$ nm and 800 nm, respectively. These absorptance peaks in the figures labelled as $\ell = 1$ peaks represent the SPP waves. The shift in their spectral position clearly indicates that this configuration can be used for the optical sensing.

To confirm that these absorptance peaks correspond to the excitation of SPP wave, we need to see if they correlate with the solution of the canonical problem of SPP waves guided by the planar gold/fluid interface. Since the refractive index of gold is taken to be wavelength dependent, we need to solve the below nonlinear equation to find the wavelengths where the SPP waves can be excited for a given ℓ and L [5, 31]:

$$\mathrm{Re}\big(\frac{q}{k_0}\big) = n_p \sin\theta + \ell\frac{\lambda_0}{L}\,. \tag{3.14}$$

We have solved this equation graphically, as shown Figs. 3.7(a) and (b) by finding the intersections of the left-hand side of this equation with the right-hand side. The left-hand side is a nonlinear function of the wavelength as the canonical solution q depends on n_d and $n_m(\lambda_0)$. The right-hand side is an equation of a straight line. The graphical solutions showed that the line $\ell = 1$ for $L = 700$ nm intersects the canonical solution curves for different values of n_d at $\lambda_0 = \{715, 788, 858, 930, 1000, 1070\}$ nm. These values of λ_0 are in excellent agreement with the peaks in Fig. 3.6(a) at $\lambda_0 = \{700, 784, 854, 925, 995, 1065\}$ nm. Similarly for $L = 800$ nm, Fig. 3.7(b) shows that the SPP waves should be excited at $\lambda_0 = \{813, 895, 976, 1055, 1137, 1218\}$ nm by $\ell = 1$ Flouquet harmonics. The peaks in Fig. 3.6(b) are present at $\lambda_0 = \{811, 891, 972, 1052, 1133, 1213\}$ nm showing an agreement between the canonical and grating results.

To examine the sensitivity of the proposed scheme in the wavelength interrogation scheme, the sensitivity is computed as

$$Sensitivity = \frac{\Delta\lambda_0}{\Delta n_d}\,, \tag{3.15}$$

where $\Delta\lambda_0$ is the spectral shift between the two peaks for the SPP wave excitation when n_d changes by Δn_d. The sensitivity is presented in Fig. 3.8 when (a) $L = 700$ nm and (b) $L = 800$ nm. The figures shows that the sensitivity for $L = 800$ nm is higher than the $L = 700$ nm. Let us note that the sensitivity is not affected by n_p for the normal incidence in the wavelength interrogation because the term $n_p \sin\theta = 0$ for this case.

3.4 Conclusions

We theoretically analyzed the excitation of SPP waves using a combination of a prism and a surface-relief grating. Both the angular and the wavelength interrogation schemes in the new geometry are proposed in this chapter. The combination made possible by an inverted grating with a prism attached to the planar side of the grating. It was seen that two types of absorption peaks are available to implement a plasmonic optical sensor. This can be used to sense the same analyte at two different angles of incidence to increase confidence in measurement. Of the two absorption peaks, it was seen that the sensitivity of the angular location of the peak to the change in the refractive index of the fluid is stronger for the peak excited by the specular component of the field but the shift in the angular location with respect to the width of the peak is somewhat higher for the non-specularly excited SPP waves. The promise of the sensing of the new geometry is also shown in the wavelength interrogation scheme. The proposed configuration can be used to build more sensitive and more reliable plasmonic sensor. The sensitivity in the geometry proposed in this work can be tuned by changing the prism refractive index and the grating period.

Chapter 4

SPP Waves along the Direction of Periodicity of Photonic Crystal

In this chapter, excitation of surface plasmon-polariton waves is investigated at an interface of a metal and a one-dimensional photonic crystal (1DPC) along the direction of periodicity of the photonic crystal in a prism-coupled configuration. The RCWA is used to formulate the problem and the absorptance spectra are obtained as a function of the incidence angle, the period, and the thickness of the photonic crystal. The correlation of the absorptance bands with the underlying canonical problem and the spatial power profiles confirmed the excitation of SPP waves. The excitation of SPP waves at the interface of the 1DPC along the direction of the periodicity opens up new avenues for applications. This interface was accessed by illuminating the metal/1DPC interface from metallic side. The plan of this chapter is as follows: Introduction to the problem is given in Section 4.1. The description and brief formulation of the problem are given in Section 4.2. Numerical results are presented and discussed in Section 4.3, and concluding remarks are presented in Section 4.4.

4.1 Introduction

Excitation of SPP waves at an interface of a homogeneous material and a one-dimensional photonic crystal (1DPC) was first studied in 1978 [92]. These SPP waves are localized to the interface which is perpendicular to the direction of periodicity of the 1DPC and have several names in the literature like Tamm plasmon-polariton (TPP), surface Bragg waves, or just SPP waves [93]. Surface waves guided by an interface of a metal and 1DPC has many

This chapter is based on "Kamran and Faryad, Excitation of surface plasmon polariton waves along the direction of periodicity of a one-dimensional photonic crystal, Physical Review A, **99**, 053811 (2019)".

applications, especially optical sensors of fluids and biochemicals [94, 95], light-couplers [96], directional emitter [97], and wave guides [98].

In all of this previous work, only excitation of surface wave guided by an interface of a homogeneous medium and the photonic crystal was exploited in the direction perpendicular to the periodicity of the 1DPC [98–100]. The excitation of surface waves at metal/1DPC interface along the direction of periodicity was neglected. Recently, a rigorous formulation of SPP waves' propagation along the direction of the periodicity of the 1DPC was presented in Ref. [101], where they obtained a dispersion equation and solved the canonical-boundary value problem for the excitation of surface waves at metal/1DPC interface along the direction of periodicity.

However, the canonical boundary-value problem is not practically realizable, because both the partnering materials are supposed to be semi-infinite. And, it is not always possible to assume that the solutions predicted by the canonical problem can be realized in a prism-coupled configuration [102]. Therefore, we set out to investigate if the excitation of the SPP waves at an interface of a metal and 1DPC along the direction of the periodicity of the photonic crystal in the prism-coupled configuration is possible as predicted by the canonical problem. For this purpose, the prism-coupled problem is formulated and solved using the RCWA [27, 28].

4.2 Problem Description

Let us consider the geometry of the problem schematically shown in Fig. 4.1. Let us assume that SPP wave is guided by the interface of the metal and the 1DPC along the x axis. Let the half-space $z<0$ be occupied by homogeneous medium (prism) with permittivity ε_p. The region $0<z<L_m$ is occupied by a metal with permittivity ε_m and thickness L_m. The region between $z>L_m$ and $z<L_m+L_{pc}$ is a photonic crystal of period Λ and thickness L_{pc}. The relative permittivity of the photonic crystal is

$$\varepsilon_r(x)=\varepsilon_r(x\pm\Lambda)\,,\quad L_m<z<L_m+L_{pc}\,. \tag{4.1}$$

The permittivity of the photonic crystal can be expanded as a Fourier series with respect to x

$$\varepsilon_r(x)=\sum_{\ell\in\mathbb{Z}}\varepsilon_r^{(\ell)}\exp(i\ell\kappa_x x)\,,\quad \mathbb{Z}\in\{0,\pm1,\pm2,...\}\,, \tag{4.2}$$

where $\kappa_x=2\pi/\Lambda$, and

$$\varepsilon_r^{(0)}=\frac{1}{\Lambda}\int_0^{\Lambda}\varepsilon_r(x)dx\,, \tag{4.3}$$

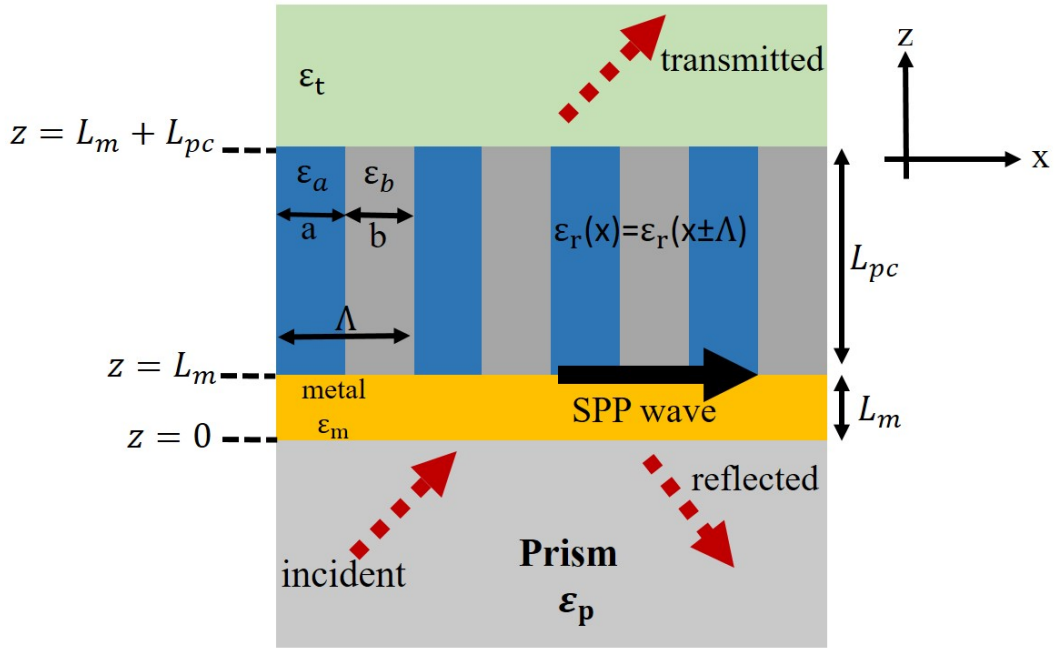

Fig. 4.1 Schematic representation of the geometry of the boundary-value problem. A p-polarized plane wave is incident upon metal/1DPC bilayer from inside a prism of relative permittiity ε_p.

and

$$\varepsilon_r^{(\ell)} = \frac{1}{\Lambda}\int_0^{\Lambda} \varepsilon_r(x)\exp(-i\ell\kappa_x x)dx\,, \quad \ell \neq 0. \tag{4.4}$$

The region $z > L_m + L_{pc}$ is a semi-infinite medium with permittivity ε_t.

To predict the excitation of the SPP waves we need to compute the plane wave absorption by the metal and the 1DPC and identify the absorption peaks that are independent of the thickness of the photonic crystal. Since the 1DPC is taken to be made up of isotropic materials, only a p-polarized incident plane wave can excite an SPP wave. For this purpose, let us consider a p-polarized plane wave propagating in the xz plane and be incident on the metal from prism side making an angle θ with the z axis. The incident, reflected and transmitted electric field phasors are given by

$$\mathbf{E}_{\text{inc}}(\mathbf{r}) = \hat{\mathbf{p}}_0^{+} a_p^{(0)} \exp\left\{ i\left[k_x^{(0)}x + k_{zp}^{(0)}z\right]\right\}, \quad z < 0\,, \tag{4.5}$$

$$\mathbf{E}_{\text{ref}}(\mathbf{r}) = \sum_{\ell=-N_t}^{N_t} \hat{\mathbf{p}}_\ell^{-} r_p^{(\ell)} \exp\left[i(k_x^{(\ell)}x - k_{zp}^{(\ell)}z)\right], \quad z < 0\,, \tag{4.6}$$

and

$$\mathbf{E}_{\mathrm{tr}}(\mathbf{r}) = \sum_{\ell=-N_t}^{N_t} \hat{\mathbf{p}}_\ell^t t_p^{(\ell)} \exp\Big(i\{k_x^{(\ell)} x + k_{zt}^{(\ell)}[z-(L_m+L_{pc})]\}\Big), \quad z > L_m + L_{pc}\,, \tag{4.7}$$

respectively, in terms of the Floquet harmonics. Where $a_p^{(0)}$ is the known amplitude of the incident electric field, $r_p^{(\ell)}$ and $t_p^{(\ell)}$ are the unknown field amplitude of the reflected and transmitted electric fields of the ℓth Floquet harmonics, where ℓ is the order of the Floquet harmonics with $\ell \in \{0, \pm 1, \pm 2...\}$. Here $\ell = 0$ represents the specular component of the fields, and $\ell \neq 0$ are the non-specular components of the fields. Other parameters are given by

$$k_{zp}^{(\ell)} = \sqrt{k_0^2 \varepsilon_p - (k_x^{(\ell)})^2}\,, \tag{4.8}$$

$$k_{zt}^{(\ell)} = \sqrt{k_0^2 \varepsilon_t - (k_x^{(\ell)})^2}\,, \tag{4.9}$$

$$\hat{\mathbf{p}}_\ell^{\pm} = \frac{\mp k_{zp}^{(\ell)} \hat{\mathbf{u}}_x + k_x^{(\ell)} \hat{\mathbf{u}}_z}{k_0 \sqrt{\varepsilon}_p}\,, \tag{4.10}$$

and

$$\hat{\mathbf{p}}_\ell^{t} = \frac{k_{zt}^{(\ell)} \hat{\mathbf{u}}_x + k_x^{(\ell)} \hat{\mathbf{u}}_z}{k_0 \sqrt{\varepsilon}_t}\,. \tag{4.11}$$

The x component of the wave number is given by

$$k_x^{(\ell)} = k_0 \sqrt{\varepsilon}_p \sin\theta + \ell(2\pi/\Lambda)\,. \tag{4.12}$$

To implement the RCWA, the field phasors are expanded in terms of Floquet harmonics in region $0 \leq z \leq L_m + L_{pc}$ as

$$\mathbf{E}(\mathbf{r}) = \sum_{\ell=-N_t}^{N_t} \Big[E_x^{(\ell)}(z)\hat{\mathbf{u}}_x + E_z^{(\ell)}(z)\hat{\mathbf{u}}_z\Big] \times \exp(ik_x^{(\ell)} x)\,, \quad z \in [0, L_m + L_{pc}]\,, \tag{4.13}$$

$$\mathbf{H}(\mathbf{r}) = \sum_{\ell=-N_t}^{N_t} H_y^{(\ell)}(z)\hat{\mathbf{u}}_y \exp(ik_x^{(\ell)} x)]\,, \quad z \in [0, L_m + L_{pc}]\,, \tag{4.14}$$

where N_t is an integer. Substituting Eqs. (4.13), and (4.14) in Maxwell curl postulates, we get two ordinary differential equations and one algebraic equation. The algebraic equation

can be arranged as

$$\left[\mathbf{E}_z(z)\right] = -\frac{\eta_0}{k_0}\left[\underline{\underline{\varepsilon}}(z)\right]^{-1}\cdot\left[\underline{\underline{K}}_x\right]\cdot\left[\mathbf{H}_y(z)\right], \tag{4.15}$$

where

$$\left[\underline{\underline{K}}_x\right] = \mathrm{diag}\left[k_x^{(\ell)}\right] \tag{4.16}$$

is a $(2N_t+1)\times(2N_t+1)$ diagonal matrix,

$$\left[\underline{\underline{\varepsilon}}(z)\right] = \left[\varepsilon^{(\ell-m)}(z)\right] \tag{4.17}$$

is a $(2N_t+1)\times(2N_t+1)$ Toeplitz matrix, and $[\mathbf{E}_x(z)]$ etc. are $(2N_t+1)\times 1$ column matrices. The two differential equations can be rearranged as a matrix ordinary differential equation

$$\frac{d}{dz}[\mathbf{f}^{(p)}(z)] = i\left[\underline{\underline{P}}^{(p)}(z)\right]\cdot[\mathbf{f}^{(p)}(z)], \qquad z\in(0, L_m+L_{pc}), \tag{4.18}$$

where the $2(2N_t+1)\times 1$ column vector $[\mathbf{f}^{(p)}(z)]$ is given as

$$[\mathbf{f}^{(p)}(z)] = \left[[\mathbf{E}_x(z)]^T, \eta_0[\mathbf{H}_y(z)]^T\right]^T, \tag{4.19}$$

and

$$\left[\underline{\underline{P}}^{(p)}(z)\right] = \begin{bmatrix} [\underline{\underline{0}}] & \left[\underline{\underline{P}}_{14}(z)\right] \\ \left[\underline{\underline{P}}_{41}(z)\right] & [\underline{\underline{0}}] \end{bmatrix}, \tag{4.20}$$

where $[\underline{\underline{0}}]$ and $[\underline{\underline{I}}]$ are the $(2N_t+1)\times(2N_t+1)$ null and identity matrixes, respectively, and

$$[\underline{\underline{P}}_{14}(z)] = k_0[\underline{\underline{I}}] - \frac{1}{k_0}[\underline{\underline{K}}_x]\cdot[\underline{\underline{\varepsilon}}(z)]^{-1}\cdot[\underline{\underline{K}}_x], \tag{4.21}$$

$$[\underline{\underline{P}}_{41}(z)] = k_0[\underline{\underline{\varepsilon}}(z)]. \tag{4.22}$$

The matrix $[\underline{\underline{P}}^{(p)}(z)]$ in Eq. (4.18) is z dependent. In order to solve this differential equation, the region between $0\leqslant z\leqslant L_m+L_{pc}$ is divided into small parallel slices, so that in each slice the matrix $[\underline{\underline{P}}^{(p)}(z)]$ remains constant. The region $0\leq z\leq L_m$ is divided into N_m slices, and the region $L_m\leq z\leq L_m+L_{pc}$ is divided into N_{pc} slices. A stable algorithm provided in Refs. [29, 9, 5] is then used to compute the reflection and transmission amplitudes. The continuity of the fields in $[\mathbf{f}^{(p)}(z)]$ is implemented at the interfaces at $z=0$, $z=L_m$, and $z=L_m+L_{pc}$.

Linear reflectance and transmittance are defined as

$$R_{pp}^{(\ell)} = \left|\frac{r_p^{(\ell)}}{a_p^{(0)}}\right|^2 \frac{\mathrm{Re}[k_{zp}^{(\ell)}]}{k_{zp}^{(0)}}, \tag{4.23}$$

and

$$T_{pp}^{(\ell)} = \left| \frac{t_p^{(\ell)}}{a_p^{(0)}} \right|^2 \frac{\mathrm{Re}[k_{zt}^{(\ell)}]}{k_{zp}^{(0)}}, \tag{4.24}$$

respectively, so that the absorptance is

$$A_p = 1 - \sum_{\ell=-N_t}^{N_t} \left(R_{pp}^{(\ell)} + T_{pp}^{(\ell)} \right). \tag{4.25}$$

The reflection and transmission amplitudes are found using the rigorous coupled-wave analysis (RCWA) using a stable algorithm [5, 29, 30, 34].

4.3 Numerical Results and Discussion

For representative numerical results, the 1DPC is taken to be the same as in Ref. [101] for comparison of the results in this problem with those of the underlying canonical problem solved in Ref. [101]. The 1DPC is made up of alternating layers of two dielectric mediums with thicknesses a and b, and relative permittivities ε_a and ε_b, respectively. Both the layers are of equal thicknesses so that $a = b = 0.5\Lambda$ and the relative permittivity is

$$\varepsilon_r(x) = \begin{cases} \varepsilon_a, & 0 < x < 0.5\Lambda, \\ \varepsilon_b, & 0.5\Lambda < x < \Lambda. \end{cases} \tag{4.26}$$

The Fourier coefficients for this permittivity profile are given as

$$\begin{aligned} \varepsilon_r^{(0)} &= \frac{\varepsilon_a + \varepsilon_b}{2}, \\ \varepsilon_r^{(\ell)} &= \tfrac{i(\varepsilon_b - \varepsilon_a)}{\ell\pi}, \qquad \forall\, \ell = odd, \\ \varepsilon_r^{(\ell)} &= 0, \qquad \forall\, \ell = even. \end{aligned} \tag{4.27}$$

For the numerical results in this section, free-space wavelength is fixed at $\lambda_0 = 633$ nm. The metal is chosen to be gold with the relative permittivity $\varepsilon_m = -11.8 + 1.3i$ and thickness $L_m = 10$ nm. The parameter N_t in the summations is set to be 15 after ascertaining the convergence of the results within 0.5% of the results when $N_t = 14$. Also, $N_m = 1$ and $N_{pc} = 1$ were set for the computation of the absorptance since both the metal and the 1DPC are homogeneous along the z axis. The relative permittivities of the alternating layer in the 1DPC are taken to be $\varepsilon_a = (n_a)^2 + 10^{-6}i$ and $\varepsilon_b = (n_b)^2 + 10^{-6}i$, where $n_a = 1.5$ and $n_b = 2$. The reason behind choosing these values of n_a and n_b is that the most of the dielectric materials have their refractive indexes around it in the visible range. For instance, many

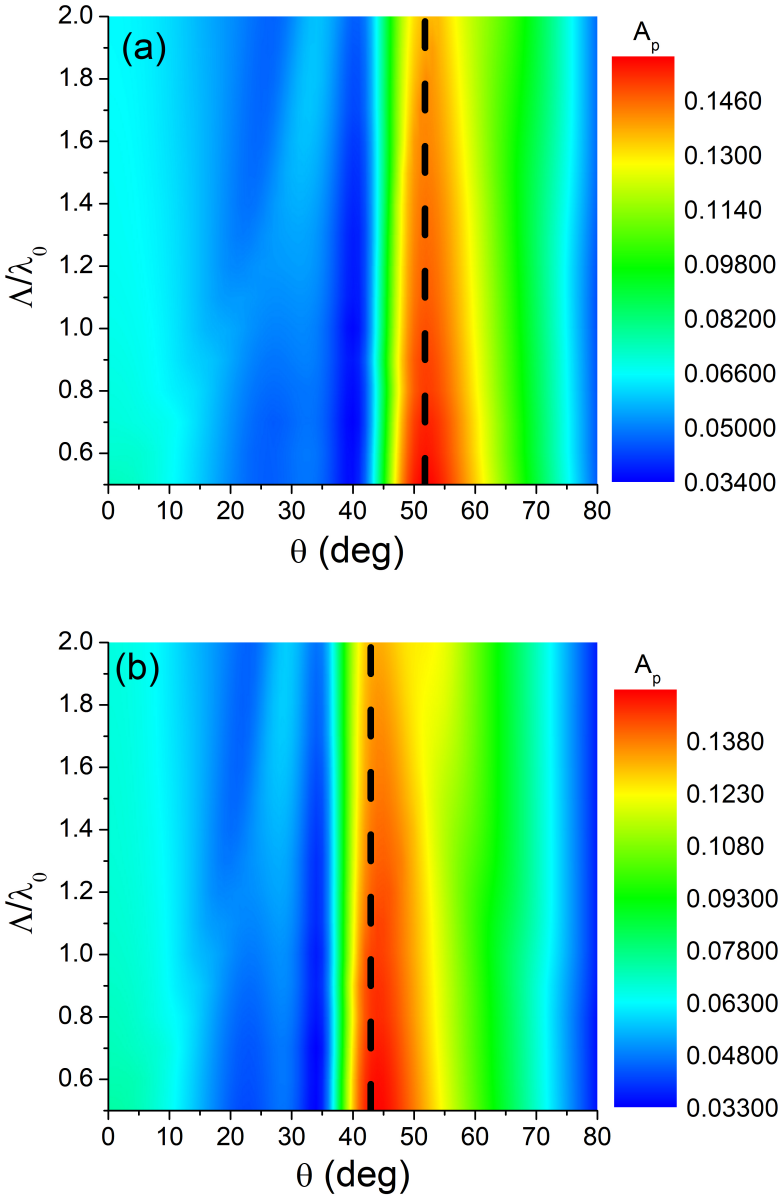

Fig. 4.2 Absorptance A_p as a function of incidence angle θ and the period Λ of the 1DPC, when $L_m = 10$ nm, $L_{pc} = 250$ nm, $n_t = n_p$, and (a) $n_p = 2.6$ and (b) $n_p = 3.0$. The black dashed line represents the angle of incidence for the excitation of surface waves in the underlying canonical boundary-value problem predicted using Eq. (4.28).

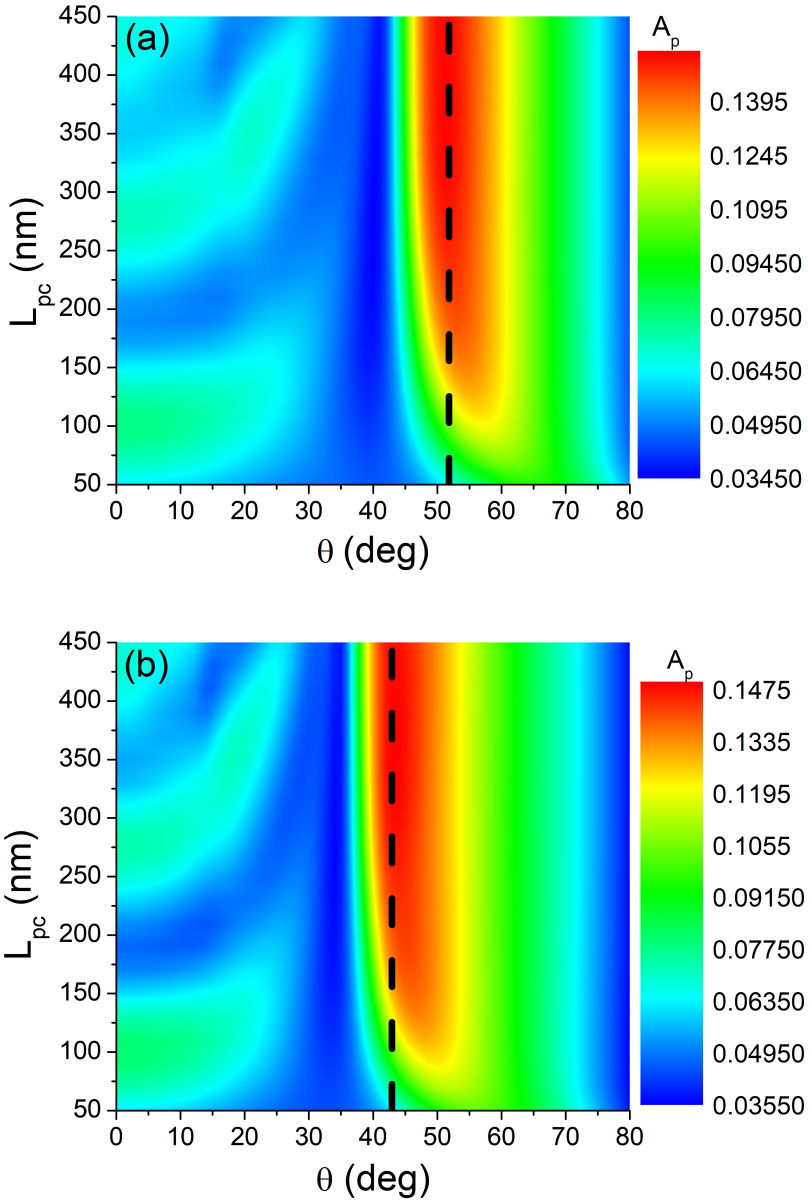

Fig. 4.3 Absorptance A_p as a function of incidence angle θ and the thickness L_{pc} of the 1DPC when $L_m = 10$ nm, $\Lambda = 1.0\lambda_0$ nm, $n_t = n_p$, and (a) $n_p = 2.6$ and (b) $n_p = 3.0$. The black dashed line represents the angle of incidence for the excitation of surface waves in the underlying canonical boundary-value problem predicted using Eq. (4.28).

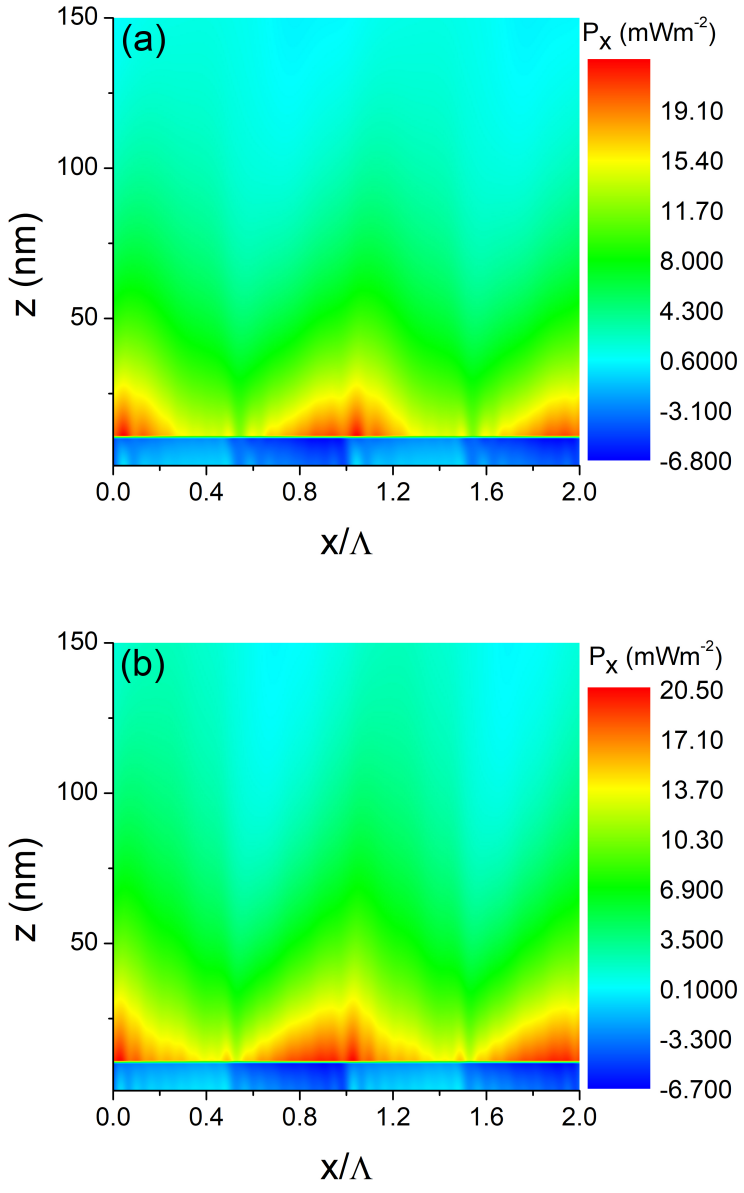

Fig. 4.4 Variation of the x component of the time-averaged Poynting vector P_x as a function of x and z, when $L_m = 10$ nm, $L_{pc} = 250$ nm, $n_p = 3.0$, $n_t = n_p$, $\theta = 44$ deg and (a) $\Lambda = 1.0\lambda_0$ and (b) $\Lambda = 1.5\lambda_0$.

silica-based glasses have their refractive index as 1.5 and the refractive index of ZnO is 2 at a wavelength of 633 nm. The small imaginary part 10^{-6} is added for comparison with the canonical problem where it was required for the computational purpose. The small imaginary part also models the real materials more accurately as all materials are lossy even though the losses are small in dielectric materials. The refractive index of the transmission medium $n_t = \sqrt{\varepsilon_t}$ is taken to be the same as that of the prism.

To delineate the excitation of SPP waves, the absorptance spectrum A_p as a function of the incidence angle θ and the period Λ of the 1DPC is presented in Fig. 4.2(a) for a prism with refractive index $n_p = 2.6$ and the thickness of the 1DPC $L_{pc} = 250$ nm. A quick scan of the figure shows that an absorptance band around $\theta = 52$ deg is present which indicates the excitation of SPP wave. To confirm that this absorptance band correlates with the canonical problem, we can use Eq. 4.12 to find the θ predicted by the canonical problem as

$$\theta = \sin^{-1}\left[\frac{\mathrm{Re}(q) - \ell(2\pi/\Lambda)}{k_0 n_p}\right], \tag{4.28}$$

where $q \sim 2.04k_0$ is the wavenumber predicted by the canonical problem [101]. For the parameters used in Fig. 4.2(a), Eq. (4.28) gives $\theta \sim 51.8$ deg when $\ell = 0$, which is in excellent agreement with the position of the spectral band found as $\theta = 52$ deg. Therefore, it can be concluded that the SPP wave is being excited as a Floquet harmonic of order 0.

To see the effect of the refractive index of the prism, the absorptance were computed for a prism with $n_p = 3.0$ (all other parameters are the same as Fig. 4.2(a)) and is presented in Fig. 4.2(b). Now, the absorptance band shifts to $\theta \sim 44$ deg. The canonical problem predicts the excitation angle of $\theta \sim 42.9$ deg that is still an excellent agreement with the angular location of our absorptance band.

To understand the effect of the thickness of the photonic crystal, the absorptance is presented in Fig. 4.3 as a function of the incidence angle θ and the thickness L_{pc} of the 1DPC for two values of the refractive index of the prism when $\Lambda = 1.0\lambda_0$. The slight change in the incidence angle when the thickness of the photonic crystal increases is because of the fact that the SPP wave is localized to the interface on the photonic crystal side and is extended to about 100 nm as the location of the absorption band stops changing after the thickness is increased beyond 100 nm.

To check the spatial extent of the SPP waves on both sides of the interface, the time-averaged Poynting vector is computed at the incidence angle where the surface wave is excited. For this purpose, the electric and magnetic field phasors are computed by dividing the photonic crystal and the metallic layer into 1-nm thick slices parallel to the metal/1DPC interface. Therefore, for the field and Poynting vector computation, the values of $N_m = L_m/1$

nm and $N_{pc} = L_{pc}/1$ nm were taken so as to get 1 nm resolution on the z axis. Furthermore, $a_p = 1$ Vm^{-1} was set. Across each slice, the field vector is computed by the solution of Eq. (4.18) as

$$[\mathbf{f}^{(p)}(z_j)] = \exp\left[i[\underline{\underline{P}}^{(p)}](z_j - z_{j-1})\right] \cdot [\mathbf{f}^{(p)}(z_{j-1})], \quad j \in \{1, N_m + N_{pc}\}. \tag{4.29}$$

After using the components of the field phasors in Eqs. (4.13) and (4.14), the x component of the time-averaged Poynting vector is given by

$$\mathbf{P}_x(x,z) = \frac{1}{2}\mathrm{Re}[\mathbf{E}(x,z) \times \mathbf{H}^*(x,z)]. \tag{4.30}$$

and is presented in Figs. 4.4(a) and (b) when $\Lambda = 1.0\lambda_0$ and $1.5\lambda_0$, respectively, and $\theta = 44$ deg, $L_{pc} = 250$ nm, and $n_p = 3.0$. We can observe that the power density is localized to the metal/1DPC interface which is an indication of the excitation of surface waves. Furthermore, on the side of the photonic crystal, the power is localized to about 100 nm from the interface. This is in line with the conclusion drawn from Fig. 4.3.

4.4 Conclusions

In this chapter, the excitation of surface plasmon-polariton (SPP) waves guided by the interface of a metal and a one-dimensional photonic crystal (1DPC) was shown along the interface which contains the direction of periodicity of the photonic crystal. A prism-coupled configuration was used to excite the SPP waves using metallic films and the 1DPC of the finite widths. Those absorptance bands were identified for plane wave incidence that remain unchanged by a change in the thickness of the 1DPC. The excitation angle in the prism-coupled configuration is in full agreement with the dispersion relation developed in the canonical boundary-value problems [101].

In contrast to the SPP waves guided by an interface of a metal and a 1DPC which is perpendicular to the direction of periodicity of the photonic crystal, this work established the excitation of the SPP waves on the long-neglected interface along the direction of the periodicity. It is hoped that it will open up new avenues of the applications in sensing and imaging. Let us also note that multiple SPP waves of different wavenumbers were excited when the direction of periodicity of the photonic crystal was perpendicular to the interface [34, 103, 104] but no such multiplicity exists in the present case.

Chapter 5

Anti-Reflection Coatings of Zero-Index Metamaterial

In this chapter, anti-reflection coatings of zero index metamaterials (ZIMs) are proposed for maximum absorption of light in solar cells. A thin layer of a ZIM is shown to help trap light inside a solar cell. The outer surface of a ZIM layer is planar, and the inner surface has periodic corrugations in order for the incident light to pass through but block the re-transmission of the light back into free space. Using rigorous calculations for light absorption efficiency integrated over the AM1.5 solar spectrum, the basic design of the anti-reflection coating using a ZIM is studied by comparing the results with a common anti-reflection coating and a ZIM layer planar on both sides.

The plan of this chapter is as follows: Introduction to the problem is given in Section 5.1. Since a ZIM has both permittivity and permeability near zero, we present the specialized formulation of the RCWA in Section 5.2 for isotropic dielectric and magnetic materials. The numerical results are presented and discussed in Section 5.3. The conclusions are presented in Section 5.4.

5.1 Introduction

The reflection of light from solar cells is one of the important factor in reducing the efficiency of the cell to convert the sun light to electric power. For this reason, anti-reflection coatings are used to minimize the reflections. The simplest anti-reflection coating was first observed by Lord Rayleigh in 19th century, when he observed that a tarnishing on a glass increased the transmittance in it instead of reflectance. Etching of a surface can also decrease the

This chapter is based on "Kamran and Faryad, Anti-reflection coatings of zero-index metamaterial for solar cells, AIP Advances **10**, 025010 (2020)".

reflectance from a surface as observed by Fraunhofer in 1817 [105]. The most commonly used anti-reflection coating is a quarter-wave layer matching the impedance of the free-space to that of the substrate [106]. An optimized version of this anti-reflection coating is designed for high efficiency silicon solar cell [107]. Anti-reflection coatings using metamaterials [108] and artificially designed surface-relief grating [109, 110] have also been proposed among others [111, 112]. These techniques have been developed for both the crystalline silicon and thin-film solar cells [113–115].

In addition to the anti-reflection coatings, other light trapping techniques are also being used. For example, the localized surface plasmons using metallic nanoparticles and propagating surface plasmon-polariton waves using surface-relief gratings [8, 116]. Furthermore, the texturing of the surface of solar cell is a very well known and efficient technique for light trapping [117, 118]. Recently, photonic crystal have also been proposed for an enhanced light trapping in thin film solar cells [119]. Nano-structuring can also be used to enhance light trapping with the help of silicon nanowire [120].

Metamaterials are the composite materials, whose properties are engineered from their constituent materials. Zero-index metamaterial (ZIM) are the metamaterials with their permittivity and/or permeability near zero [59, 60]. Hence their refractive index is near zero. When the refractive index is near zero, the phase velocity is very large inside the material. Consequently, the wavelength inside the material is also very large resulting in the phase being uniform throughout the medium [121]. Thus, an electromagnetic wave can only penetrate inside the ZIM if the shape of the wave fronts of the incident electromagnetic wave are of the same shape as of the interface of the ZIM. Therefore, if we design a layer of ZIM medium with planar surface on the side of the incident solar light and corrugations on the side of active solar material, the light will couple into the solar cell but will not be able to exit. This must help increase the light absorption inside the solar cell. This chapter is dedicated to test this hypothesis theoretically using rigorous calculations. The basic design is shown schematically in Fig. 5.1. We used the RCWA to compute the reflectance, transmittance, and absorptance of the solar cell with periodically corrugated ZIM layer [5, 23, 24, 27].

5.2 Problem Description

Let us consider the schematic of the problem shown in Fig. 5.1. The half-space $z < 0$ is the incidence medium with the relative permittivity ε_a and relative permeability μ_a. The region between $z > 0$ and $z < L_{AR}$ is occupied by a material that serves as an anti-reflection coating, with relative permittivity ε_{AR} and relative permeability μ_{AR}, and thickness L_{AR}. The region between $z > L_{AR}$ and $z < L_{AR} + L_z$ is occupied by the one-dimensional surface-releif grating

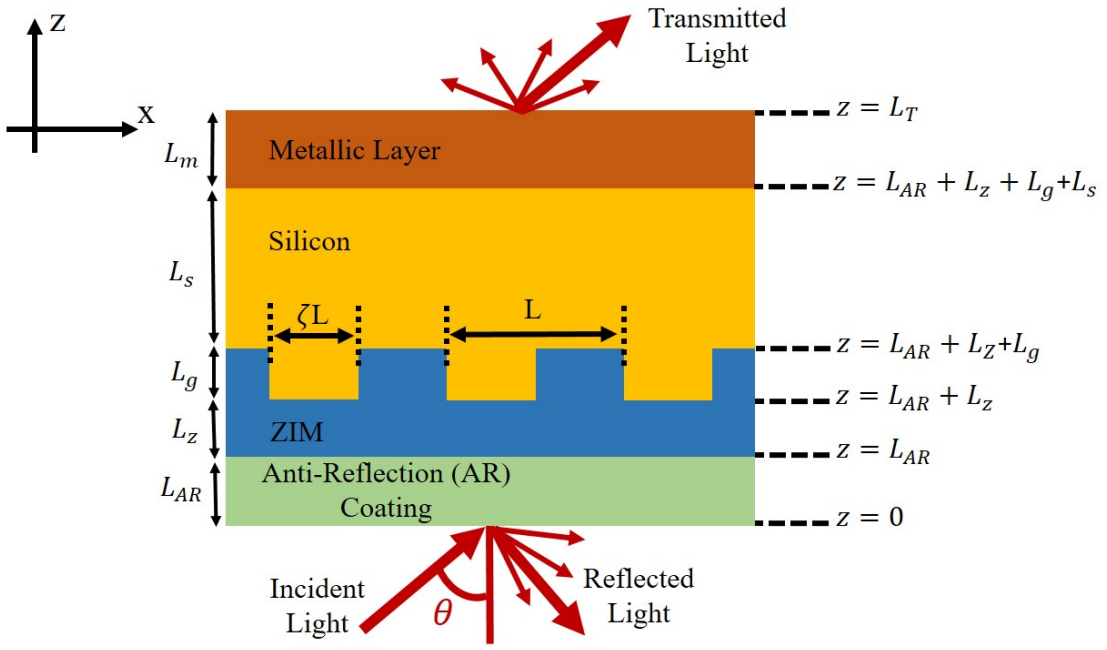

Fig. 5.1 Schematic representation of the geometry of the boundary-value problem. The periodically corrugated ZIM is a one-dimensional surface-relief grating between a planar AR coating and the active material of the solar cell (silicon).

made of ZIM with relative permittivity ε_z and relative permeability μ_z, and thickness L_z. The region between $z > L_{AR} + L_z$ and $z < L_{AR} + L_z + L_g$ is a rectangular one-dimensional surface-releif grating along x axis with depth L_g, period L, and duty cycle $\zeta \in (0,1)$, with the relative permittivity $\varepsilon_g(x,z) = \varepsilon_g(x \pm L, z)$ and the relative permeability $\mu_g(x,z) = \mu_g(x \pm L, z)$. The region between $z > L_{AR} + L_z + L_g$ and $z < L_{AR} + L_z + L_g + L_s$ is occupied by crystalline silicon with relative permittivity ε_s and relative permeability μ_s, and thickness L_s. The region between $z > L_{AR} + L_z + L_g + L_s$ and $z < L_t$ is a metallic layer with relative permittivity ε_m and relative permeability μ_m, and thickness L_m, where $L_t = L_{AR} + L_z + L_g + L_s + L_m$. The semi-infinite medium $z > L_t$ is a transmission medium with relative permittivity ε_t and relative permeability μ_t.

Let a plane wave propagating in the region $z < 0$ incident on $z = 0$ interface making an angle θ with the z axis. The incident, reflected, and transmitted electric and magnetic field phasors in terms of Floquet harmonics can be written as

$$\mathbf{E}_{\text{inc}}(\mathbf{r}) = \sum_{\ell \in \mathbb{Z}} \left[\hat{\mathbf{s}}_\ell a_s^{(\ell)} + \hat{\mathbf{p}}_\ell^+ a_p^{(\ell)} \right] \exp\left\{ i[k_x^{(\ell)} x + k_{za}^{(\ell)} z] \right\}, \quad z \leqslant 0, \tag{5.1}$$

$$\eta_0 \mathbf{H}_{\text{inc}}(\mathbf{r}) = n_a \sum_{\ell \in \mathbb{Z}} \left[\hat{\mathbf{p}}_\ell^+ a_s^{(\ell)} - \hat{\mathbf{s}}_\ell a_p^{(\ell)} \right] \exp\left\{ i[k_x^{(\ell)} x + k_{za}^{(\ell)} z] \right\}, \quad z \leqslant 0, \tag{5.2}$$

$$\mathbf{E}_{\text{ref}}(\mathbf{r}) = \sum_{\ell\in\mathbb{Z}} \left[\hat{\mathbf{s}}_\ell r_s^{(\ell)} + \hat{\mathbf{p}}_\ell^- r_p^{(\ell)}\right] \exp\left\{i[k_x^{(\ell)}x - k_{za}^{(\ell)}z]\right\}, \quad z \leqslant 0\,, \tag{5.3}$$

$$\eta_0\mathbf{H}_{\text{ref}}(\mathbf{r}) = n_a \sum_{\ell\in\mathbb{Z}} \left[\hat{\mathbf{p}}_\ell^- r_s^{(\ell)} - \hat{\mathbf{s}}_\ell r_p^{(\ell)}\right] \exp\left\{i[k_x^{(\ell)}x - k_{za}^{(\ell)}z]\right\}, \quad z \leqslant 0\,, \tag{5.4}$$

$$\mathbf{E}_{\text{tr}}(\mathbf{r}) = \sum_{\ell\in\mathbb{Z}} \left[\hat{\mathbf{s}}_\ell t_s^{(\ell)} + \hat{\mathbf{p}}_\ell^t t_p^{(\ell)}\right] \exp\left\{i[k_x^{(\ell)}x + k_{zt}^{(\ell)}(z-L_t)]\right\}, \quad z \geqslant L_t\,, \tag{5.5}$$

$$\eta_0\mathbf{H}_{\text{tr}}(\mathbf{r}) = n_t \sum_{\ell\in\mathbb{Z}} \left[\hat{\mathbf{p}}_\ell^t t_s^{(\ell)} - \hat{\mathbf{s}}_\ell t_p^{(\ell)}\right] \exp\left\{i[k_x^{(\ell)}x + k_{zt}^{(\ell)}(z-L_t)]\right\}, \quad z \geqslant L_t\,, \tag{5.6}$$

where

$$k_x^{(\ell)} = k_0 n_a \sin\theta + \ell\kappa_x\,,\ \kappa_x = 2\pi/L, \tag{5.7}$$

$$k_{za}^{(\ell)} = \sqrt{\left[k_0 n_a\right]^2 - \left[k_x^{(\ell)}\right]^2}, \tag{5.8}$$

$$k_{zt}^{(\ell)} = \sqrt{\left[k_0 n_t\right]^2 - \left[k_x^{(\ell)}\right]^2}, \tag{5.9}$$

where n_a and n_t are the refractive indices of the incidence and the transmission medium. In Eqs. (5.1)–(5.6), $a_s^{(0)}$ and $a_p^{(0)}$ are the amplitudes of the s- and p-polarized incident plane waves, respectively, and $a_s^{(\ell)} = a_p^{(\ell)} = 0 \forall\, \ell \neq 0$. Furthermore, $r_s^{(\ell)}$ and $t_s^{(\ell)}$ are unknown amplitudes of the Floquet harmonics of order ℓ in the s-polarized reflected and transmitted fields, respectively. Similarly, $r_p^{(\ell)}$ and $t_p^{(\ell)}$ are the amplitudes of the Floquet harmonics of order ℓ in the p-polarized reflected and transmitted fields, respectively, where ℓ is the order of Floquet harmonics with $\ell \in \{0, \pm1, \pm2, \pm3...\}$. Let us note that $\ell = 0$ represents the specular component of the reflected and transmitted field, and $\ell \neq 0$ are the non-specular components.

The s-polarization state is represented by the unit vector

$$\hat{\mathbf{s}}_\ell = \hat{\mathbf{u}}_y\,, \tag{5.10}$$

the p-polarization state of the incident and reflected waves is represented by

$$\hat{\mathbf{p}}_\ell^{\pm} = \frac{\mp k_{zp}^{(\ell)}\hat{\mathbf{u}}_x + k_x^{(\ell)}\hat{\mathbf{u}}_z}{k_0 n_a}\,, \tag{5.11}$$

and the p-polarization state of the transmitted wave is represented by

$$\hat{\mathbf{p}}_\ell^t = \frac{k_{zt}^{(\ell)}\hat{\mathbf{u}}_x + k_x^{(\ell)}\hat{\mathbf{u}}_z}{k_0 n_t}\,. \tag{5.12}$$

The RCWA demands that all the field phasors and permittivity are expressed as Fourier series with respect to x [30, 29, 34]. Fourier series for the relative permittivity and the relative permeability can be written as

$$\varepsilon(x,z) = \sum_{\ell=-\infty}^{\infty} \varepsilon^{(\ell)}(z) \exp(i\ell\kappa_x x)\,, \quad z \in [0, L_t]\,, \tag{5.13}$$

and

$$\mu(x,z) = \sum_{\ell=-\infty}^{\infty} \mu^{(\ell)}(z) \exp(i\ell\kappa_x x)\,, \quad z \in [0, L_t]\,, \tag{5.14}$$

respectively, where

$$\varepsilon^{(0)}(z) = \begin{cases} \varepsilon_{AR}\,, & z \in [0, L_{AR}]\,, \\ \varepsilon_z\,, & z \in [L_{AR}, L_{AR}+L_z]\,, \\ \frac{1}{L}\int_0^L \varepsilon_g(x,z)dx\,, & z \in (L_{AR}+L_z, L_{AR}+L_z+L_g)\,, \\ \varepsilon_s\,, & z \in [L_{AR}+L_z+L_g, L_{AR}+L_z+L_g+L_s]\,, \\ \varepsilon_m\,, & z \in [L_{AR}+L_z+L_g+L_s, L_t]\,, \end{cases} \tag{5.15}$$

$$\mu^{(0)}(z) = \begin{cases} \mu_{AR}\,, & z \in [0, L_{AR}]\,, \\ \mu_z\,, & z \in [L_{AR}, L_{AR}+L_z]\,, \\ \frac{1}{L}\int_0^L \mu_g(x,z)dx\,, & z \in (L_{AR}+L_z, L_{AR}+L_z+L_g)\,, \\ \mu_s\,, & z \in [L_{AR}+L_z+L_g, L_{AR}+L_z+L_g+L_s]\,, \\ \mu_m\,, & z \in [L_{AR}+L_z+L_g+L_s, L_t]\,, \end{cases} \tag{5.16}$$

and

$$\varepsilon^{(\ell)}(x,z) = \begin{cases} \frac{1}{L}\int_0^L \varepsilon_g(x,z)\exp(-i\ell\kappa_x x)dx\,, & \ell \neq 0\,, \quad z \in (L_{AR}+L_z, L_{AR}+L_z+L_g)\,, \\ 0\,, & \text{otherwise}\,, \end{cases} \tag{5.17}$$

$$\mu^{(\ell)}(x,z) = \begin{cases} \frac{1}{L}\int_0^L \mu_g(x,z)\exp(-i\ell\kappa_x x)dx\,, & \ell \neq 0\,, \quad z \in (L_{AR}+L_z, L_{AR}+L_z+L_g)\,, \\ 0\,, & \text{otherwise}\,. \end{cases} \tag{5.18}$$

Similarly, the field phasors in terms of Floquet harmonics in region $0 \leqslant z \leqslant L_t$ can be written as

$$\left.\begin{aligned}\mathbf{E}(\mathbf{r}) &= \sum_{\ell=-\infty}^{\infty}\left[E_x^{(\ell)}(z)\hat{\mathbf{u}}_x + E_y^{(\ell)}(z)\hat{\mathbf{u}}_y + E_z^{(\ell)}(z)\hat{\mathbf{u}}_z\right]\exp\left\{i[k_x^{(\ell)}x]\right\}\\ \mathbf{H}(\mathbf{r}) &= \sum_{\ell=-\infty}^{\infty}\left[H_x^{(\ell)}(z)\hat{\mathbf{u}}_x + H_y^{(\ell)}(z)\hat{\mathbf{u}}_y + H_z^{(\ell)}(z)\hat{\mathbf{u}}_z\right]\exp\left\{i[k_x^{(\ell)}x]\right\}\end{aligned}\right\}, \quad z \in [0, L_t]. \tag{5.19}$$

The remaining method is a specialized case of the method described in Chapter 2 with angle $\psi = 0$. The matrix ordinary differential equation obtained is given by

$$\frac{d}{dz}\left[\mathbf{f}(z)\right] = i\left[\underline{\underline{P}}(z)\right]\cdot\left[\mathbf{f}(z)\right], \qquad z \in (0, L_t), \tag{5.20}$$

where $[\mathbf{f}(z)]$ is a column vector with $4(2N_t+1)$ components given as

$$\left[\mathbf{f}(z)\right] = \left[[\mathbf{E}_x(z)]^T, [\mathbf{E}_y(z)]^T, \eta_0[\mathbf{H}_x(z)]^T, \eta_0[\mathbf{H}_y(z)]^T\right]^T, \tag{5.21}$$

and $4(2N_t+1)\times 4(2N_t+1)$ matrix $[\underline{\underline{P}}(z)]$ is

$$\left[\underline{\underline{P}}(z)\right] = \begin{bmatrix}[\underline{\underline{0}}] & [\underline{\underline{0}}] & [\underline{\underline{0}}] & \left[\underline{\underline{P}}_{14}(z)\right]\\ [\underline{\underline{0}}] & [\underline{\underline{0}}] & \left[\underline{\underline{P}}_{23}(z)\right] & [\underline{\underline{0}}]\\ [\underline{\underline{0}}] & \left[\underline{\underline{P}}_{32}(z)\right] & [\underline{\underline{0}}] & [\underline{\underline{0}}]\\ \left[\underline{\underline{P}}_{41}(z)\right] & [\underline{\underline{0}}] & [\underline{\underline{0}}] & [\underline{\underline{0}}]\end{bmatrix}, \tag{5.22}$$

with

$$\left[\underline{\underline{P}}_{14}(z)\right] = k_0\left[\underline{\underline{\mu}}(z)\right] - \frac{1}{k_0}\left[\underline{\underline{K}}_x\right]\cdot\left[\underline{\underline{\varepsilon}}(z)\right]^{-1}\cdot\left[\underline{\underline{K}}_x\right], \tag{5.23}$$

$$\left[\underline{\underline{P}}_{23}(z)\right] = -k_0\left[\underline{\underline{\mu}}(z)\right], \tag{5.24}$$

$$\left[\underline{\underline{P}}_{32}(z)\right] = \frac{1}{k_0}\left[\underline{\underline{K}}_x\right]\cdot\left[\underline{\underline{\mu}}(z)\right]^{-1}\cdot\left[\underline{\underline{K}}_x\right] - k_0\left[\underline{\underline{\varepsilon}}(z)\right], \tag{5.25}$$

$$\left[\underline{\underline{P}}_{41}(z)\right] = k_0\left[\underline{\underline{\varepsilon}}(z)\right], \tag{5.26}$$

where $[\underline{\underline{0}}]$ is a $(2N_t+1)\times(2N_t+1)$ null matrix.

5.2.1 Solar-Spectrum-Integrated (SSI) Absorption

The solar-spectrum-integrated (SSI) absorption efficiency of light can be defines as

$$SSI\,Absorption = \frac{\int (A_t \times AM1.5) d\lambda}{\int (AM1.5) d\lambda}, \; t \in [p,s], \tag{5.27}$$

where A_t is the absorptance and t in the subscript represents the p- or s- polarized light, and $AM1.5$ is the solar spectrum.

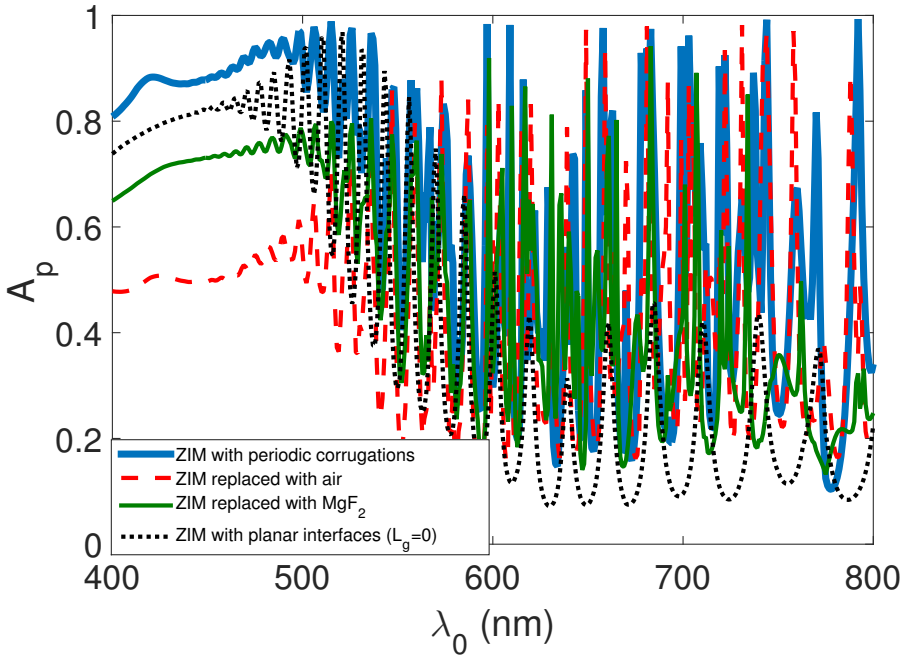

Fig. 5.2 Absorptance A_p for p-polarized incident light as a function of wavelength λ_0 for four different configurations. Other parameters are $L_{AR} = 80$ nm, $L_z = 80$ nm, $L_g = 80$ nm, $L_s = 2000$ nm, $L_m = 80$ nm, and $L = 600$ nm.

5.3 Numerical Results

To analyze the effect of periodically corrugated ZIM layer on the enhancement of light absorption in solar cells, we implemented the RCWA in Matlab and computed reflectances, transmittances, and absorptances to elucidate the effect of the ZIM corrugated layer on the

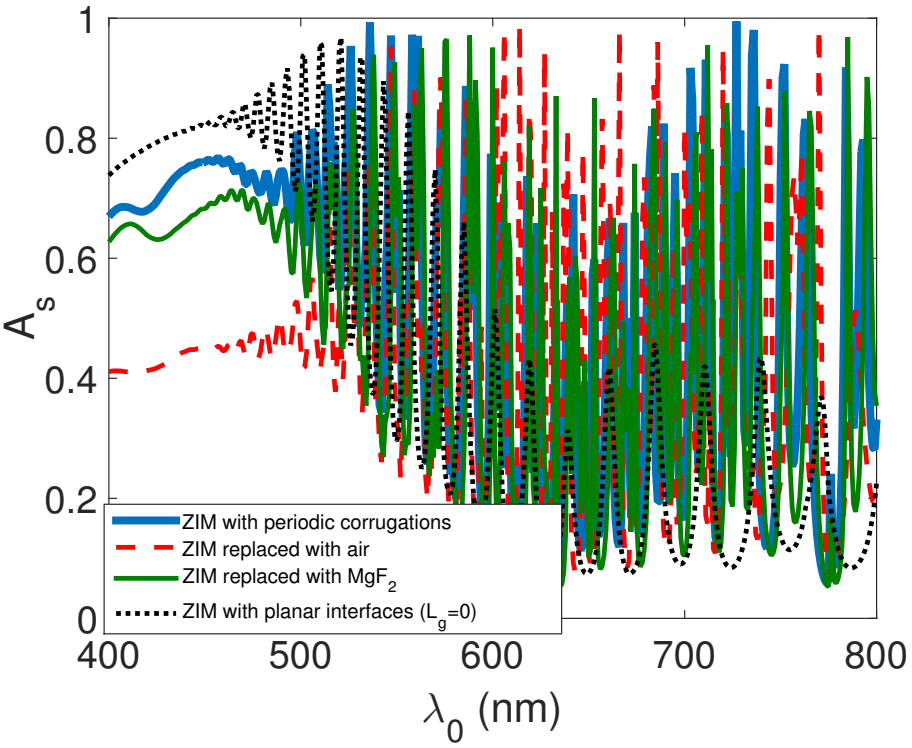

Fig. 5.3 Same as Fig. 5.2 except for *s*-polarized incident light.

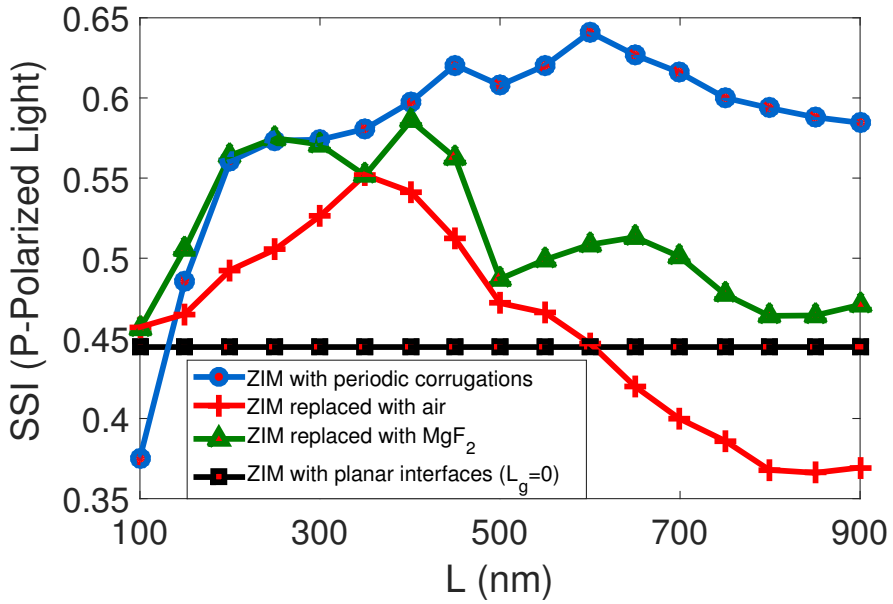

Fig. 5.4 Solar spectrum integrated (SSI) Absorption for *p*-polarized incident light as a function of period L for four different configurations as described in Fig. 5.2 (all other parameters are same).

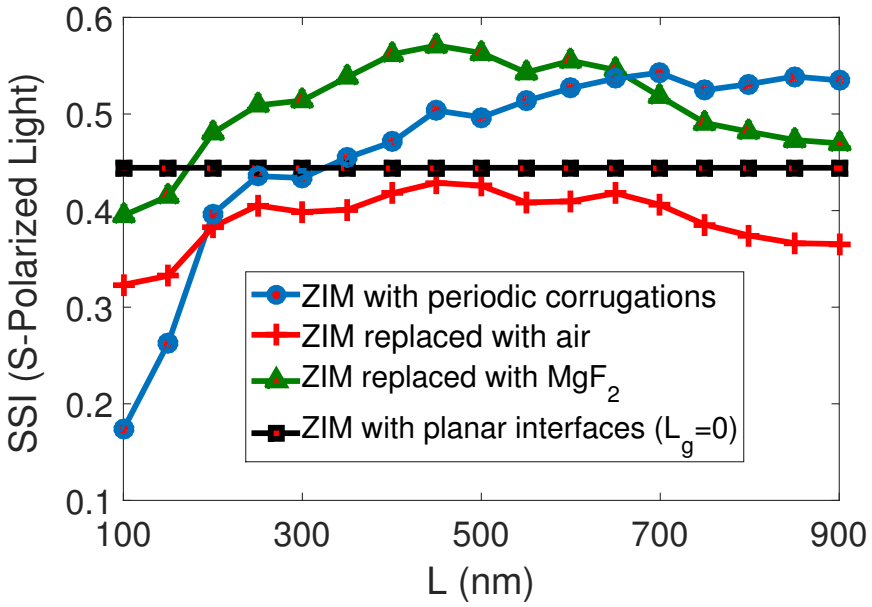

Fig. 5.5 Same as Fig. 5.4 except for *s*-polarized incident light.

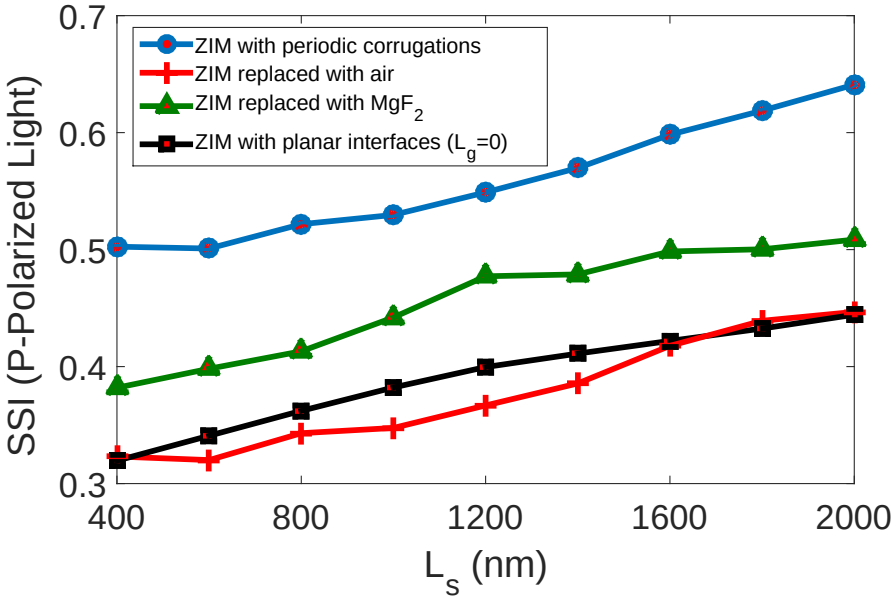

Fig. 5.6 SSI Absorption for *p*-polarized incident light as a function of thickness of silicon layer L_s for four different configurations as described in Fig. 5.2 (all other parameters are the same as in Fig. 5.2).

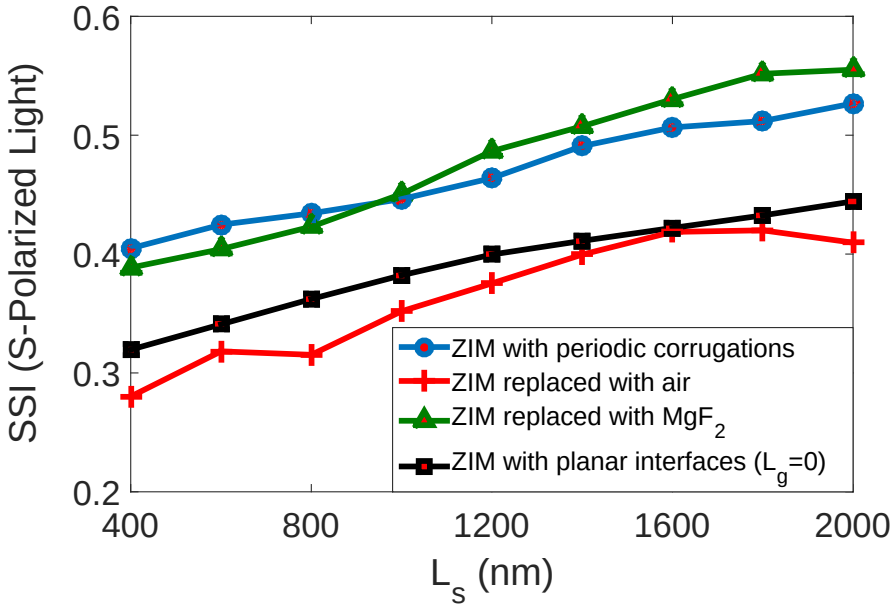

Fig. 5.7 Same as Fig. 5.6 except for *s*-polarized incident light.

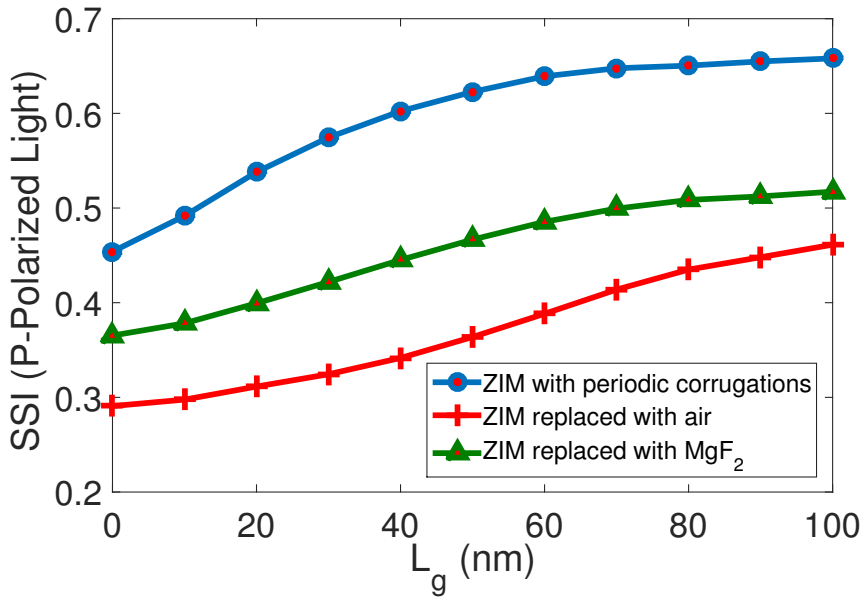

Fig. 5.8 SSI Absorption for *p*-polarized incident light as a function of depth L_g of the periodic corrugations for three different configurations (all other parameters are the same as in Fig. 5.2).

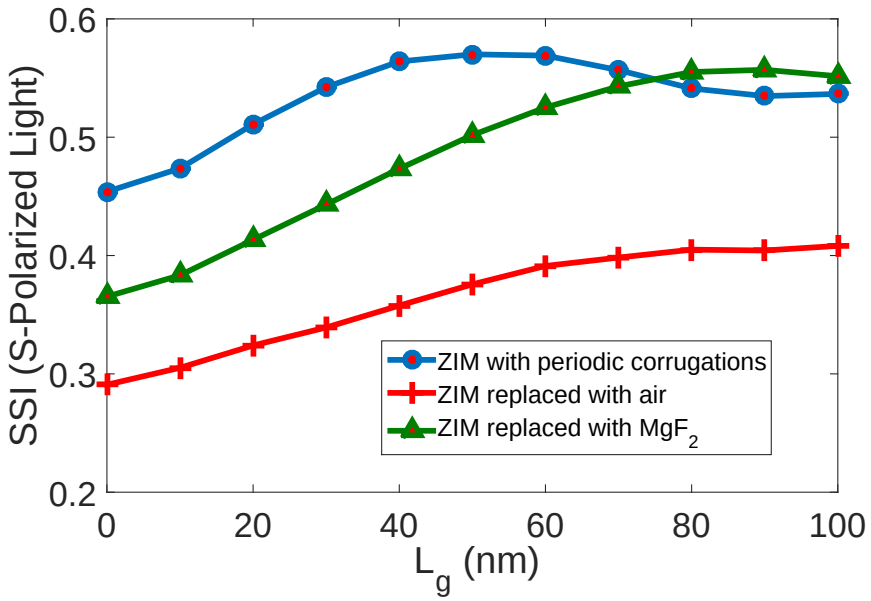

Fig. 5.9 Same as Fig. 5.8 except for s-polarized incident light.

top of the solar cell. We chose our one-dimensional grating to be rectangular with

$$\varepsilon_g(x,z) = \begin{cases} \varepsilon_z\,, & x \in (0,\zeta L)\,, \\ \varepsilon_s\,, & x \in (\zeta L, L)\,, \end{cases} \tag{5.28}$$

and

$$\mu_g(x,z) = \begin{cases} \mu_z\,, & x \in (0,\zeta L)\,, \\ \mu_s\,, & x \in (\zeta L, L)\,. \end{cases} \tag{5.29}$$

This also helped in speeding up the computations as each region in the solar cell is homogeneous along z axis and can be taken to comprise of one slice for the implementation of the RCWA. For representative results, the solar cell is taken to be made of crystalline silicon. On top of the ZIM layer, we assumed an anti-reflection layer of magnesium fluoride (MgF_2) with a thickness of 80 nm. This thin layer of magnesium fluoride helped in minimizing the reflections from the ZIM interface, so that maximum light gets in the active layer. The relative permittivity and the relative permeability of the ZIM layer were taken to be 0.01. Let us note that such ZIM materials with a constant near-zero-index do not yet exist. However, for this proof-of-concept study, this constant value is assumed. The idea is to show the effectiveness of the new design approach for the anti-reflection coatings. The consequence of this choice is that the proposed design will only work over the spectral of the ZIM where the index is nearly constant. The thickness of the ZIM layer and the metallic layer is 80 nm, for

the metallic layer we used gold (Au). The period L of the rectangular periodic corrugation is 600 nm, the duty cycle $\zeta = 0.5$, and the depth of periodic corrugation L_g is taken to be 80 nm. The parameter N_t is taken to be 15 in the simulation after ascertaining the convergence of the results within 0.5% of the results when $N_t = 16$ over the whole spectral range considered in this thesis. The refractive index of magnesium fluoride is taken from Ref. [122], silicon from Ref. [123], and gold is taken from Ref. [124]. Furthermore, all numerical results are presented for normal incidence $\theta = 0$.

To see the effect of the presence of the corrugated ZIM layer, the absorptances A_p for p- and A_s for s-polarized incident light as a function of wavelength (λ_0) are presented in Figs. 5.2 and 5.3, respectively, for the following four configurations:

- the ZIM layer having periodic corrugations,
- the ZIM layer is replaced with air,
- the ZIM layer is replaced with MgF_2, and
- the ZIM layer with the planar interfaces ($L_g = 0$).

Figures 5.2 and 5.3 show that the absorptances for ZIM layers are higher than when they are replaced with MgF_2 or air when λ_0 is small. When λ_0 is larger, the absorptances are oscillating as a function of λ_0. This is because silicon is very lossy at smaller wavelengths and losses reduce significantly when $\lambda_0 > 550$ nm. However, the absorptances, in general, are largest for the corrugated ZIM layers. This is more pronounced for the p-polarized case than for the s. This is in line with our expectations as the corrugations help trap the light inside the active layer (silicon). Let us note that the oscillations in the absorption in Figs. 5.2 and 5.3 are present regardless of the fact whether ZIM layer is present or not. This is because the silicon layer at larger wavelengths behave as a Fabry–Perot cavity. This is also confirmed by the increasing period of the oscillation as the wavelength increases because the width of the silicon layer as compared to operating wavelength decrease.

Since simple absorptance plots fail to show the actual impact of the ZIM layer directly, the SSI absorption efficiency was computed and analyzed. Figure 5.4 shows the SSI absorption efficiency for the p-polarized incident light as a function of the period L of the periodic corrugations of the ZIM layer. We can observe that the SSI absorption is considerably higher in the presence of the corrugated ZIM layer, supporting our hypothesis. Also, the variation with respect to the period L of the corrugation is small beyond a threshold value. The optimum value of SSI absorption efficiency is achieved at $L = 600$ nm. Figure 5.5 shows the SSI absorption efficiency for the s-polarized incident light as a function of the period L of the periodic corrugation. In this case, again the SSI absorption efficiency is higher when

the ZIM layer is present. Here again the SSI absorption increases with the increase of period L and remains more-or-less constant beyond a threshold value. This constant enhancement beyond a threshold value of L indicates the robustness of the ZIM layer as AR coating. This also makes sense if we consider the properties of the ZIM as they allow the coupling of light only when the incident wavefront of light and the interface has same shape to allow the constancy of the phase inside the ZIM.

To see if the proposed scheme of light trapping using a corrugated ZIM layer is valid for thin-film or thick-film solar cells, we have also plotted SSI absorption efficiency as a function of the thickness of silicon layer (L_s). Figure 5.6 shows SSI absorption of a p-polarized incident light as a function of thickness of silicon layer (L_s) for a fixed value of the period L. It can be observed that the ZIM layer with the periodic corrugation is absorbing maximum light. Also silicon is the main absorbing layer in the solar cell, that is why by increasing the thickness of the silicon layer the SSI absorption also increases. Figure 5.7 shows the SSI absorption for s-polarized incident light as a function of thickness of silicon layer (L_s). Both the figures show that the corrugated ZIM layer gives the maximum SSI absorption efficiency for a thickness of the active layer from 400 nm to 2 μm. Therefore, the proposed design of the anti-reflection coating is useful for the thin as well thick solar cells.

To check the dependence of SSI absorption efficiency on the depth of the periodic corrugations L_g, Fig. 5.8 shows the SSI absorption as a function of depth L_g. It can be observed that by increasing the depth L_g of periodic corrugations the SSI absorption also increases. Even at a very small value of L_g, the SSI absorption is higher in the case of ZIM layer, this is the evidence that the presence of periodic corrugations helped in enhancement of the light abortion in solar cell. Figure 5.9 shows the SSI absorption as a function of L_g for s-polarized incident light. In this case again we can see that the SSI absorption showing results which are consistent with our hypothesis. Let us also note that the transmittance for our chosen solar cells is negligible for all cases because of a thick metallic back reflector. Therefore, all enhancement in the absorption is due to the decrease in the reflectance.

5.4 Conclusions

A new concept of anti-reflection coatings for the solar cells is discussed for the maximum absorption of light. The proposed scheme uses the zero-index metamaterials (ZIM) with the rectangular surface-relief grating, which found to be enhanced the light absorption significantly for both the p- and the s- polarized incident light. A coating of ZIM with planar out surface and periodically corrugated inner surface was numerically investigated and the

integrated absorption efficiency for an AM1.5 incident solar flux is computed. This scheme work with the same efficiency regardless of the thickness of the active layer of the solar cells.

Chapter 6

Concluding Remarks and Future Directions

In this thesis, the problems of scattering by gratings were considered in inverted geometry using the coupled-wave approach when the incidence was from the planar side of the grating. The first application was the SPP waves guided by an interface of a metal and a dielectric material. This configuration was numerically investigated for optical sensing. A new scheme was introduced by combining a prism on the planar side of the grating to excite the SPP waves. The new geometry was an inverted grating with a prism attached to the planar side of the grating. Two types of absorptance peaks were present to provide two different angles of incidence to sense the same analyte and increased confidence in measurement. Sensitivity of each peak present in the absorptance spectrum was also computed. Sensitivity for the $\ell = 0$ peaks (due to prism) was found to be higher than the sensitivity for the $\ell = 1$ peaks (due to grating). Results for both angular and wavelength interrogation schemes were discussed for this novel sensor. The proposed configuration in this thesis can be used to build more sensitive and more reliable plasmonic sensor. The sensitivity in the geometry proposed in this work can be tuned by changing the prism refractive index and the grating period.

The second application was the excitation of SPP waves guided by the interface of a metal and a one-dimensional photonic crystal (1DPC) propagating along the direction of periodicity of the photonic crystal. Finite widths of metal and the 1DPC were used with the prism-coupled configuration to excite the SPP wave. Those absorptance bands were identified for plane wave incidence that remain unchanged by a change in the thickness of the 1DPC. The absorptance bands computed using the rigorous coupled-wave approach (RCWA) agreed excellently with the prediction of the canonical boundary-value problem. The spatial profiles of the power density showed an excellent localization of the SPP waves

to the metal/1DPC interface. The excitation angle in the prism-coupled configuration wass in full agreement with the dispersion relation previously developed in [101].

In the third application, we proposed and theoretically analyzed a new concept of anti-reflection coatings for solar cells. These coatings were made of zero-index metamaterials (ZIM). The ZIM transmit light through them only if the incident light has the same phase front as the shape of the incidence interface. Therefore, a coating with a planar outer surface and periodically corrugated inner surface was numerically investigated to see its effect on the integrated absorption efficiency for an AM1.5 incident solar flux. It was found that these coatings enhance the light absorption significantly for both the *p*- and the *s*- polarized incident light. Furthermore, it was found to work with the same efficiency regardless of the thickness of the active layer of the solar cells.

We hope that the inverted geometry explained in this thesis will open new avenues for the applications in the field of optical sensing, imaging, solar energy harvesting, and waveguides. In our work, the gratings are illuminated from the planar interface. This proposed geometry for the excitation of surface waves in grating-coupled configuration can easily be integrated with the modern chip based technology. These chips are planar. Therefore, the integration with the electronic circuitry is easy with the planar interface. That is why the grating-coupled configuration is popular choice than the prism-coupled configuration for integration of optics with electronics.

The work presented in this thesis provides a basic framework for plasmonic sensors using combined prism and gratings couplings, SPP waves along the direction of periodicity, and ZIM anti-reflection coatings. In future, these foundations can be built upon to construct more reliable and sensitive sensors by exploring the combinations of prism and grating couplings of more exotic sort, for example, by combing sensitive hyperbolic prism-coupled sensors with gratings, or layered structures enabling long-range SPP waves. Similarly, the SPP waves propagating along the direction of periodicity guided by the interface of 1DPC and metal can be explored for plasmonic sensors. Also, oblique propagation at this interface can be investigated to find more general characteristics of SPP waves guided by such interface. Finally, the idea of ZIM anti-reflection coatings can be further established by considering more realistic geometries of solar cells that usually have multiple layers instead of one active layer considered in this thesis. Also, in addition to the 1D gratings investigated in this thesis, 2D gratings can be investigated to further explore the three concepts presented in this thesis. Therefore, the work presented in this thesis can engender new research areas in plasmonics and solar cells in the near future.

References

[1] N. A. Hall and F. L. Degertekin, "Integrated optical interferometric detection method for micromachined capacitive acoustic transducers," Appl. Phys. Lett. **80**, 3859–3861 (2002).

[2] T. K. Gaylord and M. G. Moharam, "Analysis and applications of optical diffraction by gratings," Proc. IEEE **73**, 894–937 (1985).

[3] H. Kogelnik, "Coupled wave theory for thick hologram gratings," Bell Syst. Tech. J. **48**, 2909–2947 (1969).

[4] E. G. Loewen, "Diffraction gratings for spectroscopy," J. Phys. E: Sci. Instrum. **3**, 953–961 (1970).

[5] M. Faryad and A. Lakhtakia, "Grating-coupled excitation of multiple surface plasmon-polariton waves," Phys. Rev. A **84**, 033852 (2011).

[6] P. Sheng, A. N. Bloch, and R. S. Stepleman, "Wavelength-selective absorption enhancement in thin-film solar cells," Appl. Phys. Lett. **43**, 579–581 (1983).

[7] C. Heine and R. H. Morf, "Submicrometer gratings for solar energy applications," Appl. Opt. **34**, 2476–2482 (1995).

[8] V. E. Ferry, M. A. Verschuuren, H. B. T. Li, E. Verhagen, R. J. Walters, R. E. I. Schropp, H. A. Atwater, and A. Polman, "Light trapping in ultrathin plasmonic solar cells," Opt. Exp. **18**, A237–A245 (2010).

[9] F. Wnag, M. W. Horn, and A. Lakhtakia, "Rigorous electromagnetic modeling of near-field phase-shifting contact lithography," Microelectron. Eng. **71**, 34–53 (2004).

[10] F. Wang, K. E. Weaver, A. Lakhtakia, and M. W. Horn, "Electromagnetic modeling of near-field phase-shifting contact lithography with broadband ultraviolet illumination," Optik **116**, 1–9 (2005).

[11] I. Shariv, Y. Amitai, and A. A. Friesem, "Compact holographic beam expander," Opt. Lett. **18**, 1268–1270 (1993).

[12] R. Shechter, Y. Amitai, and A. A. Friesem, "Compact beam expander with linear gratings," Appl. Opt. **41**, 1236–1240 (2002).

[13] D. L. Brundrett, T. K. Gaylord, and E. N. Glytsis, "Polarizing mirror/absorber for visible wavelengths based on a silicon subwavelength grating: design and fabrication," Appl. Opt. **37**, 2534–2541 (1998).

[14] D. C. Flanders, "Submicrometer periodicity gratings as artificial anisotropic dielectrics," Appl. Phys. Lett. **42**, 492–494 (1983).

[15] S. Aoyama and T. Yamashita, "Grating beam splitting polarizer using multilayer resist method," Proc SPIE **1545**, 241–250 (1991).

[16] M. Quintanilla and A. M. de Frutos, "Holographic filter that transforms a Gaussian into a uniform beam," Appl. Opt. **20**, 879–880 (1981).

[17] C. Y. Han, Y. Ishii, and K. Murata, "Reshaping collimated laser beams with Gaussian profile to uniform profiles," Appl. Opt. **22**, 3644–3647 (1983).

[18] S. Ura, T. Suhara, H. Nishihara, and J. Koyama, "An integrated-optic disk pickup device," J. Lightwave Tech. **4**, 913–918 (1986).

[19] S. Nishiwaki, J. Asada, and S. Uchida, "Optical head employing a concentriccircular focusing grating coupler," Appl. Opt. **33**, 1819–1827 (1994).

[20] S. Ura, H. Sunagawa, T. Suhara, and H. Nishihara, "Focusing grating couplers for polarization detection," J. Lightwave Tech. **6**, 1028–1033 (1988).

[21] T. Suhara, T. Taniguchi, M. Uemukai, H. Nishihara, T. Hirata, S. Iio, and M. Suehiro, "Monolithic integrated-optic position/displacement sensor using waveguide gratings and QW-DFB laser," IEEE Photon. Lett. **7**, 1195–1197 (1995).

[22] T. Suhara, N. Nozaki, and H. Nishihara, "An integrated acoustooptic printer head," Proceedings of the Fourth European Conference on Integrated Optics **87**, 119–122 (1987).

[23] M. G. Moharam and T. K. Gaylord, "Rigorous coupled-wave analysis of planar-grating diffraction," J. Opt. Soc. Am. **71**, 811–818 (1981).

[24] M. G. Moharam and T. K. Gaylord, "Diffraction analysis of dielectric surface-relief gratings," J. Opt. Soc. Am. **72**, 1385–1392 (1982).

[25] M. G. Moharam and T. K. Gaylord, "Three-dimensional vector coupled-wave analysis of planar grating diffraction," J. Opt. Soc. Am. **73**, 1105–1112 (1983).

[26] M. G. Moharam and T. K. Gaylord, "Rigorous coupled-wave analysis of metallic surface-relief gratings," J. Opt. Soc. Am. **3**, 1780–1787 (1986).

[27] E. N. Glytsis and T. K. Gaylord, "Rigorous three-dimensional coupled-wave diffraction analysis of single and cascaded anisotropic gratings," J. Opt. Soc. Am. A **4**, 2061–2080 (1987).

[28] N. Chateau and J. P. Hugonin, "Algorithm for the rigorous coupled-wave analysis of grating diffraction," J. Opt. Soc. Am. A **11**, 1321–1331 (1994).

[29] M. G. Moharam, E. B. Grann, D. A. Pommet, and T. K. Gaylord, "Formulation for stable and efficient implementation of the rigorous coupled-wave analysis of binary gratings," J. Opt. Soc. Am. A **12**, 1068–1076 (1995).

[30] L. Li, "Multilayer modal method for diffraction gratings of arbitrary profile, depth, and permittivity," J. Opt. Soc. Am. A **10**, 2581–2591 (1993).

[31] H. Raether, *Surface Plasmons on Smooth and Rough Surfaces and on Gratings*, (Springer-Verlag, New York 1988).

[32] I. Abdulhalim, M. Zourob, and A. Lakhtakia, "Surface plasmon resonance for biosensing: a mini-review," Electromagnetics **28**, 214–242 (2008).

[33] J. Homola, *Surface Plasmon Resonance Based Sensors*, (Springer, Heidelberg, 2006).

[34] J. A. Polo, T. G. Mackay, and A. Lakhtakia, *Electromagnetic surface waves: A modern perspective* (Elsevier, 2013).

[35] T. Turbadar, "Complete absorption of light by thin metal films," Proc Phys Soc. **73**, 40–44 (1959).

[36] E. Kretschmann and H. Raether, "Radiative decay of nonradiative surface plasmons excited by light," Z. Naturforsch **A23**, 2135–2136 (1968).

[37] A. Otto, "Excitation of nonradiative surface plasma waves in silver by the method of frustrated total reflection," Z. Phys **216**, 398–410 (1968).

[38] P. C. Waterman, "Scattering by periodic surfaces," J. Acoust. Soc. Am. **57**, 791–802 (1975).

[39] A. Lakhtakia, V. K. Varadan, and V. V. Varadan, "On filling up the grooves of a perfectly conducting grating with a dielectric material," J. Mod. opt. **38**, 659–669 (1991).

[40] J. Chandezon, M. T. Dupuis, G. Cornet, and D. Maystre, "Multicoated gratings: a differential formalism applicable in the entire optical region," J. Opt. Soc. Am. **72**, 839–846 (1982).

[41] G. I. Stegeman, R. F. Wallis, and A. A. Maradudin, "Excitation of surface polaritons by end-fire coupling," Opt. Lett. **8**, 386–389 (1983).

[42] B. S. Boruah and R. Biswas, "An optical fiber based surface plasmon resonance technique for sensing of lead ions: A toxic water pollutant", Opt. Fiber Technol. **40**, 152-156 (2018).

[43] M. H. F. Meyer, M. Hartmann, and M. Keusgen, "SPR-based immunosensor for the CRP detection – A new method to detect a well known protein", Biosens. Bioelectron. **21**, 1987-1990 (2006).

[44] J. Homola and M. Piliarik, "Surface plasmon resonance (SPR) sensors", Springer Ser Chem Sens Biosens **4**, 45–67 (2006).

[45] X. D. Hoa, A. G. Kirk, and M. Tabrizian, "Towards integrated and sensitive surface plasmon resonance biosensors: a review of recent progress," Biosens. Bioelectron. **23**, 151-160 (2007).

[46] A. Gombert and A. Luque, "Photonics in photovoltaic systems," Phys. Stat. Sol. (a) **205**, 2757–2565 (2008).

[47] H. A. Atwater and A. Polman, "Plasmonics for improved photovoltaic devices," Nature Mater. **9**, 205–213 (2010).

[48] M. Coakley, "Growth and Optical Characterization of Zinc Oxide Nanowires for Anti-reflection Coatings for Solar Cells," Dissertations and Theses. Paper 290 (2011). https://pdxscholar.library.pdx.edu/open_access_etds/290 , (accessed on 3 April, 2020).

[49] H. K. Raut, V. A. Ganesh, A. S. Nair, and S. Ramakrishna, "Anti-reflective coatings: A critical, in-depth review," Energy Environ. Sci. **4**, 3779–3804 (2011).

[50] D. Chen, Y. Yan, E. Westenberg, D. Niebauer, N. Sakaitani, S. Chaudhuri, Y. Sato, and M. Takamatsu, "Development of anti-reflection (AR) coating on plastic panels for display applications," J. Sol-Gel Sci. Technol. **19**, 77–82 (2000).

[51] S. Lee, S. Choi, and J. Yi, "Double-layer anti-reflection coating using MgF_2 and CeO_2 films on a crystalline silicon substrate," Thin Solid Films **376**, 208–213 (2000).

[52] A. Szeghalmi, M. Helgert, R. Brunner, F. Heyroth, U. Gösele, and M. Knez, "Atomic layer deposition of Al_2O_3 and TiO_2 multilayers for applications as bandpass filters and anti-reflection coatings," Appl. Opt. **48**, 1727–1732 (2009).

[53] J. H. Selj, A. Thøgersen, S. E. Foss, and E. S. Marstein, "Optimization of multilayer porous silicon antireflection coatings for silicon solar cells," J. Appl. Phys **107**, 074904 (2010).

[54] D. M. Braun and R. L. Jungerman, "Broadband multilayer antireflection coating for semiconductor laser facets," Opt. Lett. **20**, 1154–1156 (1995).

[55] S. J. Orfanidis, *Electromagnetic Waves and Antenna* (Chapter 6, https://www.ece.rutgers.edu/~orfanidi/ewa/, Accessed on 27 March 27 2020).

[56] N. Engheta and R. W. Ziolkowski, *Metamaterials: Physics and engineering explorations,* (John Wiley & Sons Inc., 2006).

[57] P. Markos and C. M. Soukoulis, "Transmission properties and effective electromagnetic parameters of double negative metamaterials," Opt. Express **11**, 649–661 (2003).

[58] U. K. Chettiar, A. V. Kildishev, H. K. Yuan, W. Cai, S. Xiao, V. P. Drachev, and V. M. Shalaev, "Dual-band negative index metamaterial: double negative at 813 nm and single negative at 772 nm," Opt. Lett. **32**, 1671–1673 (2007).

[59] Y. Li, S. Kita, P. Munoz, O. Reshef, D. I. Vulis, M. Yin, M. Loncar, and E. Mazur, "On-chip zero-index metamaterials," Nat. Photonics **9**, 738–742 (2015).

[60] R. W. Ziolkowski, " Propagation in and scattering from a matched metamaterial having a zero index of refraction," Phys. Rev. E **70**, 046608 (2004).

[61] C. E. Kriegler, M. S. Rill, S. Linden, and M. Wegener, "Bianisotropic photonic metamaterials," IEEE J. Sel. Top. Quantum Electron. **16**, 367–375 (2010).

[62] M. S. Rill, C. E. Kriegler, M. Thiel, G. V. Freymann, S. Linden, and M. Wegener, "Negative-index bianisotropic photonic metamaterial fabricated by direct laser writing and silver shadow evaporation," Opt. Lett. **34**, 19–21 (2009).

[63] J. Hao, W. Yan, and M. Qiu, "Super-reflection and cloaking based on zero index metamaterial," Appl. Phys. Lett. **96**, 101109 (2010).

[64] A. Alu, M. G. Silveirinha, A. Salandrino, and N. Engheta, "Epsilon-near-zero metamaterials and electromagnetic sources: tailoring the radiation phase pattern," Phys. Rev. B **75**, 155410 (2007).

[65] M. Silveirinha and N. Engheta, "Tunneling of electromagnetic energy through subwavelength channels and bends using epsilon-near-zero materials," Phys. Rev. Lett. **97**, 157403 (2006).

[66] V. C. Nguyen, L. Chen, and K. Halterman, "Total transmission and total reflection by zero index metamaterials with defects," Phys. Rev. Lett. **105**, 233908 (2010).

[67] L. Sun, K. W. Yu, and X. Yang, "Integrated optical devices based on broadband epsilon-near-zero meta-atoms," Opt. Lett. **37**, 3096–3098 (2012).

[68] W. Zhua, I. D. Rukhlenko, and M. Premaratne, "Light amplification in zero-index metamaterial with gain inserts," Appl. Phys. Lett. **101**, 031907 (2012).

[69] M. W. Ashraf and M. Faryad, "Dirac-like cone dispersion in two-dimensional core-shell dielectric photonic crystals," J. Nanophoton. **9**, 093057 (2015).

[70] M. W. Ashraf and M. Faryad, "On the mapping of Dirac-like cone dispersion in dielectric photonic crystals to an effective zero-index medium," J. Opt. Soc. Am. B **33**, 1008–1013 (2016).

[71] L. Sun, J. Gao, and X. Yang, "Broadband epsilon-near-zero metamaterials with steplike metal-dielectric multilayer structures," Phys. Rev. B **87**, 165134 (2013).

[72] Y. Li, B. Liang, Z. Gu, X. Zou, and J. Cheng, "Unidirectional acoustic transmission through a prism with near-zero refractive index," Appl. Phys. Lett. **103**, 053505 (2013).

[73] Y. Fu, L. Xu, Z. H. Hang, and H. Chen, "Unidirectional transmission using array of zero-refractive-index metamaterials," Appl. Phys. Lett. **104**, 193509 (2014).

[74] M. Faryad and A. Lakhtakia, "Multiple trains of same-color surface plasmon-polaritons guided by the planar interface of a metal and a sculptured nematic thin film. Part V: Grating-coupled excitation," J. Nanophoton. **5**, 053527 (2011).

[75] H. Q. Zhang, S. Boussaad, and N. J. Tao, "High-performance differential surface plasmon resonance sensor using quadrant cell photodetector," Rev. Sci. Instrum. **74**, 150–153 (2003).

[76] S. E. Swiontek, M. Faryad, and A. Lakhtakia, "Surface plasmonic polaritonic sensor using a dielectric columnar thin film," J. Nanophoton. **8**, 083986 (2014).

[77] J. Dostalek, H. Vaisocherova, J. Homola, "Multichannel surface plasmon resonance biosensor with wavelength division multiplexing," Sensors and Actuators B **108**, 758–764 (2005).

[78] C. E. Jordan, A. G. Frutos, A. J. Thiel, and R. M. Corn, "Surface plasmon resonance imaging measurements of DNA hybridization adsorption and streptavidin/DNA multilayer formation at chemically modified gold surfaces," Anal. Chem. **69**, 4939–4947 (1997).

[79] B. Sepulveda, A. Calle, L. M. Lechuga, and G. Armelles, "Highly sensitive detection of biomolecules with the magneto-optic surface-plasmon-resonance sensor," Opt. Lett. **31**, 1085–1087 (2006).

[80] W. Yuan, H. P. Ho, C. L. Wong, S. K. Kong and C. Lin, "Surface plasmon resonance biosensor incorporated in a michelson interferometer with enhanced sensitivity," IEEE Sensors J. **7**, 70–73 (2007).

[81] K. V. Sreekanth, Y. Alapan, M. ElKabbash, A. M. Wen, E. Ilker, M. Hinczewski, U. A. Gurkan, N. F. Steinmetz, and G. Strangi, "Enhancing the angular sensitivity of plasmonic sensors using hyperbolic metamaterials," Adv. Opt. Mater. **4**, 1767–1772 (2016).

[82] F. Abbas and M. Faryad, "A highly sensitive multiplasmonic sensor using hyperbolic chiral sculptured thin films," J. Appl. Phys. **122**, 173104 (2017).

[83] J. Homola, H. B. Lu, and S. S. Yee, "Dual-channel surface plasmon resonance sensor with spectral discrimination of sensing channels using dielectric overlayer," Electron. Lett. **35**, 1105–1106 (1999).

[84] J. Homola, H. B. Lu, G. G. Nenninger, J. Dostalek and S. S. Yee, "A novel multichannel surface plasmon resonance biosensor," Sensors and Actuators B **76**, 403–410 (2001).

[85] P. Adam, J. Dostalek, and J. Homola, "Multiple surface plasmon spectroscopy for study of biomolecular systems," Sensors and Actuators B **113**, 774–781 (2006).

[86] J. M. Brockman and S. M. Fernandez, "Grating-coupled surface plasmon resonance for rapid, label-free, array-based sensing, " The Royal Soc. of Chem. **33**, 37–40 (2001).

[87] J. Dostalek, J. Homola, and M. Miler, "Rich information format surface plasmon resonance biosensor based on array of diffraction gratings," Sensors and Actuators B **107**, 154–161 (2005).

[88] D. W. Unfricht, S. L. Colpitts, S. M. Fernandez and M. A. Lynes, "Grating-coupled surface plasmon resonance: A cell and protein microarray platform," Proteomics **5**, 4432–4442 (2005).

[89] F. C. Chien, C. Y. Lin, J. N. Yih, K. L. Lee, C. W. Chang, P. K. Wei, C. C. Sun, and S. J. Chen, "Coupled waveguide–surface plasmon resonance biosensor with subwavelength grating," Biosens. and Bioelectron. **22**, 2737–2742 (2007).

[90] C. Thirstrup, W. Zong, M. Borre, H. Neff, H.C. Pedersen, and G. Holzhueter, "Diffractive optical coupling element for surface plasmon resonance sensors," Sensors and Actuators B **100**, 298–308 (2004).

[91] L. Fan, M. Faryad, G. Barber, T. E. Mallouk, P. B. Monk, and A. Lakhtakia, "Optimization of a spectrum splitter using differential evolution algorithm for solar cell applications," J. Photonics Energy **5**, 055099 (2015).

[92] P. Yeh, A. Yariv, and A. Y. Cho, "Optical surface waves in periodic layered media," Appl. Phys. Lett. **32**, 104–105 (1978).

[93] M. Kaliteevski, I. Iorsh, S. Brand, R. A. Abram, J. M. Chamberlain, A. V. Kavokin, and I. A. Shelykh, "Tamm plasmon-polaritons: Possible electromagnetic states at the interface of a metal and a dielectric Bragg mirror," Phys. Rev. B **76**, 165415 (2007).

[94] V. N. Konopsky and E. V. Alieva, "Photonic crystal surface waves for optical biosensors," Anal. Chem. **79**, 4729–4735 (2007).

[95] M. Skorobogatiy and A. V. Kabashin, "Photon crystal waveguide-based surface plasmon resonance biosensor," Appl. Phys. Lett. **89**, 143518 (2006).

[96] E. Morino, L. Martín-Morino, and F. J. García-Vedal, "Efficient coupling of light into and out of a photonic crystal waveguide via surface modes," Photonics Nanostructures: Fundam. Appl. **2**, 97–102 (2004).

[97] P. Kramper, M. Agio, C. M. Soukoulis, A. Birner, F. Muller, R. B. Wehrspohn, U. Gosele, and V. Sandoghdar, "Highly directional emission from photonic crystal waveguides of subwavelength width," Phys. Rev. Lett. **92**, 113903 (2004).

[98] H. K. Baghbadorani, D. Aurelio, J. Barvestani, and M. Liscidini, "Guided modes in photonic crystal slabs supporting Bloch surface waves," J. Opt. Soc. Am. B **35**, 805–810 (2018).

[99] R. D. Meade, K. D. Brommer, A. M. Rappe, and J. D. Joannopoulos, "Electromagnetic Bloch waves at the surface of a photonic crystal," Phys. Rev. B **44**, 10961 (1991).

[100] J. Barvestani, M. Kalafi, A. Soltani-Vala, and A. Namdar, "Backward surface electromagnetic waves in semi-infinite one-dimensional photonic crystals containing left-handed materials," Phys. Rev. A **77**, 013805 (2008).

[101] M. Rasheed and M. Faryad, "Rigorous formulation of surface plasmon-polariton waves propagation along the direction of periodicity of one-dimensional photonic crystal," J. Opt. Soc. Am. B **35**, 2957–2962 (2018). Erratum: **36**, 1396-1396 (2019).

[102] M. Faryad and A. Lakhtakia, "Grating-coupled excitation of the Uller–Zenneck surface wave in the optical regime," J. Opt. Soc. Am. B **31**, 1706–1711 (2014).

[103] M. Faryad and A. Lakhtakia, "On surface plasmon-polariton waves guided by the interface of a metal and a rugate filter with a sinusoidal refractive-index profile," J. Opt. Soc. Am. B **27**, 2218–2223 (2010).

[104] M. Faryad, "Differentiating surface plasmon-polariton waves and waveguide modes guided by interfaces with one-dimensional photonic crystals," Appl. Phys. A **124**, 102 (2018).

[105] J. Fraunhofer, Versuche über die Ursachen des Anlaufens und Mattwerdens des Glases und die Mittel, denselben zuvorzukommen 33–49, (Joseph von Fraunhofer's Gesammelte Schriften, Munich, 1888).

[106] G. Chartier, *Introduction to Optics* (Springer, 2005).

[107] J. Zhao and M. A. Green, "Optimized anti-reflection coatings for high-efficiency silicon solar cells," IEEE Trans. Electron Devices **38**, 1925–1934 (1991).

[108] J. Zhang, P. A. R. Ade, P. Mauskopf, L. Moncelsi, G. Savini, and N. Whitehouse, " New artificial dielectric metamaterial and its application as a terahertz antireflection coating," Appl. Opt. **48**, 6635–6642 (2009).

[109] A. Deinega, I. Valuev, B. Potapkin, and Y. Lozovik, "Minimizing light reflection from dielectric textured surfaces," J. Opt. Soc. Am. A **28**, 770–777 (2011).

[110] Y. W. Chen, P. Y. Han, and X.-C. Zhang, "Tunable broadband antireflection structures for silicon at terahertz frequency," Appl. Phys. Lett. **94**, 041106 (2009).

[111] J. Kroll, J. Darmo, and K. Unterrainer, "Metallic wave-impedance matching layers for broadband terahertz optical systems," Opt. Express **15**, 6552–6560 (2007).

[112] A. Thoman, A. Kern, H. Helm, and M. Walther, "Nanostructured gold films as broadband terahertz antireflection coatings," Phys. Rev. B **77**, 195405 (2008).

[113] K. L. Chopra, P. D. Paulson, and V. Dutta, " Thin-film solar cells: an overview," Prog. Photovolt: Res. Appl. **12**, 69–92 (2004).

[114] A. Shah, P. Torres, R. Tscharner, N. Wyrsch, and H. Keppner, " Photovoltaic technology: The case for thin-film solar cells," Science **285**, 692–698 (1999).

[115] D. E. Carlson and C. R. Wronski, "Amorphous silicon solar cell," Appl. Phys. Lett. **28**, 671–673 (1976).

[116] F. J. Beck, A. Polman, and K. R. Catchpole, " Tunable light trapping for solar cells using localized surface plasmons," J. Appl. Phys. **105**, 114310 (2009).

[117] P. Campbell and M. A. Green, "Light trapping properties of pyramidally textured surfaces ," J. Appl. Phys. **62**, 243 (1987).

[118] K. J. Weber and A. W. Blakers, "A novel silicon texturization method based on etching through a silicon nitride mask," Prog. Photovolt: Res. Appl. **13**, 691–695 (2005).

[119] D. Zhou and R. Biswas, " Photonic crystal enhanced light-trapping in thin film solar cells," J. Appl. Phys. **103**, 093102 (2008).

[120] E. Garnett and P. Yang, " Light trapping in silicon nanowire solar cells," Nano Lett. **10**, 1082–1087 (2010).

[121] A. M. Mahmoud and N. Engheta, "Wave-matter interactions in epsilon-and-mu-near-zero structures," Nat. Commun. **5**, 5638 (2014).

[122] https://refractiveindex.info/?shelf=main&book=MgF2&page=Rodriguez-de_Marcos, for for the refractive index of magnesium fluoride; (accessed on 26 July, 2019).

[123] https://refractiveindex.info/?shelf=main&book=Si&page=Schinke, for for the refractive index of silicon; (accessed on 26 July, 2019).

[124] https://refractiveindex.info/?shelf=main&book=Au&page=McPeak, for for the refractive index of gold; (accessed on 26 July, 2019).

Chapter 7

Appendix 1

In this appendix the representative Matlab® codes are given for main results.

7.1 Code for Fig. 3.2

```
iota = sqrt(-1);
nm = 10^(-9);
lam_0 = 635*nm; %wavelength
epis =(0.14089+3.6318*iota)^2; %permittivity of gold
k_0=2*pi/lam_0; %wavenumber
L = 700*nm; %period
L1=0.5*L; %offset of grating
Lg = 40; %thickness of grating
Ld = 1000;  %thickness of dielectric material to be sensed
d1 = 20*nm;  %thickness of metal(gold)
d2=d1+Lg*nm;
d3=d2+Ld*nm;
Nt=21;  %number of terms in the summation
Nm=1;
Ng=40;
Nd=1;
Ns=Nd+Ng+Nm;
zero=zeros((2*Nt)+1);
iden=eye((2*Nt)+1);
A=zeros(((2*Nt)+1),1); %incidence for p-polarized light
```

```
A(Nt+1,1)=1;
step=(d2-d1)/Ng;
%%% plot angle
diff=0.1;
last=80;
%%%%%%%%%%%
for kf=1:0.1:1.5
epidd=(kf+0.0001*iota)^2;  %permittivity of dielectric material to be sensed
na=1.7;  %refractive index of prism
ng=kf+0*iota;  %refractive index of transmission medium
ag=1;
uu=1;
for tt=0:diff:last
    disp(tt)
        theta(uu)=tt*pi/180;
         aa=1;
        for n=-Nt:Nt
            kapa(aa)=(k_0*na*sin(theta(uu)))+n*(2*pi/L);
            alpha_na(aa)=sqrt(k_0^2*na^2-kapa(aa)^2);
            alpha_ng(aa)=sqrt(k_0^2*ng^2-kapa(aa)^2);
            aa=aa+1;
        end
        K=diag(kapa);
        alpa_na=diag(alpha_na);
        alpa_ng=diag(alpha_ng);
        Yinc_e=-alpa_na/(k_0*na);
        Yref_e=alpa_na/(k_0*na);
        Ytr_e=-alpa_ng/(k_0*ng);
        Yinc_h=-iden*na;
        Yref_h=-iden*na;
        Ytr_h=-iden*ng;
        Zj=[Ytr_e;Ytr_h];
        z=d2+step/2;
        for q=Ns:-1:1
        if q>Nm+Ng  %dielectric material
            delz(q)=(d3-d2)/Nd;
```

```
            epim=epidd*iden;
        elseif q>Nm && q<=Nm+Ng  %grating part
                    delz(q)=(d2-d1)/Ng;
                    dd=1;
                    z=z-step;
                    x1=(L1/pi)*asin((z-d1)/(d2-d1));
                for ee=-2*Nt:2*Nt
                    if ee==0;
                         epigg=((2*x1-L1)*(epidd-epis)+epidd*L)/L;
else epigg=iota*(epidd-epis)*(exp(-2*iota*pi*ee*x1/L)....
        -exp(-2*iota*pi*ee*(L1-x1)/L))/(2*pi*ee);
                    end
                    epig(dd)=epigg;
                    dd=dd+1;
                end
            %%%%%%%% Toeplitz Matrix%%%%%%%%%%
                    ff=1;
                    for gg=(2*Nt)+1:-1:1;
                        row(ff)=epig(gg);
                        ff=ff+1;
                    end
                        hh=1;
                        for jj=(2*Nt)+1:(4*Nt)+1
                            col(hh)=epig(jj);
                            hh=hh+1;
                        end
                     epim=toeplitz(col,row);


        elseif q>0 && q<=Nm  %metallic part
            delz(q)=d1/Nm;
            epim=epis*iden;
        end
        %%%%% P Matrix %%%%%%%%%%
        %%%%%   RCWA %%%%%%%%%%%%
        Pm=[zero k_0*iden-((K*inv(epim)*K))/k_0;(k_0*(epim)) zero];
```

```
        [Vm1,Gm1] = eig(Pm);
        Gm2=diag(Gm1);
        Gm_imag=imag(Gm2);
        Gm_real=real(Gm2);
        [Gm3, sortindex3]=sort(Gm_imag,'descend');
        Gm_real1=Gm_real(sortindex3);
        Gm=Gm_real1+iota*Gm3;
        Djm=diag(Gm);
        Djmup{q}=diag(Gm(1:(2*Nt)+1));
        Djmlow=diag(Gm((2*Nt)+2:(4*Nt)+2));
        Vm=Vm1(:,sortindex3);
        if q==Ns
            Wm=inv(Vm)*Zj;
        else Wm=inv(Vm)*Zj1;
        end
        Wmup{q}=Wm(1:(2*Nt)+1,1:(2*Nt)+1);
        Wmlow=Wm((2*Nt)+2:(4*Nt)+2,1:(2*Nt)+1);
facAm=expm(-iota*delz(q)*Djmlow)*Wmlow*inv(Wmup{q})*expm(iota*delz(q)*Djmup{q});
        Zj1=Vm*[iden;facAm];
        end
Z0up=Zj1(1:(2*Nt)+1,1:(2*Nt)+1);
Z0low=Zj1((2*Nt)+2:(4*Nt)+2,1:(2*Nt)+1);
fac22=[Z0up -Yref_e;Z0low -Yref_h];
TR=inv(fac22)*[Yinc_e;Yinc_h]*A;
T0=TR(1:(2*Nt)+1);
%%%%%%%%%%% calculating T %%%%%%%%%%%%%
            for sw=1:Ns
          if sw==1
              T=inv(Wmup{sw})*expm(iota*delz(sw)*Djmup{sw})*T0;
          else
        T=inv(Wmup{sw})*expm(iota*delz(sw)*Djmup{sw})*T;
          end
            end

tpp=T;
rpp=TR((2*Nt)+2:(4*Nt)+2);
```

```
sumT=0;
sumR=0;
for vv=1:(2*Nt)+1
    Tpp(vv)=(real(alpha_ng(vv))/alpha_na(Nt+1))*(abs(tpp(vv)))^2;
    Rpp(vv)=(real(alpha_na(vv))/alpha_na(Nt+1))*(abs(rpp(vv)))^2;
    sumT=sumT+Tpp(vv);
    sumR=sumR+Rpp(vv);
end
sum=sumR+sumT;
%%%%%%%%%% Absorptance   %%%%%%%%%%
Ap(ag)=1-sum;
%%%%%%%%%% Reflectance   %%%%%%%%%%
Rp(ag)=sumR;
Rp0(ag)=Rpp(Nt+1);
%%%%%%%%%% Transmittance %%%%%%%%%%
Tp(ag)=sumT;
uu=uu+1;
ag=ag+1;
end
plot(0:diff:last,Ap,'LineWidth',2)
xlabel('\theta (deg)')
ylabel('A_{p}')
hold on
end
```

7.2 Code for Fig. 3.3

```
iota = sqrt(-1);
nm = 10^(-9);
epi0=8.85*10^(-12); %permittivity of free space
meu0=4*pi*10^(-7); %permeability of free space
eta0=sqrt(meu0/epi0);
lam_0 = 635*nm; %wavelength
epis =(0.14089+3.6318*iota)^2; %permittivity of gold
k_0=2*pi/lam_0; %wavenumber
L = 700*nm; %period
```

```
L1=0.5*L; %offset of grating
Lg = 40; %thickness of grating
Lm = 1000; %thickness of dielectric material to be sensed
D  = 20;
d1 = D*nm; %thickness of metal (gold)
d2 = d1+Lg*nm;
d3 = d2+Lm*nm;
Nt = 21; %number of terms in the summation
Nd = D;
Ng = Lg;
Nm = Lm;
Ns=Nd+Ng+Nm;
zero=zeros((2*Nt)+1);
iden=eye((2*Nt)+1);
A=zeros(((2*Nt)+1),1); %incidence for p-polarized light
A(Nt+1,1)=1;
step=(d2-d1)/Ng;
na=1.7; %refractive index of prism
nn=1.2;
nd=nn+0.00001*iota;
ng=nn; %refractive index of transmission medium
epidd = nd^2;
tt=11.4;   %%angle of incidence
disp(tt)
theta=tt*pi/180;
zs=1:Ns;
yy=1;
ppa=1;
for xx=0:0.004:2
x=xx*L;
aa=1;
    for n=-Nt:Nt
            kapa(aa)=(k_0*na*sin(theta))+n*(2*pi/L);
            alpha_na(aa)=sqrt(k_0^2*na^2-kapa(aa)^2);
            alpha_ng(aa)=sqrt(k_0^2*ng^2-kapa(aa)^2);
            aa=aa+1;
```

```
end
    K=diag(kapa);
    alpa_na=diag(alpha_na);
    alpa_ng=diag(alpha_ng);
    Yinc_e=-alpa_na/(k_0*na);
    Yref_e=alpa_na/(k_0*na);
    Ytr_e=-alpa_ng/(k_0*ng);
    Yinc_h=-iden*na;
    Yref_h=-iden*na;
    Ytr_h=-iden*ng;
    ZNs=[Ytr_e;Ytr_h];
    z=d2+step/2;
    for q=Ns:-1:1
    if q>Nd+Ng %dielectric material
        delz(q)=(d3-d2)/Nm;
        epim{q}=epidd*iden;
    elseif q>Nd && q<=Nd+Ng %grating part
                delz(q)=(d2-d1)/Ng;
                dd=1;
                z=z-step;
                x1=(L1/pi)*asin((z-d1)/(d2-d1));
            for ee=-2*Nt:2*Nt
                if ee==0;
                     epigg=((2*x1-L1)*(epidd-epis)+epidd*L)/L;
                else epigg=iota*(epidd-epis)*(exp(-2*iota*pi*ee*x1/L).....
                -exp(-2*iota*pi*ee*(L1-x1)/L))/(2*pi*ee);
                end
                epig(dd)=epigg;
                dd=dd+1;
            end
        %%%%%%%% Toeplitz Matrix%%%%%%%%%%
                ff=1;
                for gg=(2*Nt)+1:-1:1;
                    row(ff)=epig(gg);
                    ff=ff+1;
                end
```

```
                    hh=1;
                    for jj=(2*Nt)+1:(4*Nt)+1
                        col(hh)=epig(jj);
                        hh=hh+1;
                    end
                epim{q}=toeplitz(col,row);
        else
            delz(q)=d1/Nd; %metallic part
            epim{q}=epis*iden;
        end
        %%%%% P Matrix %%%%%%%%%%
        %%%%%   RCWA %%%%%%%%%%%%

        Pm=[zero k_0*iden-((K*inv(epim{q})*K))/k_0;(k_0*(epim{q})) zero];
        [Vm1,Gm1] = eig(Pm);
        Gm2=diag(Gm1);
        Gm_imag=imag(Gm2);
        Gm_real=real(Gm2);
        [Gm3, sortindex3]=sort(Gm_imag,'descend');
        Gm_real1=Gm_real(sortindex3);
        Gm=Gm_real1+iota*Gm3;
        Djm=diag(Gm);
        Djmup{q}=diag(Gm(1:(2*Nt)+1));
        Djmlow=diag(Gm((2*Nt)+2:(4*Nt)+2));
        Vm=Vm1(:,sortindex3);
        if q==Ns
            Wm=inv(Vm)*ZNs;
        else Wm=inv(Vm)*Zj1{q+1};
        end
        Wmup{q}=Wm(1:(2*Nt)+1,1:(2*Nt)+1);
        Wmlow=Wm((2*Nt)+2:(4*Nt)+2,1:(2*Nt)+1);
        facAm=expm(-iota*delz(q)*Djmlow)*Wmlow*inv(Wmup{q}).....
        *expm(iota*delz(q)*Djmup{q});
        Zj1{q}=Vm*[iden;facAm];
        end
Z0=Zj1{1};
```

```
Z0up=Z0(1:(2*Nt)+1,1:(2*Nt)+1);
Z0low=Z0((2*Nt)+2:(4*Nt)+2,1:(2*Nt)+1);
fac22=[Z0up -Yref_e;Z0low -Yref_h];
TR=inv(fac22)*[Yinc_e;Yinc_h]*A;
T0=TR(1:(2*Nt)+1);
%%%%%%%%%%% calculating T %%%%%%%%%%%%%
Tj{1}=inv(Wmup{1})*expm(iota*delz(1)*Djmup{1})*T0;
for sw=2:Ns
    Tj{sw}=inv(Wmup{sw})*expm(iota*delz(sw)*Djmup{sw})*Tj{sw-1};
end
%%%%%%%%%%%%%%
kx=diag(K);
T=cell(1,Ns+1);
Z=cell(1,Ns+1);
T{1}=T0;
T(2:Ns+1)=Tj;
Z(1:Ns)=Zj1;
Z{Ns+1}=ZNs;
%%%%%%%% Calcialting f, Ex, Hy %%%%%%%%
for ba=1:Ns+1
   fj{ba}=Z{ba}*T{ba};
   temp=fj{ba};
   Exx{ba}=temp(1:(2*Nt)+1);
   Hyy{ba}=temp((2*Nt)+2:(4*Nt)+2)/eta0;
end

%%%%%%% Calcualting Px %%%%%%%%%%

for ka=1:Ns
    Ex_avg{ka}=(Exx{ka+1}+Exx{ka})/2;
    Hy_avg{ka}=(Hyy{ka+1}+Hyy{ka})/2;
    Ezz{ka}=(-eta0/k_0)*((epim{ka})^(-1))*K*Hy_avg{ka};
    EE=Ezz{ka};
    HH=Hy_avg{ka};

sumE=0;
```

```
sumH=0;
for kd=-Nt:Nt
    sumE=sumE+(EE(kd+Nt+1)*exp(iota*kapa(kd+Nt+1)*x));
    sumH=sumH+(HH(kd+Nt+1)*exp(iota*kapa(kd+Nt+1)*x));
end
Px(ppa)=-0.5*real(sumE*conj(sumH));
XXa(ppa)=x/L;
ppa=ppa+1;
end
end
Zx=1;
for bj=1:501
for bk=1:Ns
    ZZ(Zx)=bk;
Zx=Zx+1;
end
end
file1='0--2_L700_n11.xlsx';
xlswrite(file1,XXa',1,'A1')
xlswrite(file1,ZZ',1,'B1')
xlswrite(file1,Px',1,'C1')
AX1=XXa';
AX2=ZZ';
Ax3=Px';
```

7.3 Code for Fig. 3.4

```
n=[1:0.05:1.5];

for pp=1:length(n)-1
    nd(pp)=(n(pp)+n(pp+1))/2;
end
%%%%%%%%%% n=1 %%%%%%%%%%%%
```

```
%angle of incidence when L=700nm and np=1.7
X71 = [4.7 6.5 8.2 9.9 11.4 13 14.6 16.2 18 19.8 21.6];
%angle of incidence when L=800nm and np=1.7
X81 = [8.4 10.4 12.3 14.2 16.1 18 19.8 21.7 23.5 25.5 27.7];
%angle of incidence when L=700nm and np=2.6
X71_p26 = [3 4.3 5.6 6.8 8.1 9.5 11 12.5 13.9 15.5 17];
%%%%%%%%%% n=0 %%%%%%%%%%%%
%angle of incidence when L=700nm and np=1.7
X70 = [38.4 41 43.9 46.7 52.2 55.4 58.1 61.6 65.7 70.4 76.4];
%angle of incidence when L=800nm and np=1.7
X80 = [38.3 40.8 43.4 46 49.4 52.8 60.1 63.2 67.1 71.8 77.1];
%angle of incidence when L=700nm and np=2.6
X70_p26 = [23.9 25.3 26.6 28.1 29.6 31.2 32.8 34.4 36 37.9 39.8];
for i=1:length(n)-1

%%%%%%% calculating sensitivity%%%%%%%%%%
    sensi1(i)=(X71(i+1)-X71(i))/0.05;
    sensi2(i)=(X70(i+1)-X70(i))/0.05;
    sensi3(i)=(X81(i+1)-X81(i))/0.05;
    sensi4(i)=(X80(i+1)-X80(i))/0.05;
    sensi5(i)=(X71_p26(i+1)-X71_p26(i))/0.05;
    sensi6(i)=(X70_p26(i+1)-X70_p26(i))/0.05;
end
plot(nd,sensi2,'k','LineWidth',3)
xlabel('n_d')
ylabel('Sensitivity (deg/RIU)')
hold on
plot(nd,sensi1,'k--','LineWidth',3)
figure
plot(nd,sensi4,'k','LineWidth',3)
xlabel('n_d')
ylabel('Sensitivity (deg/RIU)')
hold on
plot(nd,sensi3,'k--','LineWidth',3)
figure
plot(nd,sensi6,'k','LineWidth',3)
```

```
xlabel('n_d')
ylabel('Sensitivity (deg/RIU)')
hold on
plot(nd,sensi5,'k--','LineWidth',3)
```

7.4 Code for Fig. 3.5

```
n=[1:0.05:1.5];

for pp=1:length(n)-1
    nd(pp)=(n(pp)+n(pp+1))/2;
end
%%%%%%%%%% n=1 %%%%%%%%%%%%
%angle of incidence when L=700nm and np=1.7
X71 = [4.7 6.5 8.2 9.9 11.4 13 14.6 16.2 18 19.8 21.6];
%angle of incidence when L=800nm and np=1.7
X81 = [8.4 10.4 12.3 14.2 16.1 18 19.8 21.7 23.5 25.5 27.7];
%angle of incidence when L=700nm and np=2.6
X71_p26 = [3 4.3 5.6 6.8 8.1 9.5 11 12.5 13.9 15.5 17];
%%%%%%%%%% n=0 %%%%%%%%%%%%
%angle of incidence when L=700nm and np=1.7
X70 = [38.4 41 43.9 46.7 52.2 55.4 58.1 61.6 65.7 70.4 76.4];
%angle of incidence when L=800nm and np=1.7
X80 = [38.3 40.8 43.4 46 49.4 52.8 60.1 63.2 67.1 71.8 77.1];
%angle of incidence when L=700nm and np=2.6
X70_p26 = [23.9 25.3 26.6 28.1 29.6 31.2 32.8 34.4 36 37.9 39.8];
for i=1:length(n)-1

%%%%%%%% calculating sensitivity%%%%%%%%%%
    sensi1(i)=(X71(i+1)-X71(i))/0.05;
    sensi2(i)=(X70(i+1)-X70(i))/0.05;
    sensi3(i)=(X81(i+1)-X81(i))/0.05;
    sensi4(i)=(X80(i+1)-X80(i))/0.05;
    sensi5(i)=(X71_p26(i+1)-X71_p26(i))/0.05;
```

```
    sensi6(i)=(X70_p26(i+1)-X70_p26(i))/0.05;
end
%%%%%%%%%% n=1 %%%%%%%%%%%%
%coordinates at y-axis when L=700nm and np=1.7
Y71 = [0.1299  0.147  0.1713  0.194  0.2083 .....
 0.2016  0.178  0.1888  0.1759  0.1674  0.1628];
%FWHM when L=700nm and np=1.7
Y71_Full= [0.09245  0.09242  0.09756  0.1102  0.1057 .....
 0.1137  0.1108  0.1193  0.1159  0.1188  0.1225];
%coordinates at y-axis when L=800nm and np=1.7
Y81 = [0.1297  0.1302  0.1366  0.1546  0.1631 .....
 0.1843  0.2063  0.2211  0.2257  0.2132  0.2206];
%FWHM when L=800nm and np=1.7
Y81_Full = [0.09963  0.09751  0.09533  0.09544  0.09648 .....
 0.09751  0.1063  0.1037  0.1139  0.1107  0.1224];
%coordinates at y-axis when L=700nm and np=2.6
Y71_p26 = [0.1164  0.1194  0.1239  0.1239  0.1185 .....
 0.1172  0.1202  0.123  0.1258  0.1304  0.1377];
%FWHM when L=700nm and np=2.6
Y71_p26_Full = [0.09403  0.09516  0.09339  0.09432  0.09238 .....
 0.0941  0.09561 0.09513  0.09869  0.09623  0.09991];
%%%%%%%%%% n=0 %%%%%%%%%%%%
%coordinates at y-axis when L=700nm and np=1.7
Y70 = [0.5109  0.548  0.6115  0.6618  0.7964 .....
 0.7487  0.7564  0.7213  0.6821  0.6382  0.6278];
%FWHM when L=700nm and np=1.7
Y70_Full= [0.08773  0.1387  0.1073  0.1333  0.1141 .....
 0.1596  0.1274  0.2152  0.1598  0.1912  0.2375];
%coordinates at y-axis when L=800nm and np=1.7
Y80 = [0.5492  0.5329  0.5614  0.6285  0.628  .....
0.6712  0.8314  0.817  0.7837  0.7528  0.7478];
%FWHM when L=800nm and np=1.7
Y80_Full= [0.09206  0.08404  0.08943  0.09952  0.0882 .....
 0.0999  0.09658  0.1208  0.1421  0.1311  0.1667];
%coordinates at y-axis when L=700nm and np=2.
Y70_p26 = [0.4299  0.4324  0.4714  0.472  0.4492 .....
```

```
 0.4375  0.454  0.501  0.4962  0.4661  0.473];
%FWHM when L=700nm and np=2.6
Y70_p26_Full= [0.08587  0.09166  0.08673  0.09415  0.08643 .....
 0.09606  0.08728  0.09734  0.09116  0.0983  0.09814];


Y1=(Y71+Y71_Full)./2;
Y2=(Y70+Y70_Full)./2;
Y3=(Y81+Y81_Full)./2;
Y4=(Y80+Y80_Full)./2;
Y5=(Y71_p26+Y71_p26_Full)./2;
Y6=(Y70_p26+Y70_p26_Full)./2;
% %%%%%%% delta theta %%%%%%
d71 = [4  5.7  7.3  9  10.4  11.9  13.4  15.2  16.7  18.4  20.1];
d70 = [37.3  39.7  42.1  44.7  48  51.4  54.4  57.8  61.4  66  71.6];
d81 = [7.7  9.6  11.4  13.3  15.1  16.9  18.6  20.3  22  23.6  25.6];
d80 = [37.3  39.6  42  44.5  47.3  50.4  54  57.5  61.4  65.9  71];
d71_p26 = [2.5  3.8  4.9  6.1  7.3  8.7  10.1  11.4  12.8  14.1  15.5];
d70_p26 = [23.3  24.4  25.9  27.2  28.6  30.1  31.6  33  34.5  36.2  37.9];
FWHM71=(X71-d71).*2;
FWHM70=(X70-d70).*2;
FWHM81=(X81-d81).*2;
FWHM80=(X80-d80).*2;
FWHM71_p26=(X71_p26-d71_p26).*2;
FWHM70_p26=(X70_p26-d70_p26).*2;
for jj=1:length(n)-1
    avg71(jj)=FWHM71(jj)+FWHM71(jj+1)/2;
    avg70(jj)=FWHM70(jj)+FWHM70(jj+1)/2;
    avg81(jj)=FWHM81(jj)+FWHM81(jj+1)/2;
    avg80(jj)=FWHM80(jj)+FWHM80(jj+1)/2;
    avg71_p26(jj)=FWHM71_p26(jj)+FWHM71_p26(jj+1)/2;
    avg70_p26(jj)=FWHM70_p26(jj)+FWHM70_p26(jj+1)/2;
end
for i=1:length(n)-1

%%%%%%%% calculating FOM %%%%%%%%%%
```

```
    FOM1(i)=sensi1(i)/avg71(i);
    FOM2(i)=sensi2(i)/avg70(i);
    FOM3(i)=sensi3(i)/avg81(i);
    FOM4(i)=sensi4(i)/avg80(i);
    FOM5(i)=sensi5(i)/avg71_p26(i);
    FOM6(i)=sensi6(i)/avg70_p26(i);
end
plot(nd,FOM2,'k','LineWidth',4)
xlabel('n_d')
ylabel('FOM')
hold on
plot(nd,FOM1,'k--','LineWidth',4)
figure
plot(nd,FOM4,'k','LineWidth',4)
xlabel('n_d')
ylabel('FOM')
hold on
plot(nd,FOM3,'k--','LineWidth',4)
figure
plot(nd,FOM6,'k','LineWidth',4)
xlabel('n_d')
ylabel('FOM')
hold on
plot(nd,FOM5,'k--','LineWidth',4)
```

7.5 Code for Fig. 3.7

```
file1 = 'Gold_nk_500-1500.xlsx';
% Saving n and k for gold
lam1 = xlsread(file1,'A1:A1001');
nss1 = xlsread(file1,'B1:B1001');
kss1 = xlsread(file1,'C1:C1001');
lam  = lam1';
ns  = nss1';
k1   = kss1';
```

```
iota = sqrt(-1);
nm = 10^(-9);
lam_0 = lam*nm;
L = 800*nm; %period
n_air=1.7; %refractive index of prism
fac=n_air*sin(0*pi/180);
for nd=1:0.1:1.5
epid=nd^2;
for aa=1:1001
epis =(ns(aa)+k1(aa)*iota)^2;  %gold
q_k0(aa)=real(sqrt((epid*epis)/(epid+epis)));
end
plot(lam,(q_k0),'LineWidth',3)
xlabel('\lambda (nm)')
ylabel('Re(q/k_0)')
hold on
end
plot(lam,lam_0/L,'k','LineWidth',3,'HandleVisibility','off')
```

7.6 Code for Fig. 4.2

```
iota = sqrt(-1);
nm = 10^(-9);
lam_0 = 633*nm; %wavelength
epis =(-11.8+1.3*iota); %permittivity of gold
k_0=2*pi/lam_0; %wavenumber
zeta=0.5;
ind=1;
for aad=0.5:0.1:2.0
Lg = 250; %thickness of grating
L= aad*lam_0; %period
Lm=10;    %thickness of metal (gold)
d1 = Lm*nm;
d2=d1+Lg*nm;
```

```
Nt=15;%number of terms in the summation
Nm=1;
Ng=1;
Ns=Ng+Nm;
zero=zeros((2*Nt)+1);
iden=eye((2*Nt)+1);
A=zeros(((2*Nt)+1),1); %incidence for p-polarized light
A(Nt+1,1)=1;
%%%% Materials in Photonic Crystal%%%
n1=1.5;
n2=2;
ep1=(n1)^2+iota*0.00000;
ep2=(n2)^2+iota*0.00000;
%%% plot angle
diff=1;
last=80;
%%%%%%% refractive index of prism and transmission media
na=2.6;
ng=2.6;
%%%%%%%%%%%%%%%%%%%%%%%%%%%%%%%%%%%%%%%%%%%%%%%%%%%%%
ag=1;
uu=1;
for tt=0:diff:last
    Lpc(ind) = L/lam_0;
    ang(ind) = tt;
    disp(tt)
        theta(uu)=tt*pi/180;
         aa=1;
        for n=-Nt:Nt
            kapa(aa)=(k_0*na*sin(theta(uu)))+n*(2*pi/L);
            alpha_na(aa)=sqrt(k_0^2*na^2-kapa(aa)^2);
            alpha_ng(aa)=sqrt(k_0^2*ng^2-kapa(aa)^2);
            aa=aa+1;
        end
        K=diag(kapa);
        alpa_na=diag(alpha_na);
```

```
alpa_ng=diag(alpha_ng);
Yinc_e=-alpa_na/(k_0*na);
Yref_e=alpa_na/(k_0*na);
Ytr_e=-alpa_ng/(k_0*ng);
Yinc_h=-iden*na;
Yref_h=-iden*na;
Ytr_h=-iden*ng;
Zj=[Ytr_e;Ytr_h];
for q=Ns:-1:1
     if q>Nm  %photoni crystal part
            delz(q)=(d2-d1)/Ng;
            dd=1;
        for ee=-2*Nt:2*Nt
            if ee==0;
                 epigg=(ep1-ep2)*zeta+ep2;
            else epigg=iota*(ep2-ep1)*(1-.....
            exp(-2*iota*pi*ee*zeta))/(2*pi*ee);
            end
            epig(dd)=epigg;
            dd=dd+1;
        end
    %%%%%%% Toeplitz Matrix%%%%%%%%%
            ff=1;
            for gg=(2*Nt)+1:-1:1;
                row(ff)=epig(gg);
                ff=ff+1;
            end
                hh=1;
                for jj=(2*Nt)+1:(4*Nt)+1
                    col(hh)=epig(jj);
                    hh=hh+1;
                end
             epim=toeplitz(col,row);
elseif q>0 && q<=Nm %metallic part
    delz(q)=d1/Nm;
    epim=epis*iden;
```

```
        end
        %%%%% P Matrix %%%%%%%%%%
        %%%%%   RCWA %%%%%%%%%%%%
        Pm=[zero k_0*iden-((K*inv(epim)*K))/k_0;(k_0*(epim)) zero];
        [Vm1,Gm1] = eig(Pm);
        Gm2=diag(Gm1);
        Gm_imag=imag(Gm2);
        Gm_real=real(Gm2);
        [Gm3, sortindex3]=sort(Gm_imag,'descend');
        Gm_real1=Gm_real(sortindex3);
        Gm=Gm_real1+iota*Gm3;
        Djm=diag(Gm);
        Djmup{q}=diag(Gm(1:(2*Nt)+1));
        Djmlow=diag(Gm((2*Nt)+2:(4*Nt)+2));
        Vm=Vm1(:,sortindex3);
        if q==Ns
            Wm=inv(Vm)*Zj;
        else Wm=inv(Vm)*Zj1;
        end
        Wmup{q}=Wm(1:(2*Nt)+1,1:(2*Nt)+1);
        Wmlow=Wm((2*Nt)+2:(4*Nt)+2,1:(2*Nt)+1);
        facAm=expm(-iota*delz(q)*Djmlow)*Wmlow*inv(Wmup{q}).....
        *expm(iota*delz(q)*Djmup{q});
        Zj1=Vm*[iden;facAm];
        end
Z0up=Zj1(1:(2*Nt)+1,1:(2*Nt)+1);
Z0low=Zj1((2*Nt)+2:(4*Nt)+2,1:(2*Nt)+1);
fac22=[Z0up -Yref_e;Z0low -Yref_h];
TR=inv(fac22)*[Yinc_e;Yinc_h]*A;
T0=TR(1:(2*Nt)+1);
%%%%%%%%%%% calculating T %%%%%%%%%%%%%
            for sw=1:Ns
          if sw==1
              T=inv(Wmup{sw})*expm(iota*delz(sw)*Djmup{sw})*T0;
          else
        T=inv(Wmup{sw})*expm(iota*delz(sw)*Djmup{sw})*T;
```

```
          end
            end

tpp=T;
rpp=TR((2*Nt)+2:(4*Nt)+2);
sumT=0;
sumR=0;
for vv=1:(2*Nt)+1
    Tpp(vv)=(real(alpha_ng(vv))/alpha_na(Nt+1))*(abs(tpp(vv)))^2;
    Rpp(vv)=(real(alpha_na(vv))/alpha_na(Nt+1))*(abs(rpp(vv)))^2;
    sumT=sumT+Tpp(vv);
    sumR=sumR+Rpp(vv);
end
sum=sumR+sumT;
%%%%%%%%%% Absorptance   %%%%%%%%%%
Ap(ind)=1-sum;
%%%%%%%%%% Reflectance   %%%%%%%%%%
Rp(ag)=sumR;
Rp0(ag)=Rpp(Nt+1);
%%%%%%%%%% Transmittance %%%%%%%%%%
Tp(ag)=sumT;
uu=uu+1;
ag=ag+1;
ind=ind+1;
end
end
file1='test4.xlsx';
xlswrite(file1,ang',1,'A1')
xlswrite(file1,Lpc',1,'B1')
xlswrite(file1,Ap',1,'C1')
```

7.7 Code for Fig. 5.2

```
clear all
file1 = 'nk_cSi.xlsx';
file2 = 'nk_gold.xlsx';
```

```
file3 = 'AM1.5.xlsx';
file4 = 'MgF2.xlsx';
%%%  Storing n and k values of crystalline silicon  %%%
lam2 = xlsread(file1,'A1:A401');
nss1 = xlsread(file1,'B1:B401');
kss1 = xlsread(file1,'C1:C401');
lam1  = lam2';   %storing wavelength
ns1  = nss1';
k1   = kss1';
%%%  Storing n and k values of gold  %%%
nss2 = xlsread(file2,'B1:B401');
kss2 = xlsread(file2,'C1:C401');
ns2  = nss2';
k2   = kss2';
%%%  Storing AM1.5  %%%
nss3 = xlsread(file3,'B1:B401');
ns3  = nss3';
%%%  Storing n and k values of MgF2%%%
nss4 = xlsread(file4,'B1:B401');
kss4 = xlsread(file4,'C1:C401');
ns4  = nss4';
k4   = kss4';
%%%%%%%%%%%%%%%%%%%%%%%%%%%%%%%%%%%%%%%
iota    = sqrt(-1);
nm      = 10^(-9);
lam     = lam1*nm;
meuAR   = 1; %permeability of anti-reflection coating
meus  = 1;  %permeability of silicon
meugold  = 1;   %permeability of gold
epi0=8.85*10^(-12);
meu0=4*pi*10^(-7);
c=1/sqrt(epi0*meu0);
eta0=sqrt(meu0/epi0);
L = 600*nm;  %period
zeta=0.5;
L_AR  = 80; %thickness of anti-reflection coating
```

```
Lz    = 80;  %thickness of ZIM
Lg    = 80;   %thickness of grating
Ls    = 2000; %thickness of silicon
Lgold = 80;  %thickness of gold
d1    = L_AR*nm;
d2    = d1+Lz*nm;
d3    = d2+Lg*nm;
d4    = d3+Ls*nm;
d5    = d4+Lgold*nm;
Nt    = 15; %number of terms in the summation
NAR   = 1;
Nz    = 1;
Ng    = 1;
Nm    = 1;
Ngold = 1;
Ns=NAR+Nz+Ng+Nm+Ngold;
zero=zeros((2*Nt)+1);
iden=eye((2*Nt)+1);
A=zeros(((2*Nt)+1),1); %incidence for p-polarized light
A(Nt+1,1)=1;
%%% plot angle
diff=1;
last=90;
%%%%%%%%%%
na=1;  %refractive index of incidence medium
ng=1;  %refractive index of transmission medium
nz=0.001;  %refractive index of ZIM
ag=1;
uu=1;
dellam = 1*nm;
sumAM  = 0;
for xb=1:401
    AM(xb)  = ns3(xb);
    sumAM=sumAM+AM(xb)*dellam;
end
for tt=1:401
```

```
%     disp(tt)
    k_0=2*pi/lam(tt); %wavenumber
    epAR    = (ns4(tt)+iota*k4(tt))^2;  %permittivity of anti-reflection coating
    epis    = (ns1(tt)+iota*k1(tt))^2;  %permittivity of silicon
    epigold = (ns2(tt)+iota*k2(tt))^2;  %permittivity of gold
    epidd = 0.01; %permittivity of ZIM
    meudd = 0.01; %permeability of ZIM
    ang=0;
        theta=ang*pi/180;
         aa=1;
        for n=-Nt:Nt
            kapa(aa)=(k_0*na*sin(theta))+n*(2*pi/L);
            alpha_na(aa)=sqrt(k_0^2*na^2-kapa(aa)^2);
            alpha_ng(aa)=sqrt(k_0^2*ng^2-kapa(aa)^2);
            aa=aa+1;
        end
        K=diag(kapa);
        alpa_na=diag(alpha_na);
        alpa_ng=diag(alpha_ng);
        Yinc_e=-alpa_na/(k_0*na);
        Yref_e=alpa_na/(k_0*na);
        Ytr_e=-alpa_ng/(k_0*ng);
        Yinc_h=-iden*na;
        Yref_h=-iden*na;
        Ytr_h=-iden*ng;
        Zj=[Ytr_e;Ytr_h];
        for q=Ns:-1:1
        if q>NAR+Nz+Ng+Nm   %metallic part
            delz(q)=(d5-d4)/Ngold;
            epim=epigold*iden;
            meum = meugold*iden;
        elseif q>NAR+Nz+Ng && q<=NAR+Nz+Ng+Nm  %silicon part
            delz(q)=(d4-d3)/Nm;
            epim = epis*iden;
            meum = meus*iden;
        elseif q>NAR+Nz && q<=NAR+Nz+Ng %grating part
```

```
            delz(q)=(d3-d2)/Ng;
            dd=1;
        for ee=-2*Nt:2*Nt
            if ee==0;
                 epigg=(epis-epidd)*zeta+epidd;
                 meugg=(meus-meudd)*zeta+meudd;
            else epigg=iota*(epidd-epis)*.....
            (1-exp(-2*iota*pi*ee*zeta))/(2*pi*ee);
                 meugg=iota*(meudd-meus)*.....
                 (1-exp(-2*iota*pi*ee*zeta))/(2*pi*ee);
            end
            epig(dd)=epigg;
            meug(dd) = meugg;
            dd=dd+1;
        end
    %%%%%%%% Toeplitz Matrix%%%%%%%%%%
            ff=1;
            for gg=(2*Nt)+1:-1:1;
                row(ff)=epig(gg);
                rowmeu(ff)=meug(gg);
                ff=ff+1;
            end
                hh=1;
                for jj=(2*Nt)+1:(4*Nt)+1
                    col(hh)=epig(jj);
                    colmeu(hh)=meug(jj);
                    hh=hh+1;
                end
             epim = toeplitz(col,row);
             meum = toeplitz(colmeu,rowmeu);
elseif q>NAR && q<=NAR+Nz  %ZIM part
    delz(q)=(d2-d1)/Nz;
    epim = epidd*iden;
    meum = meudd*iden;
elseif q>0 && q<=NAR   %MgF2 part
    delz(q)=d1/NAR;
```

```
            epim = epAR*iden;
            meum = meuAR*iden;
        end
        %%%%% P Matrix %%%%%%%%%%
        %%%%%   RCWA %%%%%%%%%%%%
        Pm=[zero k_0*meum-((K*inv(epim)*K))/k_0;(k_0*(epim)) zero];
        [Vm1,Gm1] = eig(Pm);
        Gm2=diag(Gm1);
        Gm_imag=imag(Gm2);
        Gm_real=real(Gm2);
        [Gm3, sortindex3]=sort(Gm_imag,'descend');
        Gm_real1=Gm_real(sortindex3);
        Gm=Gm_real1+iota*Gm3;
        Djm=diag(Gm);
        Djmup{q}=diag(Gm(1:(2*Nt)+1));
        Djmlow=diag(Gm((2*Nt)+2:(4*Nt)+2));
        Vm=Vm1(:,sortindex3);
        if q==Ns
            Wm=inv(Vm)*Zj;
        else Wm=inv(Vm)*Zj1;
        end
        Wmup{q}=Wm(1:(2*Nt)+1,1:(2*Nt)+1);
        Wmlow=Wm((2*Nt)+2:(4*Nt)+2,1:(2*Nt)+1);
        facAm=expm(-iota*delz(q)*Djmlow)*Wmlow*inv(Wmup{q}).....
        *expm(iota*delz(q)*Djmup{q});
        Zj1=Vm*[iden;facAm];
        end
Z0up=Zj1(1:(2*Nt)+1,1:(2*Nt)+1);
Z0low=Zj1((2*Nt)+2:(4*Nt)+2,1:(2*Nt)+1);
fac22=[Z0up -Yref_e;Z0low -Yref_h];
TR=inv(fac22)*[Yinc_e;Yinc_h]*A;
T0=TR(1:(2*Nt)+1);
%%%%%%%%%%% calculating T %%%%%%%%%%%%%
            for sw=1:Ns
          if sw==1
              T=inv(Wmup{sw})*expm(iota*delz(sw)*Djmup{sw})*T0;
```

```
          else
        T=inv(Wmup{sw})*expm(iota*delz(sw)*Djmup{sw})*T;
          end
            end

tpp=T;
rpp=TR((2*Nt)+2:(4*Nt)+2);
sumT=0;
sumR=0;
for vv=1:(2*Nt)+1
    Tpp(vv)=(real(alpha_ng(vv))/alpha_na(Nt+1))*(abs(tpp(vv)))^2;
    Rpp(vv)=(real(alpha_na(vv))/alpha_na(Nt+1))*(abs(rpp(vv)))^2;
    sumT=sumT+Tpp(vv);
    sumR=sumR+Rpp(vv);
end
sum=sumR+sumT;
%%%%%%%%%% Absorptance   %%%%%%%%%%
Ap(ag)=1-sum;
%%%%%%%%%% Reflectance   %%%%%%%%%%
Rp(ag)=sumR;
Rp0(ag)=Rpp(Nt+1);
%%%%%%%%%% Transmittance %%%%%%%%%%
Tp(ag)=sumT;
%%%% Calculating SSI  %%%%%
ss(ag)=Ap(ag)*AM(tt)*dellam;
uu=uu+1;
ag=ag+1;
end
sum_ss=0;
for xa=1:401
    sum_ss=sum_ss+ss(xa);
end
SSI=sum_ss/sumAM
figure
plot(lam1,Ap,'LineWidth',2)
```

7.8 Code for Fig. 5.3

```
clear all
file1 = 'nk_cSi.xlsx';
file2 = 'nk_gold.xlsx';
file3 = 'AM1.5.xlsx';
file4 = 'MgF2.xlsx';
%%%  Storing n and k values of crystalline silicon  %%%
lam2 = xlsread(file1,'A1:A401');
nss1 = xlsread(file1,'B1:B401');
kss1 = xlsread(file1,'C1:C401');
lam1  = lam2'; %storing wavelength
ns1  = nss1';
k1   = kss1';
%%%  Storing n and k values of gold  %%%
nss2 = xlsread(file2,'B1:B401');
kss2 = xlsread(file2,'C1:C401');
ns2  = nss2';
k2   = kss2';
%%%  Storing AM1.5  %%%
nss3 = xlsread(file3,'B1:B401');
ns3  = nss3';
%%%  Storing n and k values of MgF2%%%
nss4 = xlsread(file4,'B1:B401');
kss4 = xlsread(file4,'C1:C401');
ns4  = nss4';
k4   = kss4';
%%%%%%%%%%%%%%%%%%%%%%%%%%%%%%%%%%%%
iota    = sqrt(-1);
nm      = 10^(-9);
lam     = lam1*nm;
meuAR   = 1;  %permeability of anti-reflection coating
meus  = 1; %permeability of silicon
meugold  = 1; %permeability of gold
epi0=8.85*10^(-12);
meu0=4*pi*10^(-7);
c=1/sqrt(epi0*meu0);
```

```
eta0=sqrt(meu0/epi0);
L = 600*nm;
zeta=0.5;
L_AR  = 80; %thickness of anti-reflection coating
Lz    = 80; %thickness of ZIM
Lg    = 80; %thickness of grating
Ls    = 2000; %thickness of silicon
Lgold = 80;  %thickness of gold
d1    = L_AR*nm;
d2    = d1+Lz*nm;
d3    = d2+Lg*nm;
d4    = d3+Ls*nm;
d5    = d4+Lgold*nm;
Nt    = 15; %number of terms in the summation
NAR   = 1;
Nz    = 1;
Ng    = 1;
Nm    = 1;
Ngold = 1;
Ns=NAR+Nz+Ng+Nm+Ngold;
zero=zeros((2*Nt)+1);
iden=eye((2*Nt)+1);
A=zeros(((2*Nt)+1),1); %incidence for s-polarized light
A(Nt+1,1)=1;
%%%%%%%%%%
na=1;  %refractive index of incidence medium
ng=1;  %refractive index of transmission medium
nz=0.001;  %refractive index of ZIM
ag=1;
uu=1;
dellam = 1*nm;
sumAM  = 0;
for xb=1:401
    AM(xb)  = ns3(xb);
    sumAM=sumAM+AM(xb)*dellam;
end
```

```
for tt=1:401
    disp(tt)
    k_0=2*pi/lam(tt);  %wavenumber
    epAR    = (ns4(tt)+iota*k4(tt))^2;  %permittivity of anti-reflection coating
    epis    = (ns1(tt)+iota*k1(tt))^2;  %permittivity of silicon
    epigold = (ns2(tt)+iota*k2(tt))^2;  %permittivity of gold
    epidd = 0.01; %permittivity of ZIM
    meudd = 0.01; %permeability of ZIM
    ang=0;
        theta=ang*pi/180;
         aa=1;
        for n=-Nt:Nt
            kapa(aa)=(k_0*na*sin(theta))+n*(2*pi/L);
            alpha_na(aa)=sqrt(k_0^2*na^2-kapa(aa)^2);
            alpha_ng(aa)=sqrt(k_0^2*ng^2-kapa(aa)^2);
            aa=aa+1;
        end
        K=diag(kapa);
        alpa_na=diag(alpha_na);
        alpa_ng=diag(alpha_ng);
        Yinc_e=iden*na;
        Yref_e=iden*na;
        Ytr_e=iden*ng;
        Yinc_h=-alpa_na/(k_0*na);
        Yref_h=alpa_na/(k_0*na);
        Ytr_h=-alpa_ng/(k_0*ng);
        Zj=[Ytr_e;Ytr_h];
        for q=Ns:-1:1
        if q>NAR+Nz+Ng+Nm %metallic part
            delz(q)=(d5-d4)/Ngold;
            epim=epigold*iden;
            meum = meugold*iden;
        elseif q>NAR+Nz+Ng && q<=NAR+Nz+Ng+Nm %silicon part
            delz(q)=(d4-d3)/Nm;
            epim = epis*iden;
            meum = meus*iden;
```

```
elseif q>NAR+Nz && q<=NAR+Nz+Ng %grating part
            delz(q)=(d2-d1)/Ng;
            dd=1;
        for ee=-2*Nt:2*Nt
            if ee==0;
                 epigg=(epis-epidd)*zeta+epidd;
                 meugg=(meus-meudd)*zeta+meudd;
            else epigg=iota*(epidd-epis)*.....
            (1-exp(-2*iota*pi*ee*zeta))/(2*pi*ee);
                 meugg=iota*(meudd-meus)*.....
                 (1-exp(-2*iota*pi*ee*zeta))/(2*pi*ee);
            end
            epig(dd)=epigg;
            meug(dd) = meugg;
            dd=dd+1;
        end
    %%%%%%%% Toeplitz Matrix%%%%%%%%%%
            ff=1;
            for gg=(2*Nt)+1:-1:1;
                row(ff)=epig(gg);
                rowmeu(ff)=meug(gg);
                ff=ff+1;
            end
                hh=1;
                for jj=(2*Nt)+1:(4*Nt)+1
                    col(hh)=epig(jj);
                    colmeu(hh)=meug(jj);
                    hh=hh+1;
                end
             epim = toeplitz(col,row);
             meum = toeplitz(colmeu,rowmeu);
elseif q>NAR && q<=NAR+Nz %ZIM part
    delz(q)=(d2-d1)/Nz;
    epim = epidd*iden;
    meum = meudd*iden;
elseif q>0 && q<=NAR %MgF2 part
```

```
            delz(q)=d1/NAR;
            epim = epAR*iden;
            meum = meuAR*iden;
        end
        %%%% P Matrix %%%%%%%%%%
        %%%%   RCWA %%%%%%%%%%%%
        Pm=[zero -k_0*meum;((K*inv(meum)*K)/k_0)-k_0*(epim) zero];
        [Vm1,Gm1] = eig(Pm);
        Gm2=diag(Gm1);
        Gm_imag=imag(Gm2);
        Gm_real=real(Gm2);
        [Gm3, sortindex3]=sort(Gm_imag,'descend');
        Gm_real1=Gm_real(sortindex3);
        Gm=Gm_real1+iota*Gm3;
        Djm=diag(Gm);
        Djmup{q}=diag(Gm(1:(2*Nt)+1));
        Djmlow=diag(Gm((2*Nt)+2:(4*Nt)+2));
        Vm=Vm1(:,sortindex3);
        if q==Ns
            Wm=inv(Vm)*Zj;
        else Wm=inv(Vm)*Zj1;
        end
        Wmup{q}=Wm(1:(2*Nt)+1,1:(2*Nt)+1);
        Wmlow=Wm((2*Nt)+2:(4*Nt)+2,1:(2*Nt)+1);
        facAm=expm(-iota*delz(q)*Djmlow)*Wmlow*inv(Wmup{q}).....
        *expm(iota*delz(q)*Djmup{q});
        Zj1=Vm*[iden;facAm];
        end
Z0up=Zj1(1:(2*Nt)+1,1:(2*Nt)+1);
Z0low=Zj1((2*Nt)+2:(4*Nt)+2,1:(2*Nt)+1);
fac22=[Z0up -Yref_e;Z0low -Yref_h];
TR=inv(fac22)*[Yinc_e;Yinc_h]*A;
T0=TR(1:(2*Nt)+1);
%%%%%%%%%%% calculating T %%%%%%%%%%%%%
            for sw=1:Ns
          if sw==1
```

```
              T=inv(Wmup{sw})*expm(iota*delz(sw)*Djmup{sw})*T0;
          else
        T=inv(Wmup{sw})*expm(iota*delz(sw)*Djmup{sw})*T;
          end
            end
tpp=T;
rpp=TR((2*Nt)+2:(4*Nt)+2);
sumT=0;
sumR=0;
for vv=1:(2*Nt)+1
    Tpp(vv)=(real(alpha_ng(vv))/alpha_na(Nt+1))*(abs(tpp(vv)))^2;
    Rpp(vv)=(real(alpha_na(vv))/alpha_na(Nt+1))*(abs(rpp(vv)))^2;
    sumT=sumT+Tpp(vv);
    sumR=sumR+Rpp(vv);
end
sum=sumR+sumT;
%%%%%%%%%% Absorptance   %%%%%%%%%%
Ap(ag)=1-sum;
%%%%%%%%%% Reflectance   %%%%%%%%%%
Rp(ag)=sumR;
Rp0(ag)=Rpp(Nt+1);
%%%%%%%%%% Transmittance %%%%%%%%%%
Tp(ag)=sumT;
%%%% Calculating SSI  %%%%%
ss(ag)=Ap(ag)*AM(tt)*dellam;
uu=uu+1;
ag=ag+1;
end
sum_ss=0;
for xa=1:401
    sum_ss=sum_ss+ss(xa);
end
SSI=sum_ss/sumAM
plot(lam1,Ap,'LineWidth',2)
```

7.9 Code for Fig. 5.4

```
clear all
file1 = 'nk_cSi.xlsx';
file2 = 'nk_gold.xlsx';
file3 = 'AM1.5.xlsx';
file4 = 'MgF2.xlsx';
%%%  Storing n and k values of crystalline silicon  %%%
lam2 = xlsread(file1,'A1:A401');
nss1 = xlsread(file1,'B1:B401');
kss1 = xlsread(file1,'C1:C401');
lam1  = lam2';   %storing wavelength
ns1  = nss1';
k1   = kss1';
%%%  Storing n and k values of gold  %%%
nss2 = xlsread(file2,'B1:B401');
kss2 = xlsread(file2,'C1:C401');
ns2  = nss2';
k2   = kss2';
%%%  Storing AM1.5  %%%
nss3 = xlsread(file3,'B1:B401');
ns3  = nss3';
%%%  Storing n and k values of MgF2%%%
nss4 = xlsread(file4,'B1:B401');
kss4 = xlsread(file4,'C1:C401');
ns4  = nss4';
k4   = kss4';
%%%%%%%%%%%%%%%%%%%%%%%%%%%%%%%%%%%%
iota    = sqrt(-1);
nm      = 10^(-9);
lam     = lam1*nm;
meuAR   = 1; %permeability of anti-reflection coating
meus  = 1;  %permeability of silicon
meugold  = 1;   %permeability of gold
epi0=8.85*10^(-12);
meu0=4*pi*10^(-7);
c=1/sqrt(epi0*meu0);
```

```
eta0=sqrt(meu0/epi0);
zeta=0.5;
L_AR  = 80; %thickness of anti-reflection coating
Lz    = 80;  %thickness of ZIM
Lg    = 80;   %thickness of grating
Ls    = 2000; %thickness of silicon
Lgold = 80;  %thickness of gold
d1    = L_AR*nm;
d2    = d1+Lz*nm;
d3    = d2+Lg*nm;
d4    = d3+Ls*nm;
d5    = d4+Lgold*nm;
Nt    = 15; %number of terms in the summation
NAR   = 1;
Nz    = 1;
Ng    = 1;
Nm    = 1;
Ngold = 1;
Ns=NAR+Nz+Ng+Nm+Ngold;
zero=zeros((2*Nt)+1);
iden=eye((2*Nt)+1);
A=zeros(((2*Nt)+1),1); %incidence for p-polarized light
A(Nt+1,1)=1;
va=100:50:900;
% va=[900];
for vc=1:length(va)
    disp(va(vc));
    L = va(vc)*nm;
%%%%%%%%%%%
na=1;  %refractive index of incidence medium
ng=1;  %refractive index of transmission medium
nz=0.001;  %refractive index of ZIM
ag=1;
uu=1;
dellam = 1*nm;
sumAM  = 0;
```

```
for xb=1:401
    AM(xb)  = ns3(xb);
    sumAM=sumAM+AM(xb)*dellam;
end

for tt=1:401
%     disp(tt)
    k_0=2*pi/lam(tt);
epAR    = (ns4(tt)+iota*k4(tt))^2;  %permittivity of anti-reflection coating
    epis    = (ns1(tt)+iota*k1(tt))^2;  %permittivity of silicon
    epigold = (ns2(tt)+iota*k2(tt))^2;  %permittivity of gold
    epidd = 0.01+iota*0.0;  %permittivity of ZIM
    meudd = 0.01+iota*0;     %permeability of ZIM
    ang=0;
        theta=ang*pi/180;
         aa=1;
        for n=-Nt:Nt
            kapa(aa)=(k_0*na*sin(theta))+n*(2*pi/L);
            alpha_na(aa)=sqrt(k_0^2*na^2-kapa(aa)^2);
            alpha_ng(aa)=sqrt(k_0^2*ng^2-kapa(aa)^2);
            aa=aa+1;
        end
        K=diag(kapa);
        alpa_na=diag(alpha_na);
        alpa_ng=diag(alpha_ng);
        Yinc_e=-alpa_na/(k_0*na);
        Yref_e=alpa_na/(k_0*na);
        Ytr_e=-alpa_ng/(k_0*ng);
        Yinc_h=-iden*na;
        Yref_h=-iden*na;
        Ytr_h=-iden*ng;
        Zj=[Ytr_e;Ytr_h];
        for q=Ns:-1:1
        if q>NAR+Nz+Ng+Nm %metallic part
            delz(q)=(d5-d4)/Ngold;
            epim=epigold*iden;
```

```
    meum = meugold*iden;
elseif q>NAR+Nz+Ng && q<=NAR+Nz+Ng+Nm %silicon part
    delz(q)=(d4-d3)/Nm;
    epim = epis*iden;
    meum = meus*iden;
elseif q>NAR+Nz && q<=NAR+Nz+Ng %grating part
            delz(q)=(d2-d1)/Ng;
            dd=1;
        for ee=-2*Nt:2*Nt
            if ee==0;
                 epigg=(epis-epidd)*zeta+epidd;
                 meugg=(meus-meudd)*zeta+meudd;
            else epigg=iota*(epidd-epis)*.....
            (1-exp(-2*iota*pi*ee*zeta))/(2*pi*ee);
                 meugg=iota*(meudd-meus).....
                 *(1-exp(-2*iota*pi*ee*zeta))/(2*pi*ee);
            end
            epig(dd)=epigg;
            meug(dd) = meugg;
            dd=dd+1;
        end
    %%%%%%% Toeplitz Matrix%%%%%%%%%
            ff=1;
            for gg=(2*Nt)+1:-1:1;
                row(ff)=epig(gg);
                rowmeu(ff)=meug(gg);
                ff=ff+1;
            end
                hh=1;
                for jj=(2*Nt)+1:(4*Nt)+1
                    col(hh)=epig(jj);
                    colmeu(hh)=meug(jj);
                    hh=hh+1;
                end
             epim = toeplitz(col,row);
             meum = toeplitz(colmeu,rowmeu);
```

```
        elseif q>NAR && q<=NAR+Nz %ZIM part
            delz(q)=(d2-d1)/Nz;
            epim = epidd*iden;
            meum = meudd*iden;
        elseif q>0 && q<=NAR %MgF2 part
            delz(q)=d1/NAR;
            epim = epAR*iden;
            meum = meuAR*iden;
        end
        %%%%% P Matrix %%%%%%%%%%
        %%%%%   RCWA %%%%%%%%%%%%
        Pm=[zero k_0*meum-((K*inv(epim)*K))/k_0;(k_0*(epim)) zero];
        [Vm1,Gm1] = eig(Pm);
        Gm2=diag(Gm1);
        Gm_imag=imag(Gm2);
        Gm_real=real(Gm2);
        [Gm3, sortindex3]=sort(Gm_imag,'descend');
        Gm_real1=Gm_real(sortindex3);
        Gm=Gm_real1+iota*Gm3;
        Djm=diag(Gm);
        Djmup{q}=diag(Gm(1:(2*Nt)+1));
        Djmlow=diag(Gm((2*Nt)+2:(4*Nt)+2));
        Vm=Vm1(:,sortindex3);
        if q==Ns
            Wm=inv(Vm)*Zj;
        else Wm=inv(Vm)*Zj1;
        end
        Wmup{q}=Wm(1:(2*Nt)+1,1:(2*Nt)+1);
        Wmlow=Wm((2*Nt)+2:(4*Nt)+2,1:(2*Nt)+1);
        facAm=expm(-iota*delz(q)*Djmlow)*Wmlow*inv(Wmup{q}).....
        *expm(iota*delz(q)*Djmup{q});
        Zj1=Vm*[iden;facAm];
        end
Z0up=Zj1(1:(2*Nt)+1,1:(2*Nt)+1);
Z0low=Zj1((2*Nt)+2:(4*Nt)+2,1:(2*Nt)+1);
fac22=[Z0up -Yref_e;Z0low -Yref_h];
```

```
TR=inv(fac22)*[Yinc_e;Yinc_h]*A;
T0=TR(1:(2*Nt)+1);
%%%%%%%%%%% calculating T %%%%%%%%%%%%%
            for sw=1:Ns
          if sw==1
              T=inv(Wmup{sw})*expm(iota*delz(sw)*Djmup{sw})*T0;
          else
        T=inv(Wmup{sw})*expm(iota*delz(sw)*Djmup{sw})*T;
          end
            end

tpp=T;
rpp=TR((2*Nt)+2:(4*Nt)+2);
sumT=0;
sumR=0;
for vv=1:(2*Nt)+1
    Tpp(vv)=(real(alpha_ng(vv))/alpha_na(Nt+1))*(abs(tpp(vv)))^2;
    Rpp(vv)=(real(alpha_na(vv))/alpha_na(Nt+1))*(abs(rpp(vv)))^2;
    sumT=sumT+Tpp(vv);
    sumR=sumR+Rpp(vv);
end
sum=sumR+sumT;
%%%%%%%%%% Absorptance   %%%%%%%%%%
Ap(ag)=1-sum;
%%%%%%%%%% Reflectance   %%%%%%%%%%
Rp(ag)=sumR;
Rp0(ag)=Rpp(Nt+1);
%%%%%%%%%% Transmittance %%%%%%%%%%
Tp(ag)=sumT;
%%%% Calculating SSI  %%%%%
ss(ag)=Ap(ag)*AM(tt)*dellam;
uu=uu+1;
ag=ag+1;
end
sum_ss=0;
for xa=1:401
```

```
    sum_ss=sum_ss+ss(xa);
end
SSI(vc)=sum_ss/sumAM;
end
plot(va,SSI)
```